Measurement of nuclear decay data for beta decay and electron capture using metallic magnetic calorimeters

Arshjot Kaur

université PARIS-SACLAY

Measurement of nuclear decay data for beta decay and electron capture using metallic magnetic calorimeters

Mesure des données de désintégration de radionucléides relatives aux transitions bêta et aux captures électroniques à l'aide de calorimètres métalliques magnétiques

Thèse de doctorat de l'université Paris-Saclay

École doctorale n°576 Particules, hadrons, énergie et noyau : instrumentation, imagerie, cosmos et simulation (PHENIICS)
Spécialité de doctorat : Physique nucléaire
Graduate School : Physique. Référent : Faculté des sciences d'Orsay

Thèse préparée au **Laboratoire National Henri Becquerel** (Université Paris-Saclay, CEA), sous la direction de **Martin LOIDL**, Directeur de recherche, et le co-encadrement de **Matias RODRIGUES**, Ingénieur de recherche

Thèse soutenue à Paris-Saclay, le 10 Novembre 2023, par

Arshjot KAUR

Composition du Jury

Membres du jury avec voix délibérative

Jean-Luc SAUVAGEOT Directeur de recherche, CEA Saclay- DRF/IRFU/DAP/LSIS, Université Paris-Saclay	Président
Loredana GASTALDO Professeur, Kirchhoff Institute for Physics, Heidelberg University	Rapportrice & Examinatrice
Philippe DESSAGNE Directeur de recherche, Institut luridisciplinaire Hubert Curien (IPHC), CNRS Strasbourg, Université de Strasbourg	Rapporteur & Examinateur
Frédéric JUGET Chercheur, Institute de Radio-physique, Centre Hospitalier Universitaire Vaudois, Université de Lausanne	Examinateur

THÈSE DE DOCTORAT

NNT:2023UPASP151

université PARIS-SACLAY

ÉCOLE DOCTORALE
Particules, hadrons, énergie et noyau : instrumentation, imagerie, cosmos et simulation (PHENIICS)

Titre: Mesure des données de désintégration de radionucléides relatives aux transitions bêta et aux captures électroniques à l'aide de calorimètres métalliques magnétiques

Mots clés: Détecteurs cryogéniques, métrologie des radionucléides, données de décroissance radioactive, Spectroscopie d'énergie de désintégration, probabilités fractionnelles de captures électroniques, spectres bêta

Résumé: La précision des probabilités fractionnelles de captures électroniques (CE) et des mesures des spectres bêta est vitale pour la métrologie des radionucléides. Lors de la détermination de l'unité SI d'activité, le becquerel, à l'aide de mesures primaires d'activité comme le comptage par scintillation liquide (LSC), les données de désintégration relatives à la désintégration bêta et à la CE sont essentielles. Ces données sont également cruciales pour valider les calculs théoriques et pour de nombreuses applications, notamment la médecine nucléaire, l'énergie et la gestion des déchets nucléaires, ou la recherche sur la physique des neutrinos. En outre, des données précises sur les intensités d'émission de photons provenant de radionucléides se désintégrant par CE sont essentielles pour l'étalonnage des détecteurs de rayons X et de rayons gamma. Dans la littérature, la plupart des données sur la désintégration bêta et la CE proviennent de mesures anciennes ou de calculs théoriques présentant des incertitudes importantes ou sous-estimées. Les mesures récentes effectuées à l'aide de détecteurs cryogéniques ont mis en évidence ces divergences. Les calorimètres métalliques magnétiques (MMC) sont des détecteurs cryogéniques qui ont démontré des performances impressionnantes dans les mesures de spectres bêta, de l'énergie totale de désintégration et de rayons X et gamma. Ils se caractérisent par une résolution en énergie élevée, un seuil d'énergie très bas, une excellente linéarité en énergie et un rendement de détection de près de 100% aux basses énergies. Cette thèse utilise les MMC en mode de spectroscopie de l'énergie de désintégration, également connu sous le nom de mesure en géométrie 4π, pour mesurer les données de désintégration de radionucléides se désintégrant par transition bêta (^{14}C) ou par CE (comme le ^{125}I, ^{54}Mn, ^{59}Ni, et le ^{51}Cr). Une grande importance est accordée à l'étape de préparation de sources pour éviter les distorsions spectrales causées par certains types de sources radioactives. Les résultats obtenus ont montré une amélioration des incertitudes et sont en grande partie en accord avec les valeurs de la littérature et celles du code de calcul BetaShape.

université PARIS-SACLAY

ÉCOLE DOCTORALE
Particules, hadrons, énergie et noyau : instrumentation, imagerie, cosmos et simulation (PHENIICS)

Title: Measurement of nuclear decay data for beta decay and electron capture using metallic magnetic calorimeters

Keywords: Cryogenic detectors, Radionuclide metrology, Nuclear decay data, Decay Energy Spectroscopy, Fractional Electron Capture probability ratios, Beta spectrum

Abstract: Accurate fractional electron capture probabilities and beta spectra measurements are vital in radionuclide metrology. When determining the SI unit of activity, Becquerel, using primary activity measurements e.g . by Liquid Scintillation Counting (LSC), decay data on beta decay and electron capture are essential. These data are also crucial for validating theoretical calculations and for numerous applications, including nuclear medicine, nuclear energy and waste management or neutrino physics research. Additionally, accurate data on the photon emission intensities from radionuclides undergoing electron capture (EC) is vital for calibrating X-ray and gamma-ray detectors. In the literature, most decay data concerning beta decay and electron capture is derived from old measurements or theoretical calculations having large or underestimated uncertainties. Recent measurements using cryogenic detectors revealed these discrepancies. Metallic Magnetic Calorimeters (MMCs) are cryogenic detectors that have demonstrated impressive performance in beta spectra, total decay energy, and X-ray measurements. Their key features include high energy resolution, a low energy threshold, excellent energy linearity, and nearly 100% detection efficiency at low energies. This thesis employs MMCs in the Decay Energy Spectroscopy (DES) mode, also known as 4π measurement mode, to measure the decay data for specific radionuclides undergoing beta decay (like ^{14}C) and electron capture (such as ^{125}I, ^{54}Mn, ^{59}Ni, and ^{51}Cr). Emphasis is placed on the source preparation step to address spectral distortions that can arise from certain types of radionuclide samples. The obtained results showed improvement in uncertainties and are in large part in agreement with the literature values and those from the BetaShape calculation code.

Acknowledgement

The journey at LNHB-MA, CEA, and the process of writing this dissertation have been truly remarkable. Since my first day in October 2020, my supervisors, colleagues and friends at LNHB has provided a welcoming and conducive environment. Writing this dissertation would not have been possible (or half as much fun) without their support. I want to express my deepest gratitude to all those who have contributed to the completion of this doctoral thesis. This journey has been both challenging and rewarding, and I am thankful for the support and guidance I have received along the way.

First and foremost, I thank my supervisors, Martin Loidl and Matias Rodrigues, whose expertise, encouragement, and invaluable insights have been instrumental in shaping this research. They have been supportive since the very first day and motivated me during challenging times when progress seemed elusive. Both academically and emotionally, they stood by me through the ups and downs of navigating the intricate path leading to the completion of this thesis. They gave me moral support and the freedom to wander intellectually, with only an occasional tug on my sleeve to bring me back to the topic. There were numerous occasions where I felt disheartened and stumped about the direction of my research, but inevitably, a meeting with them would reinvigorate my enthusiasm and raise my spirits immeasurably. Their steadfast support and intellectual guidance—from start to finish—have been invaluable over the years, and I feel incredibly privileged to have them as my supervisor. Your unwavering commitment to excellence has been a constant source of inspiration to become an independent researcher.

I am also indebted to my thesis committee members, Loredana Gastaldo, Philippe Dessagne, Jean-Luc Sauvageot, and Frédéric Juget, for their constructive feedback and thoughtful suggestions. Their collective expertise has significantly enriched the quality of this work.

I would like to express my heartfelt thanks to Mark Kellett, the head of LNHB-MA, for graciously hosting me in the laboratory and fostering a warm and supportive atmosphere. There is no way to express how much it meant to me to be a LNHB member. My gratitude extends to my esteemed colleagues: Marie-Christine Lépy, Yves Ménesguenm, Christophe Dulieu, Benoit Sabot, Valérie Lourenço, Christophe Bobin, Lucille Chambon, Sylvain Leblond, Xavier Mougeot, Valérie Detey, Sylvie Pierre and Yann Kergadallan who have not only inspired me but also offered encouragement, engaging discussions, and a strong sense of camaraderie throughout my doctoral program.

During my three years at LNHB, I have made some brilliant friends: Lokmann, Stephanie, Victor, Gael, Dilan, Triem, and Beatrice. They provided me with friendship, great conversations, an instant social life, and constant encouragement. The positive and joyful atmosphere created by my colleagues and friends has been a constant source of delight. Special thanks also go to my friends outside of the workplace: Kajal, Aravind, Harshit, and Anetka, who stood by me through challenging times, cheered me on and celebrated every milestone. I know I can be difficult to deal with at the best of times, but thank you for being there for me when I needed it.

I would also like to acknowledge the dedicated staff and state-of-the-art resources at LNHB, whose facilities and services have been essential to the progress of this research.

I would like to express my sincere gratitude to my family for their steadfast support throughout my academic endeavors. Their unwavering encouragement, empathy, and affection have supported me

during challenging and celebratory moments. I extend heartfelt thanks to my parents, Narinderpal Singh and Navdeep Kaur. My younger brother, Gursimran, has not only been a cherished sibling but also my closest confidant and steadfast companion. He patiently listened to my endless rants, offered love, support, and motivation, and played a crucial role in helping me navigate this period with positivity.

As this chapter concludes, I look forward to embracing new opportunities and facing future challenges, grateful for the support and collaboration of each individual and institution involved.

Thank you all for being an integral part of this academic journey.

Résumé étendu

Introduction

Cette thèse vise à mesurer les données de désintégration associées aux radionucléides se désintégrant par désintégration bêta et capture d'électrons (CE). Des mesures précises des probabilités fractionnelles de capture d'électrons et des spectres bêta sont nécessaires dans divers domaines tels que la métrologie des rayonnements ionisants, la médecine nucléaire, la physique des neutrinos, la quantification des déchets radioactifs, et pour la validation de calculs théoriques. Dans la littérature, les données compilées utilisables pour la CE et la désintégration bêta reposent principalement sur d'anciens calculs théoriques qui utilisent l'approximation du noyau gelé et manquent de descriptions explicites des processus d'ionisation multiples. En outre, les valeurs mesurées présentent des incertitudes importantes ou indéterminées, comme l'ont montré les récentes mesures effectuées avec des détecteurs cryogéniques.

Le LNHB-MA est le laboratoire national français de métrologie des rayonnements ionisants, il est responsable de la mesure primaire de l'activité. Le comptage par scintillation liquide (LSC) est la principale technique de de mesure d'activité pour certains radionucléides, il nécessite une connaissance précise de la forme du spectre bêta ou des rapports de probabilité fractionnelles de CE. Les incertitudes dans les probabilités de CE influencent directement l'incertitude qui en résulte dans les mesures d'activité effectuées par les méthodes du rapport des coïncidences triples aux coïncidences doubles (TDCR) ou CIEMAT-NIST dans la technique de LSC. Le LSC nécessite la forme du spectre bêta pour modéliser l'émission de lumière, en particulier dans le spectre des basses énergies, où le rendement de détection des scintillateurs diminue de manière significative, tout comme pour les autres détecteurs conventionnels. Le bilan d'incertitude de l'étalon d'activité doit tenir compte de la connaissance de ce paramètre. Une autre tâche importante de la métrologie des rayonnements ionisants consiste à déterminer et à évaluer les données nucléaires et atomiques et à mettre à jour les tables de données de désintégration.

Les probabilités fractionnelles de capture d'électrons sont également nécessaires en médecine nucléaire pour contrôler le débit de dose requis pour le traitement du cancer afin de minimiser les dommages causés à l'ADN dans les tissus sains environnants. Une autre application nécessitant des rapports de probabilité de capture d'électrons précis est l'utilisation d'isotopes de capture d'électrons à longue durée de vie pour les techniques de datation et la détermination de l'âge du système solaire. En outre, des données précises sur les intensités d'émission de photons des radionucléides soumis à la CE sont essentielles pour l'étalonnage des détecteurs de rayons X et de rayons gamma. Malgré leurs nombreuses applications, le nombre de radionucléides à capture d'électrons mesurés précisément est limité.

Les calorimètres métalliques magnétiques (MMC) sont des détecteurs cryogéniques qui ont démontré des performances impressionnantes dans les mesures de spectres bêta, de l'énergie totale de désintégration et de rayons X. Leurs principales caractéristiques sont une haute résolution en énergie, un seuil d'énergie bas, une excellente linéarité en énergie et un rendement de détection de près de 100 % à basse énergie. Cette thèse utilise les MMC en mode de spectroscopie de l'énergie de dés-

intégration (DES), également connu sous le nom de mode de mesure 4π, pour mesurer les données de désintégration de radionucléides spécifiques subissant une désintégration bêta (comme le ^{14}C) ou une capture d'électrons (comme le ^{125}I, ^{54}Mn, ^{59}Ni et ^{51}Cr). Les résultats obtenus sont comparés aux valeurs de la littérature et à celles du code de calcul BetaShape.

Principe de fonctionnement des MMC

Les MMC sont des calorimètres classiques. Les constituants de base d'un MMC sont un absorbeur où les particules incidentes déposent leur énergie, un capteur paramagnétique (thermomètre) en fort contact thermique avec l'absorbeur qui détecte l'élévation de température conséquente ΔT, et un lien thermique faible reliant l'ensemble absorbeur-thermomètre à un bain thermique maintenu à une température constante T_0. L'absorbeur et le thermomètre sont caractérisés par leurs capacités thermiques respectives C_a et C_s, le lien thermique par sa conductivité thermique G, et le couplage thermique entre l'absorbeur et le thermomètre par G_{a-s}. Ce n'est qu'à très basse température, typiquement <100 mK, que les capacités thermiques sont suffisamment faibles pour avoir une élévation de température mesurable, et les bruits thermiques suffisamment faibles pour obtenir un rapport signal sur bruit élevé. Le détecteur revient à sa température d'équilibre avec une constante de temps $\tau_d = (C_a + C_s)/G$.

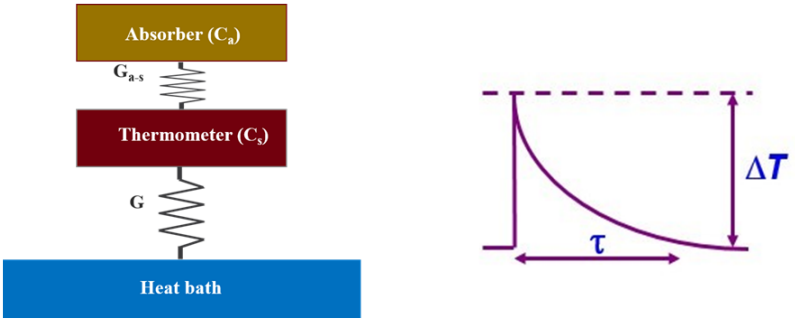

Figure 1: Les composants d'un MMC et la forme de l'impulsion.

Les MMC mesurent l'énergie des photons ou particules incidents individuels sous la forme d'une élévation de température. L'augmentation de la température modifie l'aimantation du capteur paramagnétique (Ag:Er ou Au:Er), ce qui entraîne une variation du flux magnétique. Le signal est lu (voir la figure 2) à l'aide d'un magnétomètre DC SQUID. Un transformateur de flux supraconducteur se compose d'une paire de bobines de lecture qui lit le signal du thermomètre paramagnétique et d'une bobine d'entrée qui couple ce signal au SQUID de lecture, le tout étant connecté dans un circuit supraconducteur fermé. Les bobines de lecture sont en Nb en forme de méandres et servent également à générer le champ magnétique pour aimanter le capteur en y gelant un courant parcourant les deux méandres.

La combinaison d'absorbeurs métalliques et de thermomètres métalliques magnétiques présente l'avantage d'un temps de montée du signal très rapide pour une capacité thermique donnée de

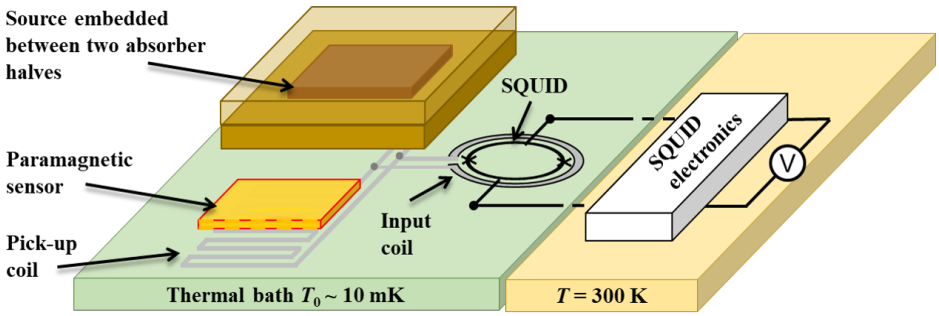

Figure 2: Circuit de lecture d'un MMC.

l'absorbeur. Si le contact entre l'absorbeur et le thermomètre est métallique, c'est-à-dire sans oxyde ou autre couche isolante, la chaleur transportée par les électrons de conduction peut se propager dans le thermomètre sans impédance thermique notable. Le couplage électron-spin dans le thermomètre est très rapide, l'équilibre thermique entre les électrons de conduction et les spins est généralement établi en moins d'une microseconde, même à des températures basses de l'ordre du mK. La résolution énergétique des MMC est déterminée par le rapport signal/bruit dépendant du temps et par la structure temporelle du signal. L'obtention de la meilleure résolution énergétique consiste à maximiser la taille du signal tout en minimisant le bruit afin d'obtenir le rapport signal sur bruit le plus élevé. La limite fondamentale de la résolution en énergie des détecteurs cryogéniques thermiques comme les MMC est le bruit induit par les fluctuations statistiques de l'énergie thermique entre l'ensemble absorbeur-senseur et le bain thermique. Une autre des principales causes de bruit des MMC, pas seulement à basse fréquence, est la contribution du bruit en 1/f attribuée aux ions Er dans le capteur de température. Le bruit total peut également être fortement influencé par le bruit blanc du SQUID, y compris le bruit de l'électronique du SQUID fonctionnant à température ambiante. Il limite donc le rapport signal sur bruit global et, par conséquent, la résolution énergétique du détecteur.

Optimisation du détecteur

La première étape de la mesure consiste à optimiser le détecteur. Dans un premier temps il s'agit de définir la géométrie de l'absorbeur et de la source. Au cours des deux projets EMPIR, MetroBeta et MetroMMC, cinq tailles différentes de puces de senseurs MMC ont été conçues par le Kirchhoff Institut für Physik (KIP) de l'université de Heidelberg en Allemagne, pour une large plage de gammes d'énergie. Pour maximiser le rapport signal-sur-bruit, les capacités thermiques de l'absorbeur et du thermomètre paramagnétique doivent être égales. À cette fin, des simulations de Monte Carlo sont effectuées à l'aide d'un programme appelé PENELOPE afin d'optimiser la géométrie du détecteur. Les simulations sont effectuées pour obtenir l'épaisseur appropriée de l'absorbeur dans lequel toute l'énergie de désintégration, à l'exception de celle du neutrino, est déposée. Le pouvoir d'arrêt (rendement intrinsèque) des absorbeurs de différents matériaux et géométries est calculé. Les résultats obtenus sont comparés entre eux pour sélectionner celui qui a la capacité thermique la plus faible et un pouvoir d'arrêt suffisant à la température de travail du MMC, c'est-à-dire 10 à 20 mK, obtenue

en utilisant un réfrigérateur à dilution pré-refroidi par de l'hélium liquide. L'étape suivante consiste à préparer la source et son intégration à l'intérieure de l'absorbeur pour les géométries optimisées à l'étape précédente. La préparation de la source est une partie importante de la mesure car la méthode de formation de la source peut affecter la forme du spectre. Si des cristaux de sel sont formés dans la couche source, les électrons émis lors du processus de désintégration perdent une partie de leur énergie dans le matériau source. Cette énergie ne serait pas entièrement convertie en chaleur détectable, ce qui entraînerait une distorsion du spectre et, par conséquent, en plus une dégradation de la résolution énergétique. Les sources à utiliser pour les mesures de 4π doivent être minces et homogènes pour permettre au rayonnement de traverser, avec une perte d'énergie minimale, le matériau de la source vers l'absorbeur. Trois techniques différentes de préparation des sources ont été utilisées dans cette thèse.

- Dépôt manuel de gouttes : méthode standard réalisée à l'aide d'une micropipette ou d'un pycnomètre. Dans cette méthode, une petite gouttelette d'une solution radioactive est déposée sur un substrat et elle est séchée pour former une fine couche de matériau radioactif. Les solutions de radionucléides typiques contiennent certaines charges de sel, ce qui signifie que le dépôt de gouttes conduit souvent à la formation de cristaux de sel de grande taille (de l'ordre du micromètre). Des études antérieures ont révélé que les cristaux de sel peuvent entraîner une distorsion considérable du spectre en raison d'une thermalisation incomplète de l'énergie des électrons. Cette méthode a été utilisée pour préparer les sources de $^{125}\mathrm{I}$ et de $^{14}\mathrm{C}$, mais sous des conditions très favorables évitant la formation de cristaux macroscopiques.

- Dépôt de gouttes à l'aide d'un distributeur de microgouttes : une approche permettant d'éviter la formation de gros cristaux de sel consiste à réduire la taille des gouttes individuelles à quelques picolitres. Le volume des gouttes peut être réduit à environ 50 pL à l'aide d'un distributeur de micro-gouttes. Cette méthode permet d'obtenir une grande reproductibilité avec une excellente précision en termes de volume et de positionnement. Pour améliorer encore la qualité de la source, au lieu d'utiliser une feuille métallique normale, une nanomousse d'or a été utilisée pour préparer la source. La solution remplit les cavités de la nanomousse et est séchée sur une très grande surface, ce qui permet d'obtenir un dépôt réparti finement. Cette méthode a été utilisée pour préparer les sources de $^{54}\mathrm{Mn}$ et $^{59}\mathrm{Ni}$.

- L'électrodéposition : Elle est basée sur le principe de l'électrolyse. Par électrodéposition, on obtient des sources très fines et homogènes. Lors de l'électrodéposition, si aucun dépôt métallique ne peut être obtenu, une couche d'oxyde ou d'hydroxyde se forme souvent. Il peut s'agir d'une source de haute qualité si la couche mince et homogène présente une très faible auto-absorption. Malheureusement, l'électrodéposition ne peut être utilisée qu'avec des métaux et le processus n'est pas universellement applicable ; il doit être adapté à l'élément désiré. Cette méthode a été utilisée pour préparer les sources de $^{54}\mathrm{Mn}$, $^{59}\mathrm{Ni}$ et $^{51}\mathrm{Cr}$.

Une fois les sources préparées, l'autoradiographie, basée sur la technologie de la plaque d'image au phosphore (IP), a été utilisée pour vérifier l'homogénéité et la distribution de l'activité des sources. Ensuite, la source de radionucléide à mesurer est placée entre les deux moitiés de l'absorbeur afin d'obtenir un angle solide de détection de 4π sr (géométrie 4π). L'ensemble absorbeur-source 4π est

soudé par diffusion à 400°C pendant 2 heures dans un four. L'ensemble absorbeur-source est collé au capteur à l'aide de l'époxy Stycast 1266 et les puces MMC et SQUID au support du détecteur à l'aide du vernis GE. Le bain thermique présent sur la puce du MMC sous forme d'un grand film mince d'or est thermiquement couplé au support en cuivre à l'aide de fils de bonding en or de 25 µm de diamètre (voir la figure 3).

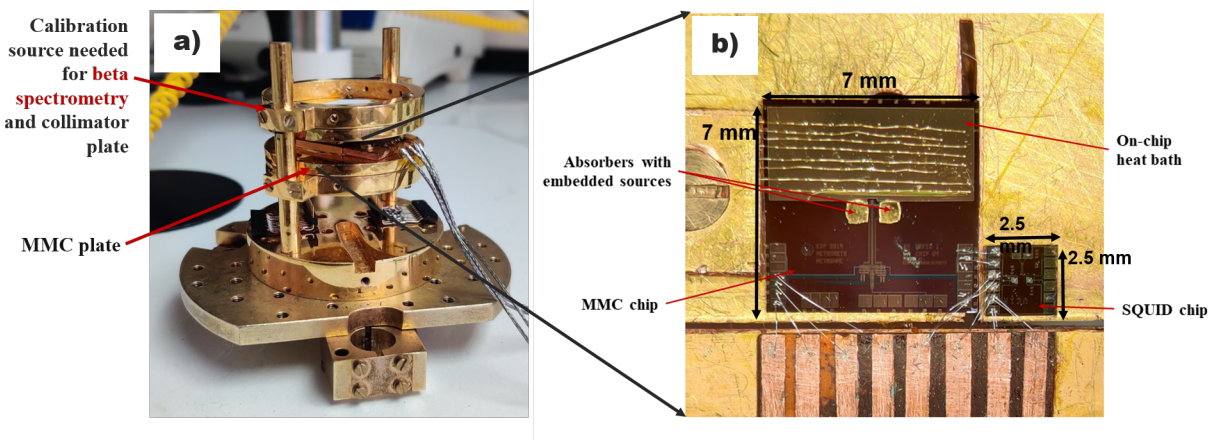

Figure 3: Configuration complète du détecteur.

Acquisition des données

La température de fonctionnement du MMC est de 10 à 20 mK, obtenue grâce au réfrigérateur à dilution. Les données de sortie de l'électronique du SQUID sont acquises en continu, généralement pendant deux à trois semaines, afin d'obtenir des statistiques suffisantes pour le spectre de décroissance. La tension de sortie analogique de l'électronique du SQUID Magnicon est amplifiée et filtrée à l'aide d'un filtre passe-bas ou passe-bande avec un amplificateur SR560 de Stanford Research Systems. La sortie de l'amplificateur SR560 est connectée à une carte d'acquisition PCI P25M d'Innovative Integration, qui numérise le signal. Les données obtenues sont analysées hors ligne à l'aide de routines de traitement des signaux écrites en MATLAB.

Les résultats

Dans une mesure de 4π d'un nucléide à capture d'électrons, la source est enfermée entre deux moitiés d'absorbeur. Dans le cas idéal, une seule raie est observée dans le spectre d'énergie pour chaque couche électronique sur laquelle la capture a lieu, correspondant à l'énergie de liaison de l'électron capturé. En effet, le détecteur additionne l'énergie totale émise dans une cascade d'électrons Auger et/ou de rayons X pour chaque désintégration individuelle. Le rapport des surfaces des pics correspond aux rapports de probabilité de capture fractionnelle d'électrons. Les rapports de probabilités fractionnelles de capture d'électrons pour ^{125}I, ^{54}Mn et ^{59}Ni mesurés sont comparés aux valeurs de la littérature et du code de calcul des formes de spectres bêta et de CE BetaShape. Ces valeurs sont

Table 1: Comparaison des valeurs mesurées avec le code BetaShape et la littérature.

Radionucléide	Ratios CE fraction-nelles	Cette thèse	BetaShape code	Littérature
^{125}I	$P_{\mathrm{L}}/P_{\mathrm{K}}$	0.2388 (26)	0.1947 (29)	0.23 (3), 0.2543 (27), 0.253 (5)
^{125}I	$P_{\mathrm{M}}/P_{\mathrm{K}}$	0.0575 (16)	0.0447 (22)	-
^{125}I	$P_{\mathrm{N}}/P_{\mathrm{K}}$	0.0156 (21)	0.0101 (10)	-
^{54}Mn	$P_{\mathrm{L}}/P_{\mathrm{K}}$	0.11320 (21)	0.11219 (31)	0.098 (6), 0.106 (3), 0.096 (5)
^{54}Mn	$P_{\mathrm{M}}/P_{\mathrm{K}}$	0.01686 (23)	0.01746 (11)	-
^{59}Ni-électrodéposé	$P_{\mathrm{L}}/P_{\mathrm{K}}$	0.1154 (11)	0.11590 (26)	0.1210 (20)
^{59}Ni-goutte déposée	$P_{\mathrm{L}}/P_{\mathrm{K}}$	0.1122 (22)	0.11590 (26)	0.1210 (20)

indiquées dans le tableau.

La mesure du spectre bêta du ^{14}C faisait partie du projet MetroBeta EMPIR et la première mesure a été effectuée en 2019. Lors de la mesure de 2019, une augmentation du spectre en dessous de 6 keV a été observée. Pour confirmer l'origine de cette augmentation, une nouvelle mesure utilisant la même source de ^{14}C a été effectuée pendant la thèse. Lors de la mesure de 2021, l'augmentation anormale n'a pas été observée. On peut conclure que la probabilité trop élevée aux basses énergies est due aux conditions expérimentales non optimales de la mesure de 2019. La mesure de 2021 peut être considérée comme fiable.

Conclusion

Dans cette thèse, les mesures ont été effectuées en utilisant la technique de spectroscopie de l'énergie de désintégration avec les MMC. Les résultats des mesures ont été comparés à la littérature et au code BetaShape. Trois méthodes différentes de préparation des sources ont été utilisées. Pour le ^{125}I, la valeur $P_{\mathrm{L}}/P_{\mathrm{K}}$ est en accord avec la seule mesure directe disponible dans la littérature, mais les valeurs ont montré une grande divergence par rapport aux valeurs récentes du code BetaShape et au reste des valeurs de la littérature. Cela est dû à la diminution de l'épaisseur de l'absorbeur pendant la phase de préparation du détecteur, de sorte qu'une nouvelle mesure est nécessaire. Pour ^{54}Mn et ^{59}Ni, un bon accord a été observé entre MMC, BetaShape et les valeurs de la littérature. Pour le ^{59}Ni, une comparaison entre deux spectres de désintégration de sources différentes a permis d'identifier la meilleure méthode de préparation de la source pour une excellente résolution en énergie et des distorsions minimales du spectre. La comparaison a montré que l'électrodéposition est supérieure à la méthode de distribution par microgouttes, même si une nanomousse est utilisée à la place d'une feuille métallique pleine comme substrat. Pour la mesure du spectre bêta du ^{14}C, l'augmentation

inattendue en dessous de 6 keV observée dans le spectre de 2019 n'a pas été observée. Au cours de cette thèse et des autres mesures effectuées au groupe des détecteurs cryogéniques du LNHB, il a été observé que les statistiques de faible comptage limitent la comparaison des spectres expérimentaux avec les calculs théoriques et les paramètres de désintégration fondamentaux. Afin d'améliorer les incertitudes statistiques, un nouveau spectromètre multicanal a été conçu. Il s'agit d'une conception complètement modulaire qui peut mesurer 10 détecteurs simultanément tout en facilitant le changement des puces individuelles de MMC ou de SQUID. Les MMC et les SQUID sont placés sur des structures de support séparées ayant un espace étroit (0.1 mm) entre eux pour avoir un couplage thermique minimum entre les MMC et les SQUID, afin de minimiser le chauffage des MMC par la dissipation d'énergie dans les SQUID. Avec cette nouvelle configuration du spectromètre, des statistiques de comptage de l'ordre de 10^8 sont attendues dans les quelques semaines de prise de données.

Contents

List of Figures

List of Tables

1 - Introduction

1.1 . Motivation

In the expansive field of nuclear science, the field of radionuclide metrology serves as the foundation for a standardized radioactivity measurement system. Natural and artificial radionuclides are identified by their emitted particles and photons during decay. The accuracy of these measurements partially relies on the precise knowledge of nuclear decay data and calibrations of detectors that are traceable to SI units. In ionizing radiation metrology, the primary standards are the measuring tools and procedures delivering the best achievable precision or the lowest achievable uncertainty without requiring any calibration. The primary task in ionizing radiation metrology is introducing new standards while maintaining and improving current ones, especially for dose (measured in Gray) and activity (measured in Becquerel) units. The essential tools to convert nuclear detector count rates to SI-traceable activities are also developed. An additional pivotal aspect of ionizing radiation metrology is determining and evaluating nuclear and atomic data, including data like decay schemes, half-lives, emission probabilities, and certain nuclear and atomic coefficients. The precision in determining this data often depends on the measuring instruments. To select the best instrumentation and method for a specific radionuclide standardization, previous knowledge of nuclear decay data is required.

As an example, liquid scintillation counting is a primary measuring technique used for beta-decaying radionuclides, but it requires a precise beta spectrum shape, especially in the low-energy region. The detection efficiency usually reduces in the low-energy region. The detection efficiency calculation depends on spectral shape knowledge both in the Triple-to-Double Coincidence Ratio (TDCR) and in the CIEMAT-NIST methods. In a similar way, for nuclides decaying via electron capture, data on fractional capture probabilities are needed. Also, experimental data is needed to improve the theoretical calculation of beta spectra.

Most of the experimentally measured beta spectra employed electrostatic or magnetic spectrometers, which exhibit low detection efficiency and a non-linear response to energy. These instruments also necessitate high-activity sources, resulting in energy loss of the beta particles within the source itself. In the case of solid-state detectors, the energy loss of beta particles in the dead layers and backscattering also lead to spectrum distortion. For the case of radionuclides decaying by electron capture, the number of measured radionuclides is limited. The compiled usable data is in large part based on old theoretical calculations using the frozen core approximation with no explicit description of multiple ionization processes, and the measured values have large or undetermined uncertainties. The uncertainties in EC probabilities directly impact the resulting uncertainty in activity measurements performed by The triple-to-double coincidence ratio (TDCR) method in the liquid scintillation counting (LSC) technique. The fractional electron capture probabilities are also needed in nuclear medicine to control the required dose rate for cancer treatment to minimize DNA damage in surrounding tissues. Another application that requires accurate EC probability ratios is the use of long-lived EC isotopes for dating techniques and determining the age of the solar system. Despite their broad applications, the associated decay data, like the fractional EC probabilities and vital atomic data, including fluorescence yields and emission probabilities for X-rays and Auger electrons, still needs significant improvements.

This thesis work's main objective is to measure the decay data associated with radionuclides decaying by beta decay and electron capture. In the first chapter, the different radioactive decay modes and the decay data related to them are presented. Some of the conventional detectors used in the literature for the previous measurements are also mentioned, along with some of their shortcomings. Different types of cryogenic detectors are described, and the main points which lead to the use of Metallic Magnetic Calorimeters (MMCs), one of the varieties of cryogenic detectors, to perform accurate measurements, are also discussed. The second chapter focuses on the physics and operation of MMCs. The third chapter discusses the details of how the experiments are performed. All the source and absorber preparation techniques for each measured radionuclide are described step by step. The fourth chapter is about the analysis of the measurements and the results obtained, along with their comparison to the values in the literature and from the theoretical calculations. Finally, the thesis work is summarized, and the perspectives are detailed.

1.2 . Different radioactive decays

1.2.1 . Alpha decay

Alpha decay is a spontaneous process during which a highly energetic $^{4}\mathrm{He}$ nucleus (α- particle) is emitted. During this nuclear transformation, the system moves to a lower energy state, and the daughter nucleus has two protons and four nucleons fewer than the parent nucleus. It is represented as:

$$^{\mathrm{A}}_{\mathrm{Z}}\mathrm{X} \rightarrow ^{\mathrm{A-4}}_{\mathrm{Z-2}}\mathrm{Y} + \alpha$$

The repulsive electrostatic force between protons has an unlimited range, and the disruptive force in a nucleus is roughly proportional to the square of atomic number. The short-range strong nuclear force narrowly balances the mutual repulsion of their protons in nuclei with A > 210. Alpha decay happens in such nuclei to reduce their size and increase the stability of the resultant nuclei after the decay. During the decay, inside the nucleus, two protons from the topmost proton energy levels and two neutrons from the peak neutron energy levels come together to form an α-particle, a state referred to as a "quasi-bound-state". This α-particle has an energy roughly equivalent to Q_α in the equation 1.1, with minor deviations due to the nuclear recoil being ignored.

$$Q_\alpha = (m_\mathrm{X} - m_\mathrm{Y} - m_\alpha)c^2 \tag{1.1}$$

In equation 1.1, m_X is the mass of the parent nucleus, m_Y is the mass of the daughter nucleus, m_α is the mass of the alpha particle and c is the velocity of light. The Q value has to be positive for alpha decay. The α-particle is held within a potential well formed by the powerful, short-distance nuclear forces. Simultaneously, there exists a Coulombic repulsion between this 'quasi-' α-particle and the remaining part of the nucleus. Together, these constitute a potential barrier whose height, V_c, is the Coulomb potential at the nucleus' radius, R (where the strong interaction is rapidly attenuated) [1]. The potential barrier height is represented mathematically in the equation 1.2, where Z_e is the electric charge of the daughter nucleus. The particle does not have enough energy to overcome this barrier using classical physics, but it can do it via quantum tunneling.

$$V_{\mathrm{c}} = \frac{2Ze^2}{4\pi\epsilon_0 R} \tag{1.2}$$

In heavy elements, the alpha particle would need a minimum kinetic energy of about 3.8 MeV to "tunnel through" the potential well.

1.2.2 . Beta decay and electron capture

The first evidence of radioactivity was Henri Becquerel's unforeseen discovery of electrons from the fogging of a black paper covering the photographic plate, which was placed adjacent to a uranium salt substance in 1896. He was studying the fluorescence of uranium salts and decided to explore the possible relation between X-rays, discovered a year before, in 1895, by Wilhelm Röntgen, and the fluorescence [2]. In 1898, G. C. Schmidt observed the emission of radiation from Thorium [3]. Marie Curie and Pierre Curie also observed the spontaneous emission of radiation from Thorium and new elements called Radium and Polonium. Marie Curie named the process "Radioactivity" in 1898 [4].

The separation between radioactive emissions was done by Ernest Rutherford in 1899, designating them Alpha and Beta rays based on their ionization and penetration strengths [5]. The name "gamma-rays" was given by Rutherford in 1903 to describe a form of radiation that Paul Villard first observed in 1900 as being even more piercing than the already known radiations [6]. These researchers showed that there are three different forms of radiation: alpha (the helium nuclei), beta (electrons), and gamma (the energetic photons). James Chadwick later demonstrated in 1914 that the beta radiation spectrum, i.e., the emission intensity of electron's energy, is continuous. This spectrum seemingly contradicted the principle of energy conservation. To solve this mystery, a new hypothesis in 1930 by Wolfgang Pauli proposed that a new kind of particle is emitted with beta decay to preserve the principle of energy conservation. Enrico Fermi gave the name 'neutrino' in 1933. Still, it was only detected later in 1956 by F. Reines and C. Crown when they observed the interaction of neutrinos emitted from a nuclear reactor with the protons of the water [7]. The discovery of the opposite process of beta decay, the capture of an electron by a nucleus from its atomic orbital, occurred in 1937 when Luis Alvarez first observed K-electron capture in ^{48}V [8]. But its theory was first discussed in the 1934 paper by Gian Carlo Wick [9]. Bethe, Bacher and Moller developed the electron capture theory based on the works of Fermi and Yukawa [10, 11].

There are thousands of nuclei that can be created and investigated in labs; out of these 1000s, about 251 are stable nuclei, and the remaining unstable nuclei are termed radioactive nuclei or radionuclides. The radionuclide that has either additional protons or extra neutrons converts to stable nuclei through the process of radioactive decay. The nuclide chart, as shown in Figure 1.1 [12], plots the stable as well as radioactive nuclides with the value of Z (atomic number) on the Y axis and the value of N (number of neutrons) on the X axis. In the chart, the isotopes (equal number of protons but different number of neutrons) are placed on the horizontal lines. On the vertical lines, the isotones (equal number of neutrons but different number of protons) are placed. The black line from the bottom left to the upper right shows a small number of cases of stable nuclei.

Generally, the primary decay type for particular nuclides is given by which one moves the nucleus closer to the line of stability. During an alpha decay, a helium nucleus is emitted, so the daughter nucleus is two places left and two places down from to the parent nucleus. In the Figure 1.1, the nuclei decaying by alpha decay are found in the upper right of the chart because the Coulomb potential is

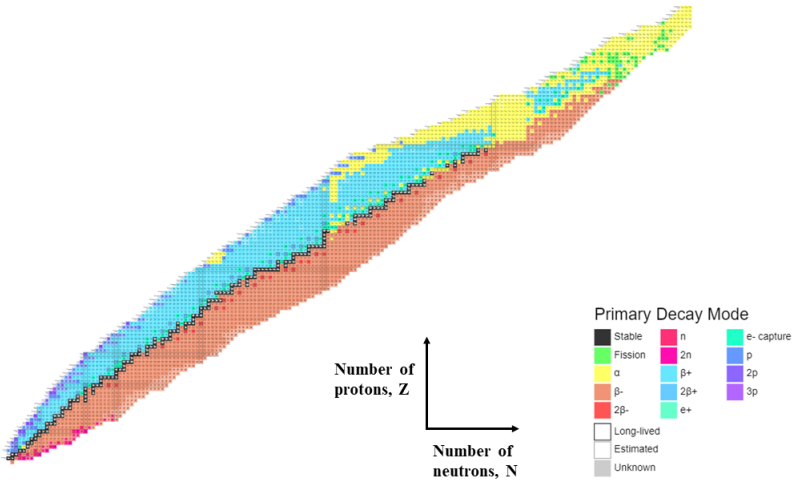

Figure 1.1: Nuclide chart [12].

more or less proportional to Z, so in lighter nuclei, it is too small for the alpha particle to tunnel out of the nucleus. The nuclide chart reveals that there are fewer nuclei undergoing alpha decay (shown in yellow) compared to those undergoing beta decay (represented in blue and orange). This difference is primarily because, in beta decay, a neutron can spontaneously transform into a proton, electron, and antineutrino, all within the nucleus. This transformation is steered by the weak nuclear force, not the strong nuclear force that binds the nucleus. There's no need to overcome a Coulomb barrier in this interaction. Many unstable nuclei reside in regions where alpha decay isn't prominent, and they typically undergo some form of beta decay to achieve stability.

The second-most ionizing radiation released by uranium gave rise to the term "Beta Decay." It was initially thought to be fast moving electrons [13]. Nevertheless, there were three main disagreements, with the beta decay being the electrons emission:

1. The non-conservation of energy as the continuous spectrum of distribution of beta particles' energy, from being maximum at Q-value down to zero, contradicts this law.

2. The non-conservation of angular momentum as the electron spin is ½, but the change in nuclear spin must be an integer.

3. The non-conservation of the quantum number called lepton number upon the emission of a single electron.

The introduction of the neutrino solved the above three contradictions. Enrico Fermi proposed a theory of beta decay, including the neutrino presuming it to be massless and chargeless [14]. The relation proposed by him is known as Fermi's Golden Rule, which treats beta decay as a transition that depends on the degree of coupling between the initial and final states. The transition probability λ_{if} is written as $\lambda_{if} = \frac{2\pi}{\hbar}|M_{if}|^2\rho_f$, where M_{if} is the matrix element for the interaction and ρ_f is the density of final state [14]. It was hypothesized that the neutrino must be a minuscule neutral antiparticle with a half-integer spin that is a lepton and responsible for carrying away the extra energy.

Hence, beta decay is a weak interaction disintegration process between two neighboring isobars sharing the energy and momentum of the process between the recoil daughter nucleus, neutrino/antineutrino, and positron/ electron. There are three types of decay modes under the category of beta decay: β^-, β^+, and electron capture (EC). These decay modes can be represented in three ways: the general physics view (in parent and daughter atom), nuclear physics (proton and neutron), and the fundamental or particle physics view (in quarks and bosons) [1]. The three modes are discussed in detail below.

1.2.2.1 . Beta minus (β^-) decay

In the case of a radionuclide where the number of neutrons is larger than that in the stable isotopes, the radionuclide achieves optimal neutron/proton ratio with the conversion of a neutron to a proton inside the nucleus and emissions of an electron, and an antineutrino. Hence, the name beta minus decay. It can be viewed as the following

- In general physics view: ${}^{A}_{Z}\mathrm{X} \rightarrow {}^{A}_{Z+1}\mathrm{Y} + \beta^- + \bar{\nu}_\mathrm{e}$, A= Mass number, Z= atomic number, X=Parent nucleus, Y= daughter nucleus, $\bar{\nu}_\mathrm{e}$= electron antineutrino.
- In nuclear Physics view: n$\rightarrow$ p + $\mathrm{e}^- + \bar{\nu}_\mathrm{e}$, n = neutron, p = proton
- In particle physics view: d$\rightarrow$ u + $\mathrm{e}^- + \bar{\nu}_\mathrm{e}$, d= down quark, u = up quark

The maximum β^- energy is represented as : $E_{\beta-max} = Q - E_l$. Here we ignore the nuclear recoil energy, that is of the order of eV, compared to the beta energies in the range of keV to MeV.

- E_l is the energy level of the daughter nucleus until which the decay occurs.
- Q is the total disintegration energy (difference between atomic masses of ground state of parent and daughter atom).

1.2.2.2 . Beta plus (β^+) decay

β^+ decay happens in those radionuclides where the number of protons is larger than that of the stable isotopes. The radionuclide achieves optimal proton/neutron ratio with the conversion of proton to neutron inside the nucleus and emissions of a positron and a neutrino. It is also termed a positron emission process. It can be viewed as the following:

- In general physics view: ${}^{A}_{Z}\mathrm{X} \rightarrow {}^{A}_{Z-1}\mathrm{Y} + \beta^+ + \nu_\mathrm{e}$, ν_e= electron neutrino.
- In nuclear Physics view: p$\rightarrow$ n + $\mathrm{e}^+ + \nu_\mathrm{e}$
- In particle physics view: u$\rightarrow$ d + $\mathrm{e}^+ + \nu_\mathrm{e}$

The maximum β^+ energy is represented as : $E_{\beta+max} = Q - E_l - 2m_0c^2$, $2m_0c^2 = 1.021998$ MeV, m_0 is the rest mass of electron. This extra term comes from the fact that β^+ transition occurs only if $Q - E_l > 2m_0c^2$.

1.2.2.3 . Beta spectra

The beta spectrum is a continuous energy distribution extending from 0 to $E_{\beta max}$. The transition energy is shared between electron (positron), neutrino (antineutrino), and for a small portion, the nuclear recoil energy that arises from the momentum conservation between electron and nucleus. The initial and final nuclear states have well-defined total angular momenta with quantum numbers J_i and J_f. L_β is the orbital angular momentum quantum number and the intrinsic spin quantum number is S_β with the value of 1, -1, or 0. According to the law of total angular momentum conservation: $J_i = J_f + L_\beta + S_\beta$ and $\Delta J = J_i - J_f$. The allowed transitions have $L_\beta = 0$, while the forbidden transitions have$L_\beta = n$, where n is the order of forbiddenness. The parity relationship is $\Delta\pi = \pi_f\pi_i = (-1)^L$. These parameters define the different beta decay transitions. The classification of beta decay is shown in table 1.1.

Table 1.1: Table of classification of beta decay.

Type	Forbiddenness	ΔJ	Δπ
Super allowed		0	+1
Allowed		0,±1	+1
Forbidden unique	First	±2	-1
	Second	±3	+1
	Third	±4	-1
	Fourth	±5	+1
Forbidden Non-unique	First	$0,\pm1$	-1
	Second	±2	+1
	Third	±3	-1
	Fourth	±4	+1

In some of the isotopes, beta decay can populate different states: the ground state and/or excited states of the daughter nucleus. This is referred to as branching in beta decay. The branching ratio corresponds to the ratio of relative populations. Higher Q-values imply that the decay is energetically more favorable, meaning that the decay will occur more often and faster (shorter half-life). In the case of multiple possible decay channels, the branching ratio of a specific decay mode will generally increase with increasing Q-value of that decay mode, all other factors being equal. The branching ratio is also used in calculating log (ft). The comparative partial half-lives ft are used to derive information on the shape factors of the beta transitions and on the different level spins and parities. A theoretical beta spectrum is produced by the weak interaction coupling constant g, the statistical phase space factor that depicts the momentum distribution between the electron and neutrino, the Fermi function F that accounts for Coulomb effects, and the shape factor C that contains the relevant nuclear structure information [15, 16]. The number of beta particles N emitted per unit of time with the energy W, in the range between W and $W + dW$, defines the shape of the spectrum as

$$N(W)dW = \frac{g^2}{2\pi^3}\eta W(W_0 - W)^2 F(Z,W)C(W)dW \tag{1.3}$$

W is the normalized energy with value $1 + \frac{E_k}{m}$

E_k is the kinetic energy of the particle
m is the electron rest mass
η is the normalized momentum with value $\sqrt{(W^2-1)}$
W_0 is the normalized endpoint energy of the particle with value $1+\frac{E_{max}}{m}$
E_{max} is the endpoint energy of the beta particle
Z is the daughter nuclei's atomic number.

The nature of the transition, which can be "allowed" or "forbidden," depending on the structure of the nuclei involved and certain atomic processes influence the shape of the beta spectrum. In the case of allowed and unique forbidden transition, the theoretical shape factor can be directly evaluated as an energy function. The energy-independent component only appears as a normalization factor in calculating the beta spectrum shape. It can be ignored with the assumption that the contribution of the leptonic wave functions throughout the entire space may be substituted by their value at the nuclear surface. In contrast, it is much more complicated for non-unique forbidden transitions as various nuclear matrix elements of their Fermi functions are still unknown. The energy dependency of the nuclear matrix components cannot be ruled out in forbidden non-unique transitions, which substantially complicates the computation of the beta spectral forms [15, 16]. In this thesis, the beta spectrum of $^{14}\mathrm{C}$ is measured and compared with the theoretically calculated spectrum from the BetaShape program [17] developed at LNHB.

1.2.2.4 . Electron capture (EC)

In this decay mode, the proton-rich nucleus of the electrically neutral atom captures an inner shell electron, hence the conversion of a proton into a neutron with the emission of an electron neutrino. The EC decay mode competes with the beta plus decay mode. The emission of the positron is only possible if the energy released during the decay is 511 keV (rest mass energy of positron) or more. If the energy is not sufficient, electron capture is the only process via which the excess of protons is reduced. Also, EC produces only two bodies after the decay with respect to the three-body formation in β^-or β^+ decay [13]. It can be viewed as the following:

- In general physics view: ${}^{A}_{Z}\mathrm{X}+\mathrm{e}^- \rightarrow {}^{A}_{Z-1}\mathrm{Y}+\nu_\mathrm{e}$.
- In nuclear Physics view: $\mathrm{e}^- + \mathrm{p} \rightarrow n + \nu_\mathrm{e}$
- In fundamental physics view: $\mathrm{u}+\mathrm{e}^- \rightarrow \mathrm{d}+\nu_\mathrm{e}$

As this is a two-body decay process, and the neutrino being the lepton and very much lighter than the daughter nucleus, it carries away most of the decay energy, resulting in a single characteristic energy, causing the daughter nuclei to recoil and have a single characteristic momentum. The EC process results in a vacancy in the shell (Figure 1.2), from where the electron was captured by the nucleus. This hole is then subsequently filled by an electron from a higher shell, leaving a new vacancy that is again filled by a higher shell electron, and so on. In doing this, the electrons move from higher to lower energy levels and release energy. This energy is monoenergetic for each change of electron shell and is emitted either in the form of characteristic X-ray photons (radiative decay) or another electron (non-radiative decay). This emitted electron is called an Auger electron. Auger electrons are preferred

in low atomic number elements, while for the higher atomic number elements, characteristic X-ray photon emission is more probable, at least when filling a K shell vacancy. Coster-Kronig transition is a special case in Auger transition where the electron transition can happen between two electronic subshells of the same shell [1].

Fluorescence yield, often denoted by the symbol ω, is a parameter that represents the probability of an atom undergoing radiative decay (emitting an X-ray photon) rather than non-radiative decay after an inner-shell electron vacancy has been created. For electron capture, the significance is that after the electron is captured by the nucleus, the resulting inner-shell vacancy can lead to either the emission of characteristic X-rays (with probability ω) or the ejection of Auger electrons (with probability $1 - \omega$), as mentioned above.

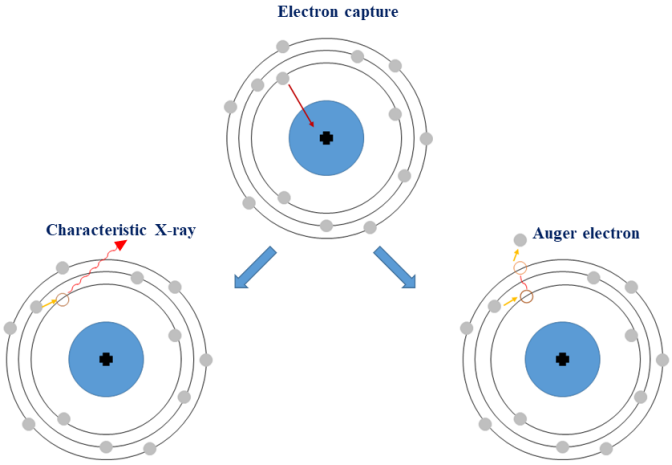

Figure 1.2: Representation of electron capture and subsequent atomic rearrangement processes.

If the electron capture results in the daughter nucleus being in an excited state, then the daughter nucleus deexcites to the ground state via the emission of the energy corresponding to the difference in transition energy levels. Again, this energy can be emitted either in the form of a gamma photon or by interacting electromagnetically with an orbital electron and causing the ejection of this electron from the atom. This latter process is called internal conversion. The energy of this electron is the energy difference between the initial and final nuclear states minus the binding energy of the electron. As in the case of electron capture, the emission of a conversion electron is followed by an atomic rearrangement, accompanied by the emission of X-rays and/or Auger electrons.

A fractional capture probability is the probability that the capture occurs on a given shell, K, L, M,... Fractional capture probabilities for an electron-capture transition (ε) of probability P_ε sum to unity: $P_\mathrm{K} + P_\mathrm{L} + P_\mathrm{M} + P_\mathrm{N} + \ldots = 1$. The probabilities strongly decrease from the lower to the higher shells, typically by about an order of magnitude between neighboring shells. P_K can be calculated from the ratios $P_\mathrm{L}/P_\mathrm{K}, P_\mathrm{M}/P_\mathrm{L}, \ldots$ as

$$P_\mathrm{K} = \left\{1 + \frac{P_\mathrm{L}}{P_\mathrm{K}}\left[1 + \frac{P_\mathrm{M}}{P_\mathrm{L}}\left(1 + \frac{P_\mathrm{N}}{P_\mathrm{M}}\left(1 + \frac{P_\mathrm{O}}{P_\mathrm{N}}\right)\right)\right]\right\}^{-1} \tag{1.4}$$

The primary contributions to P_{L}, P_{M} and P_{N} for allowed and non-unique first forbidden transitions comes from the L_1, M_1, and N_1 shells, respectively. However, capture from the L_2, M_2 and N_2 shells should be taken into consideration, although capture from other subshells may be overlooked [18,19]. The experimental calculated fractional capture ratio $P_{\mathrm{L}}/P_{\mathrm{K}}$ is the ratio of peak area of L and K capture peak, respectively, while, in the theoretical calculation, $P_{\mathrm{L}}/P_{\mathrm{K}}, P_{\mathrm{M}}/P_{\mathrm{K}}, P_{\mathrm{M}}/P_{\mathrm{L}}$ can be determined correspondingly from the ratio of transition energy along with the ratio for the correction factors for overlap and exchange effect [20].

EC is generally very difficult to observe due to difficulty in detection of the neutrino and the very small recoil energy of the daughter nuclei. However, the rearrangement in the electron shells happening after the electron capture paves the way to detect and study the electron capture. $^{163}\mathrm{Ho}$ is one of the most studied electron capture radionuclides worldwide [21–24]. It is used to study the mass of the electron neutrino, while the endpoint energy of the tritium beta decay is used for the tentative of measuring the mass of antineutrino [20, 26–28]. These two radionuclides are the only ones (the long-studied $^{187}\mathrm{Re}$ has turned out to be too difficult to measure) that offer a method without using the theoretical models to establish the precise size of neutrino masses. $^{163}\mathrm{Ho}$ decays via EC to $^{163}\mathrm{Dy}$ with a Q-value of 2.8 keV, which is the smallest known Q-value for EC transition. Due to this small maximum available decay energy, there is a constraint on the choice of the detector type. One of the best available techniques for this type of measurement is the calorimetric one. In the calorimetric measurement, having the EC nuclide embedded in the detector in a 4π geometry, the total energy of the rearrangement + recoil energy, i. e. the total decay energy except that of the neutrino, is measured. There are currently a few projects named ECHo, HOLMES, and NU-MECS that measure the calorimetric energy spectrum arising from the EC decay of $^{163}\mathrm{Ho}$ [23–28]. Finding the neutrino mass opens doors to physics outside of the Standard Model (SM), and the best upper limit on the effective electron neutrino mass is given as m_ν<0.8eV (90% CL) by the KATRIN collaboration [25–28]. This number obtained has effects on how the universe's large-scale structure has evolved throughout cosmic history. The methods of determining the neutrino mass include the direct kinematic measurements using $^{163}\mathrm{Ho}$ and indirect measurements of astrophysical phenomena that constrain the sum of the mass eigenstates through models of cosmic history. Except for this famous radionuclide, the research on the electron capture spectra of other radionuclides is very limited, and the available decay data is also scarce. One of the main works of this thesis is to measure the decay data of several radionuclides that decay via electron capture using the calorimetric technique.

1.2.3 . Deexcitation process

Deexcitation is the process by which an excited atom returns to a lower energy state, usually its ground state or a state close to it. Deexcitation is often associated with the release of energy from an atomic nucleus that has transitioned from a higher to a lower energy level in the context of radioactive decay. It can be categorized into gamma (γ) transition and atomic relaxation.

- Gamma (γ) transition

When a nucleus undergoes a radioactive decay or captures a particle, it often results in the nucleus being in an excited energy state. To return to its ground state or a lower excited state, the nucleus releases its excess energy in the form of electromagnetic radiation called as γ-rays (photon emission) or

as a conversion electron. The emitted energy corresponds approximately to the difference between the initial E_{i} and final E_{f} energy level of the transition. It is also named as the third primary decay along with α and β decay, but unlike these, it does not involve a change in the element.

- Atomic relaxation

Atomic relaxation is another type of deexcitation process resulting in a mono-energetic emission. Like after an electron capture event, there is a hole formation in the inner electron shell from where the electron was captured. This vacancy triggers a cascade of events: an electron from a higher energy shell fills the hole, releasing the energy difference between the two shells. This energy is either emitted as a characteristic X-ray photon or transferred to another outer-shell electron, ejecting it from the atom – the latter process is known as the Auger effect. The energy of the Auger electron is defined as the difference between the first transition and the Auger electron's original energy level before emission.

Atomic orbital notation is commonly used to express the various electron states that exist in an atom. In photon or X-ray spectrometry, a special terminology called 'Siegbahn notation' is used to denote the transition of of X-rays. If the electron jumps from L shell to K shell, the transition is called K_α X-ray emission and if it's from M shell to K shell, it's called as K_β X-ray emission. The pictorial representation is given in Figure 1.3.

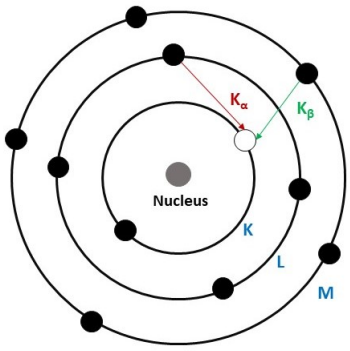

Figure 1.3: Pictorial representation of K_α and K_β X-ray spectral lines.

An electronic orbital's primary quantum number n is represented alphabetically by its letter, for example, K (n = 1; 1s), L (n = 2; 2s, 2p), and so on. The subscript on L and higher gives a unique designation to each of the different orbitals, which may have the same n but different l (angular quantum number), s (spin Quantum Number), or j (total angular momentum quantum number) quantum numbers, i.e., L_1 has quantum numbers $n = 2$ and $l = 0$, and so corresponds to the $2s$ orbital; L_2 is $2p(1/2)$ with $n = 2, l = 1, j = 1/2$ and L_3 is $2p(3/2)$ with $n = 2, l = 1, j = 3/2$, and so on in order of increasing energy. When a transition involves many orbitals. It is described by the spectroscopic notation of the orbitals. See the case for KL_1L_2 Auger electron transition in Figure 1.4.

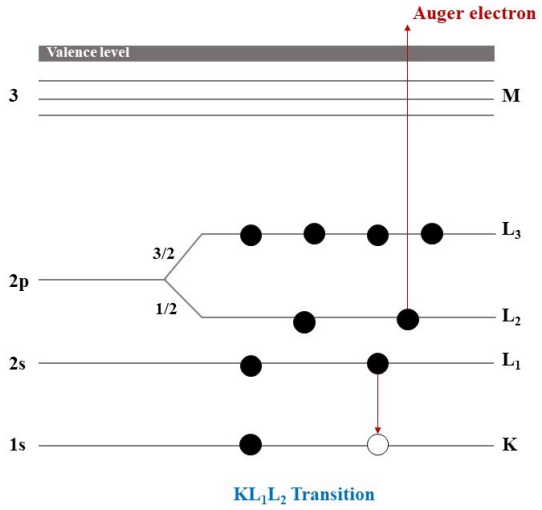

Figure 1.4: Spectroscopic notation of the orbitals for KL_1L_2 Auger electron transition.

1.3 . Ionizing radiation metrology

Ionizing radiation can be classified into two categories: electromagnetic (photon) and particle radiation. Their origin can be both natural and artificial sources. Ionizing radiation metrology is the branch of science that is responsible for measuring and implementing the units of the International System of Units (SI) in this field. The Laboratoire de Métrologie de l'Activité (LNHB-MA), CEA Paris-Saclay is one of the national metrology institutes federated by the Laboratoire National de métrologie et d'Essais (LNE). It is in charge of primary metrology for the measurement of activity (expressed as becquerel and its derivatives) along with being in charge of the evaluation and publication of nuclear and atomic data associated with the decay of radionuclides. The laboratory uses different detection methods to cover a wide range of activity according to emitter types (α,β,γ, X). This section discusses these detection methods in the context with the different radioactive decay types. A summary will present why metallic magnetic calorimeters are preferred in beta and electron capture spectrum measurements.

1.3.1 . Decay data

Decay data is an essential tool to characterize and quantify radionuclides. The nuclear and atomic data comprise the following characteristics:

- Half-life
- Decay modes: branching ratios, Q-values
- The energies and emission intensities (or probabilities) for alpha particles, beta particles, γ-rays, Auger- and conversion-electrons, X-rays, delayed-neutrons and protons.
- The energies of the atomic rearrangement process after electron-capture (EC) and transition/emission probabilities and transition, EC/β+ ratios

- Fluorescence yields and internal conversion coefficients
- Spontaneous fission properties (branching ratios, and recoil energies)
- Detailed quantification of the uncertainties related to all of the atomic and nuclear characteristics mentioned above.

To be able to use the radionuclides to their full potential, the precise details about their characteristics mentioned above are crucial. Hence, accurate measurements with in-depth assessments of the radionuclide decay data are required [29]. There have been major advancements in terms of experimental radiation detection techniques as well as theoretical calculations over the last few decades to identify and characterize the different decay processes as well as the properties of the daughter nuclei. These techniques provide an important route to our understanding of the structure of the nucleus and specifying the suitable nuclear application, like selecting the appropriate dose rate in nuclear medicine, radiation monitoring and protection, nuclear reactor shielding and waste management, astrophysics, fundamental nuclear physics research, etc. There are many non-nuclear applications of nuclear decay data in various industries, namely chemical, petroleum, automotive, electronic, metallurgical, and mining. A familiarity with half-lives, radiation energies, and emission probabilities is necessary for many of these applications. To ensure the precision and effectiveness of various radioactive items, including medical investigations and research-based developments, precise and reliable decay data are essential [30, 31].

The compilation of such data sets is a significant result of research projects conducted by national standards laboratories and other research institutions worldwide to evaluate radiometric methods and, as a result, the precision of many quantitative decay characteristics. Some of the nuclear decay databases are ENSDF (Evaluated Nuclear Structure Data File), NuDat (Nuclear structure and decay data), XUNDL (Experimental Unevaluated Nuclear Data List), etc. The creation of national and international databases of suggested decay data through compilation and evaluation helps with the development of reliable theoretical data and the establishment of radionuclides for use as standards and in nuclear applications. The suggested decay data in these multiple libraries are updated on a regular basis either by worldwide consensus or more locally focused initiatives depending on particular country requirements [32]. The Decay Data Evaluation Project (DDEP), which received assistance from several specialized and national laboratories- CEA/LNHB (France), PTB (Germany), INEEL (USA), KRI (Russia), LBNL (USA), NPL (United Kingdom), CIEMAT (Spain), CNDC (China), NIM (China), NIST (USA), IFIN-HH (Romania) - was established in 1995. It consists of a number of consented studies to compile high-quality files of recommended decay data. The Bureau International des Poids et Mesures (BIPM) has recommended the usage of these data, which include radionuclides important to radiation metrology [33]. The results from this project were published under the 'Table de Radionuclides,' [34] and they are updated regularly by the LNHB. An online library for gamma and alpha emissions called- 'Nucléide –Lara' is also published by LNHB [35].

The evaluation procedure is coordinated by the IAEA. The evaluators follow certain guidelines to determine if a given data value can be included in the decay data libraries. According to these guidelines, When there are several measurements of the same parameter, each measurement should not contribute more than 50% to the total value. If the experiment value is inconsistent, then a few other steps are taken, like the unweighted mean can be recommended, or some value can be rejected based

on the incorrect calibration methods or poorly specified measuring approaches used by the metrologist. Rather than the complete rejection of the measured value, a different approach to changing the weights is taken [29–32].

Among the different decay data mentioned in the previous paragraphs, this thesis is focused on the decay data associated with beta decay and electron capture. Electron capture probabilities and beta spectra will be measured using a metallic magnetic calorimeter and compared with the theoretically calculated data and the data available in the literature. From the literature, it was observed that some of the decay data currently being utilized are established using old theoretical calculation methods, and the usable compiled experimental data have shown certain divergences with the recent data acquired using cryogenic detectors [36]. This is particularly the case in radionuclides decaying by electron capture and beta decay. The decay data from the electron capture influence various fields like cancer treatment, the calculation of the age of the solar system, particle physics, and the fundamental research for updating primary activity standardization in metrology. When determining the activity of a radioactive sample containing beta-emitting isotopes, the beta spectrum shape is required, except for nuclides which can be measured by the beta-gamma coincidence method. A precise understanding of the beta spectra's forms can aid in reducing the uncertainty in activity measurements performed using e.g. the Liquid scintillation counting method [37]. The conventional detection techniques, including ionization and liquid scintillation detectors, have energy-dependent quantum efficiency and substantial limits in energy resolution. Metallic Magnetic Calorimeters (MMC) have proved to be an excellent alternative to conventional detectors in terms of detection efficiency, energy linearity, low energy threshold, and energy resolution.

1.4 . Detection techniques used for beta and electron capture spectrometry

Ionizing radiation has many applications in different sectors like health, industry, environment, fundamental research, etc. Ionizing radiation metrology is the science that comprises the measurement of radioactivity (activity expressed as becquerel and its derivatives) and dosimetry of charged photons and particles (absorbed dose, air kerma, and dose equivalents, respectively expressed in gray and sievert). It also includes experimental and theoretical techniques to determine the nuclear and atomic data associated with the decay of radionuclides. Accurate and reliable measurements are provided for the safe performance of ionizing radiation in different applications and to establish a national and international references for different types of radiation detections. So that the world can use nuclear technology with maximum reliability. The measurement of nuclear and atomic data comprising cross-sections, branching ratios, half-lives, emission probabilities, and photon interaction coefficients has been performed using well-established and highly reliable conventional detection techniques like semiconductor, scintillation detectors, or ionization chambers, and also non-conventional techniques like cryogenic detectors, high-pressure xenon spectrometers, liquid ionization and proportional counters, thermoluminescent dosimeters, activation detectors. In this section, the conventional detectors as well as cryogenic detectors used in the ionizing radiation metrology are discussed.

1.4.1 . Overview of conventional detection techniques

1.4.1.1 . Proportional counter

The proportional counter operates by filling a chamber with an inert gas, such as argon, and a small amount of a quenching gas like methane. An electric field is established in the chamber by applying a voltage between a central wire (anode) and the chamber walls (cathode). When ionizing radiation passes through the gas, it ionizes the atoms along its path, creating electron-ion pairs. The electrons are driven toward the anode by the electric field, and the positive ions drift towards the cathode. As the electrons approach the central wire, the electric field strength increases and the electrons gain enough energy to ionize further gas atoms, creating an avalanche of secondary ionizations. The key feature of a proportional counter is that the total charge collected (and thus the amplitude of the pulse produced) is proportional to the energy of the original ionizing radiation. This allows for energy measurement in addition to simple detection [1]. The operating principle is shown in Figure 1.5.

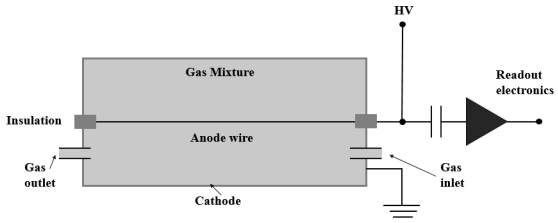

Figure 1.5: Proportional counter setup

There are three main types of proportional counters that are widely utilized. The first type, known as the gas flow proportional counter with a window, is commonly used for alpha and beta particle counting and the windowless is used for tritium measurements. The second type is called air proportional counter, used exclusively for alpha counting. The third type is called as sealed proportional counter, which uses gases like BF_3 or Helium-3 for neutron detection [38, 39]. The main disadvantage of using these counters is their limited energy resolution. The initial ionization event in the gas creates a number of electron-ion pairs that is statistically distributed. The subsequent multiplication of these charges in the gas amplification region also exhibits statistical variations. Both of these statistical processes follow a Poisson distribution, which can cause fluctuations in the output signal, thus limiting the energy resolution [40].

1.4.1.2 . Scintillation detector

A scintillation counter or detector involves a scintillator, i. e. a material that exhibits the phenomenon of scintillation, or light emission when excited by ionizing radiation. The excitation caused by the interaction of radiation and scintillator material results in flashes of varying intensity. The intensity of each flash is directly proportional to the incident radiation's energy [1].

A standard configuration involving scintillating detectors is shown in Figure 1.6. It contains the scintillator, where the incident particle deposits its energy, along its path the atoms are excited. If

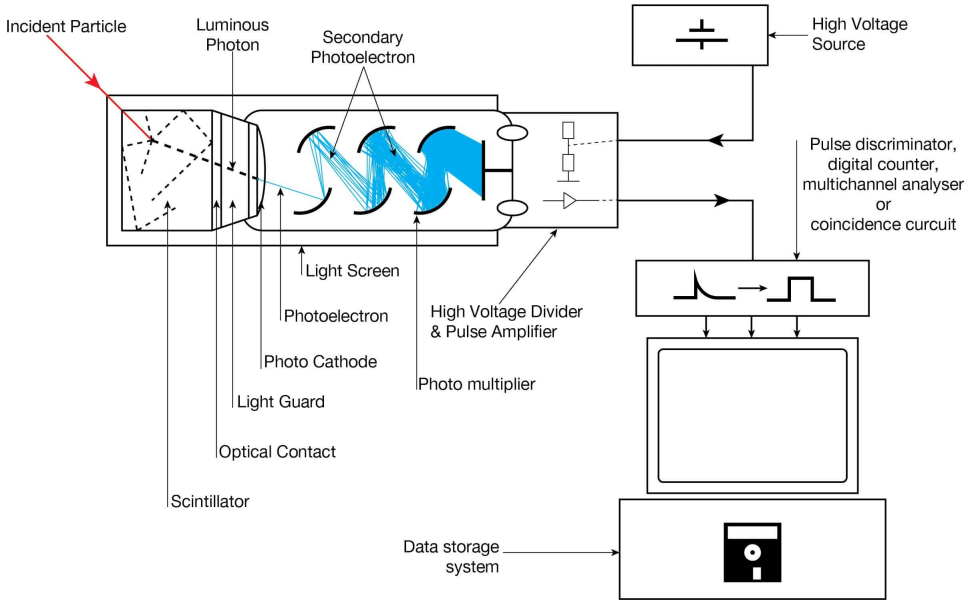

Figure 1.6: Scintillation detector technique

the incident radiation is charged then the track is the particle path itself. However, if the incident radiation is uncharged like in the case of gamma rays, the energy is converted to energetic electrons via Compton scattering, photoelectric effect, or pair production [1]. During the deexcitation process, light photons are produced. To transduce these luminous photons into an electrical signal and to amplify said signal, devices like a photo-multiplier tube (PMT), a charge-coupled camera, or a photo-diode are used.

In a PMT, photons generated from the deexcitation process interact with a photocathode, thereby releasing low-energy primary electrons. These primary electrons are then electrostatically accelerated and secondary electrons are released upon their interaction with the PMT's dynodes. The output electrical signal is a distinct, quantifiable pulse for each photon cluster produced from the first ionizing incident in the scintillator. This signal carries valuable information about the energy of the original incident radiation and is forwarded to a charge amplifier to integrate this energy information. As a result, the resultant signal is proportional to the energy deposited by the particle that excited the scintillator. The decay rate can be determined by counting the number of these pulses per unit time. The sensitivity of PMTs is quoted by their quantum efficiency, i.e. number of photoelectrons emitted per incident photons. Alternatively, photo-diodes, particularly silicon photodiodes are also utilized in place of PMTs. In a silicon photodiode, the incident light is absorbed in a thin layer of silicon, leading to the formation of electrons and holes, which are then collected. Photodiodes are commonly operated in the reverse bias mode.

Scintillation detectors incorporate a wide variety of scintillators, each with its own characteristics and strengths. One essential classification of scintillators is based on their state of matter. This comprises scintillators that are solid, liquid, or gaseous. Solid scintillators, for instance, come in organic and inorganic forms. Organic solid scintillators, usually comprised of single crystal or plastic materials, offer fast response times and excellent discrimination between neutron and gamma ra-

diation [41]. Inorganic scintillators, on the other hand, are made of materials such as sodium iodide (NaI) or thallium-doped sodium iodide [NaI(Tl)], have high-density and high-atomic-number features that lead to improved gamma radiation detection efficiency [42]. Liquid scintillators, typically organic compounds dissolved in an organic solvent, are known for their ability to measure low-level beta radiation. They offer greater flexibility in detector size and shape and possess faster decay times, enabling a higher count rate capability. There has been recent development of inorganic crystal-based scintillators (e.g., lanthanum bromide [$LaBr_3$] and cerium bromide [$CeBr_3$]), which are known for their high light output and relatively good energy resolution. The duration of the light flashes is extremely small, ranging from 10^{-9} seconds in organic scintillators to 10^{-6} seconds in inorganic scintillators, leading to the high count rate capability. The drawback of the scintillation counter is a modest energy resolution and the fact that some of the inorganic crystals used as a scintillator are hygroscopic.

1.4.1.3 . Semiconductor detector

Semiconductor detectors are another form of radiation detector that is widely utilized. This detector type uses semiconductor materials such as silicon and germanium. The semiconductor detectors exploit the response of the semiconductor to incident radiation when it is placed between two electrodes. The radiation path generates electron-hole pairs within the material, and the number of these pairs is proportional to the radiation's energy [1]. The charges are collected with the application of a voltage between two electrodes.

Silicon is commonly used for charged particle detection because of its narrow depletion width (active volume of the detector when applying bias voltage), roughly 1mm at maximum. This makes them an excellent choice for alpha spectroscopy. In contrast, germanium can reach a depletion width of up to 2 cm with a bias voltage of a few kV. So, germanium detectors can serve as total absorption detectors for gamma rays in the energy range of a few MeVs. The interaction probability of gamma radiation is also greater in the germanium detectors due to its higher atomic number than that of silicon resulting in superior photon detection efficiency and high resolution. The energy required to create an electron-hole pair in Silicon detectors is 3.6 eV, while for germanium, it is only 2.9 eV [43].

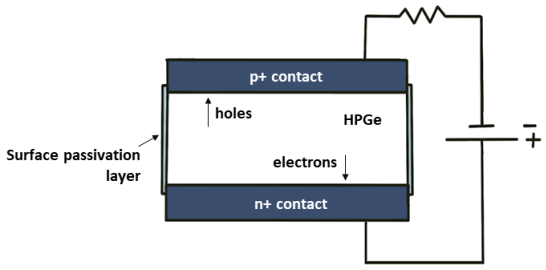

Figure 1.7: HPGe detector technique representation.

Semiconductor detectors work as solid-state ionization chambers, where charged particles produce electron-hole pairs instead of electron-ion pairs. In a semiconductor detector, the energy required to make electron-hole pairs is substantially less than necessary to generate electron-ion pairs, resulting in better energy resolution. The semiconductor crystal is sandwiched between two elec-

trodes, and a voltage is applied to these electrodes to generate an electric field. This field causes carriers (electrons and holes) to drift to their corresponding electrodes, generating a signal. Collecting electron-hole pairs before they recombine is the primary challenge with semiconductor detectors. This problem is frequently addressed by the use of highly pure semiconductor crystals. The two most commonly used types of semiconductor crystals used are intrinsic (high purity), like in High purity germanium detector (HPGe) (Figure 1.7) , and extrinsic (doped), like in Si(Li), Ge(Li), i.e., lithium doped silicon and germanium detectors. In intrinsic crystals, thermal or optical excitation of electrons to the conduction band generates charge carriers. Extrinsic crystals, on the other hand, rely on dopants occupying lattice positions to produce charge carriers.

Semiconductor detectors, used in diverse scientific fields, from macroscopic applications in astronomy to microscopic applications in nuclear medicine as radiation imaging tools, offer better energy resolution than gaseous or liquid detectors [44–46]. This is due to the smaller statistical variation of the pulse height. Their main limitation is the energy range; their performance declines beyond a few MeV energy. Scintillator detectors become a better option at these high energies as they can be made larger in size without affecting their energy resolution, which is not the case for semiconductors. Furthermore, large-size semiconductor detectors are difficult to fabricate due to the high purity requirements of the semiconductor material. Impurities can introduce defects in the detector, thereby degrading its performance.

1.4.2 . Limitations of the conventional detection techniques

The previous section briefly describes the conventional detection techniques for compiling the decay data tables. Along with their various advantages, each of these techniques has some limitations. Proportional counters being a type of gaseous ionization detectors have a limited dynamic range for energy measurement, which restricts the range of energies that can be measured accurately as well as low detection efficiency and poor resolution. For very high-energy radiation, they may not be the most suitable choice. They also have a limited energy resolution and suffer from the process of avalanche of secondary discharges. Proportional counters also observe the radiation damage effect on its components as prolonged exposure to high levels of radiation can lead to damage to the gas and the materials of the detector, which can degrade its performance over time. Some of the concerns of proportional counters, like energy range, can be improved using scintillation detectors. Crystal scintillators exhibit high stopping power for many types of radiation, including gamma rays and high-energy particles, leading to high detection efficiency, and as well provide rapid response times, often in the nanosecond range, making them suitable for applications that require fast timing resolution such as in time-of-flight measurements. Plastic and liquid scintillators are excellent choices when a large detection volume is required. The disadvantage of crystal scintillators is hygroscopicity like that of NaI crystal, leading to performance degradation if not stored or protected properly. One of the other significant disadvantages of scintillation counters is quenching. Quenching is a process that reduces the number of scintillation light photons produced following the absorption of ionizing radiation. This happens when certain factors or substances, known as quenching agents, absorb or divert the energy that would otherwise have gone into producing the scintillation photons. Two types of quenching may affect scintillation detectors:

- Chemical quenching: Certain chemical substances or impurities in the scintillator can absorb

the excited states produced by radiation, thereby reducing the number of photons emitted.

- Color quenching: If a colored or absorbing substance is present in the scintillator, it can absorb some scintillation light, thereby reducing the total light output.

Quenching can lower the detector's response to radiation, which means that the output signal is smaller than expected for a given radiation energy or dose. This can affect the detector's ability to measure the radiation energy or dose accurately. It is particularly significant when measuring low-energy radiation because quenching effects are more severe for low-energy radiation. In order to correct for quenching, calibration procedures are often employed. This usually involves measuring the detector's response to a known radiation source and adjusting the detector's response accordingly. Scintillation detectors also have high background counts in the case of NaI and plastic scintillators.

The semiconductor detectors require only a few eVs of ionization energy to create an electron-hole pair; hence, they have better energy resolution than both scintillation and ionization chambers. The common drawback of all these techniques is that the detection efficiency depends on the energy, and at low energies, the efficiency decreases quite rapidly. The other one is the limitation to the energy resolution that cannot be substantially improved. In the case of solid-state detectors, its surface leads to the self-absorption and backscattering of the electrons, hence the depletion of electron efficiency too.

In order to mitigate the inherent limitations associated with conventional detection techniques, non-traditional methods have been explored. A prominent example of such innovation is the development of cryogenic detectors, also referred to as cryogenic calorimeters or bolometers. These detectors are designed to operate at extremely low temperatures, specifically below 100 millikelvin (mK). At such low temperatures, the material's heat capacities are minimal and excitation levels in the microelectronvolt (μ eV) range become accessible for signal formation. One of the central motivations behind the development of cryogenic detectors was the quest for higher energy resolution combined with a lower energy threshold. Conventional scintillation and semiconductor detectors are constrained by statistical fluctuations in the number of signal carriers induced by radiation, which poses a limit on energy resolution. Operating at temperatures below 1 kelvin, cryogenic detectors effectively reduce these limitations.

These calorimeters are designed to measure the total energy deposition, which encompasses heat in the form of phonons, or quasi-particles in a superconductor. With an optimized detection system, they can achieve remarkably higher energy resolutions. This superior performance is attributed to the involvement of a large number of low-energy quanta (μeV to meV) in the detection process. At these low temperatures, a variety of solids offer low energy excited states, thereby increasing the signal carrier number with reduced excitation energy per carrier. Concurrently, thermal noises are significantly diminished, resulting in a high signal-to-noise ratio and further enhancing the overall energy resolution. Consequently, cryogenic calorimeters excel in detecting minute energy deposits on the order of electronvolts (eV), with resolutions that vastly surpass those of traditional detection systems. The mechanism underlying this detection involves the energy deposited during the interaction of a particle with a solid material. In the context of a calorimeter, a particle interaction in the absorber initiates a discernible rise in temperature. To precisely measure this temperature change, highly sensitive thermometers or temperature sensors are employed, which are particularly effective

at extremely low temperatures.

Common sensor choices include transition edge sensors (or superconducting phase transition thermometers), thermistors, or magnetic sensors. The specific concepts underlying various cryogenic detectors are elaborated in subsequent sections. One significant edge that low-temperature detectors hold over alternatives such as proportional counters, semiconductor detectors, or scintillation detectors lies in their near-unity detection efficiency for low-energy X-ray photons and electrons, as well as their energy linearity. Most of these advantages are primarily rooted in the sharp reduction in specific heat observed in all solids at low temperatures, coupled with lower thermal noise in both the detectors and the readout electronics at the cold amplifier stage. Furthermore, the wide selection of available absorber materials renders cryogenic detection techniques an especially appealing option for a range of applications [40–44].

1.4.3 . Overview of cryogenic detection techniques

The discipline of cryogenics studies the impacts of extremely low temperatures. The name cryogenics emerges from combining two Greek words, kryos representing frost and genic representing the production. The first time the term cryogenics was used in the context of permanent gas liquefaction was by Prof. Kamerlingh Onnes in 1894. The word cryogenics has come to mean temperatures below about –150 degrees Celsius. The compression and expansion of gases are utilized to achieve cryogenic temperatures. The rules of thermodynamics state that there is a limit to achieving the lowest temperature, known as absolute zero. At this absolute zero temperature, molecules or atoms are at their finite lowest energy state. According to the SI system, 0 Kelvin (K) corresponds to the absolute zero temperature. 0 K is the same as – 273.15 °C or –459.67 °F.

The applications of cryogenics are wide-ranging, from the use of cryogenic liquids in the medical field, in the food industry for preservation, in fundamental research, and are incorporated with the developments in the other fields of science and technology. The calorimetric detection of energetic particles, or more generally, thermal detection of radiation, has a long history in physics. The first law of thermodynamics serves as its foundation. The development of cryogenic detectors was intertwined with the pursuit of new and improved ways of particle detection with higher resolution and quantum efficiency in radiation spectroscopy. One of the main driving forces for the development of cryogenic particle detectors was the expectation that they would show excellent sensitivity to weakly interacting particle interactions. In recent decades, various cryogenic detectors have been developed and tested experimentally for basic physics experiments and other applications. All of these detectors exhibit one characteristic: they are extremely sensitive to the interaction of a single particle. This sensitivity is because solid-state systems are less influenced by lattice vibrations inside their crystal structure at low temperatures. In the thermal calorimeter, the decreased background noise from thermal vibrations allows for detecting small temperature changes induced by a very low-energy particle [47, 48].

The first suggestion to use thermal detectors for detecting radiation with their increased sensitivity at low temperatures was made by F. Simon in 1935 [49]. In the early 1980s, a group of physicists proposed to use cryogenics in detecting low-energy particles by using a superconducting calorimeter. The reduction of thermal noise and the ease with which quantum-mechanical processes could be accessed at cryogenic temperatures are the fundamental drivers behind the development of low-temperature sensors, as superconductivity is a quantum occurrence that happens at low tempera-

tures and plays a vital role in the development of near-equilibrium cryogenic detectors. Superconducting materials are used in their sensing components as part of the cryogenics for support and frequently in the cryogenic circuits that make arrays of sensors available. When going through the history of the development of cryogenic detectors, the following applications were where their usage was targeted [47, 48].

1. High energy resolution for the radiation spectroscopy: In X-ray spectroscopy, for the low energy X-rays (E< 10 keV), high-energy resolution detectors, with energy resolution less than 10 eV, was required. In 1984, McCammon et al. and Moseley et al. developed the thermal X-ray microcalorimeter, which observed an energy resolution of 7.3 eV at 6 keV [50, 75]. During the same period, LLNL and ESA proposed the cryogenic detector using STJs for X-ray astronomy.

2. Observation of the solar neutrino's low-energy spectrum: A 1984 proposal by Drukier and Stodolsky postulated neutrinos could be detected when coherently scattered off nuclei within superheated superconducting granules. This method could yield cross sections many orders of magnitude greater than single neutrino-nucleon scattering. Additionally, Booth suggested using superconducting indium as both a target and a detector for neutrinos, leveraging the Cooper pair-breaking mechanism inherent to superconducting detectors. This would allow for neutrino detection through the more conventional inverse beta decay in $^{115}\mathrm{In}$. The concept of quasiparticle trapping, introduced by Booth in 1987, has since become a foundational principle for many cryogenic particle detectors, beginning with this indium detector [51]. The first measurements in neutrinoless double beta decay searches and single beta decay using cryogenic detectors were also recorded.

3. Galactic halo discovery of non-baryonic dark matter: Goodman and Witten proposed using the same cryogenic detector technique for identifying specific dark matter candidates, which was inspired by the publication by Drukier and Stodolsky on detecting solar neutrinos using superconducting granules. A cryogenic particle detector, which has a high sensitivity to weakly ionizing radiation, would be able to detect the nuclear recoil if weakly interacting massive particles (WIMPs) were to occupy our galactic halo: WIMPs would elastically scatter off nuclei. Some of the dark matter experiments employing phonon-mediated cryogenic detectors are the CDMS (The Cryogenic Dark Matter Search), SuperCDMS (Super Cryogenic Dark Matter Search), the CRESST (Cryogenic Rare Event Search using Superconducting Thermometers) collaboration, the EDELWEISS (Expérience pour DEtecter Les WIMPs En Site Souterrain) collaboration, the ORPHEUS collaboration, and few others [52–54].

4. Decay data: The accurate determination and evaluation of nuclear and atomic data is an important task in radiation metrology. This accuracy in measurement hinges on the availability of specific instruments, and the continual enhancement and development of these tools are vital. The first institute to utilize cryogenic detectors in ionizing radiation metrology applications was the French Laboratoire National Henri Becquerel (LNHB-MA). In its first stages, calorimeters were created in collaboration with the Institut d'Astrophysique Spatiale of CNRS combining absorbers like diamond, germanium, or bismuth with NTD Ge thermistors. Subsequent developments led to a shift towards metallic magnetic calorimeters using gold absorbers [55, 56].

The ionizing radiation metrology branch of the U.S. National Metrology Institution NIST operates cryogenic detectors based on TES [57, 58], while the Korean Ionizing Radiation Metrology Institution KRISS as well as the German national metrology institute PTB both uses metallic magnetic calorimeters [59, 60]. LNHB is developing MMCs, in part through collaboration with the Karlsruhe Institute of Technology and Kirchhoff Institut für Physik at the University of Heidelberg. The MMCs are used in diverse measurements including absolute activity measurement, beta spectrometry, fractional electron capture probabilities, as well as X- and gamma-ray spectrometry.

Types of cryogenic detectors Cryogenic detectors are classified into two categories: (near) equilibrium detectors, described as classical calorimeters and non-equilibrium detectors like Kinetic inductance detectors (KIDs), Superconducting tunnel junctions (STJs), and superheated superconducting granules. Near-equilibrium cryogenic detectors are sensitive to thermal phonons, while non-equilibrium ones are more sensitive to the quasi-ballistic, high-energy phonons. The three most common thermometers used for near equilibrium calorimeters are metallic paramagnets, called Metallic Magnetic Calorimeter (MMCs), heavily doped semiconductor thermistors, and superconductors operating at the superconducting to normal transition, known as transition edge sensors (TES). The thermal detectors operating in non-equilibrium mode are generally faster than those in equilibrium mode, as they collect only quasi-ballistic phonons and use the sensors that operate only when the excitation energy is larger than $k_B T$ [61]. In literature, two terms are generally used in reference to cryogenic detectors: calorimeter and bolometer. The main difference between these two is that bolometer is a temperature transducer that measures the flux of particles or radiations. In contrast, the calorimeter measures the energy of single quanta or particles.

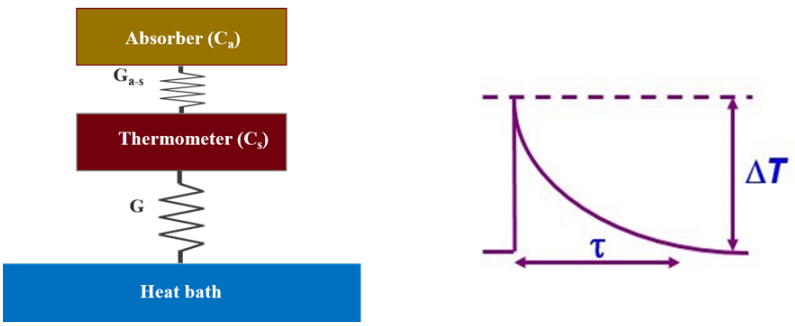

Figure 1.8: Basic concept of a classical cryogenic calorimeter.

The cryogenic calorimeter is comprised of three essential components, as illustrated in the referenced Figure 1.8. The first component is the absorber, whose heat capacity is C_{a}. The incident particles deposit their energy in the absorber, increasing its temperature. This is known as energy thermalization, the conversion of the deposited energy into thermal energy. The second component is a sensitive thermometer (heat capacity C_{s}), which is in tight thermal contact with the absorber, allowing it to detect and measure any increase in the absorber's temperature following the energy

deposition. Lastly is the heat bath (thermal bath) or heat sink. The heat bath is weakly thermally coupled to the absorber-thermometer ensemble to restore their temperature to a base value of the heat bath (T_0) after every event. The thermal link to the heat bath is characterized by its thermal conductivity G and between the absorber-thermometer by $G_{\mathrm{a-s}}$. If the particle deposits an energy E in the absorber, its temperature change is given by $\Delta T = E/C_{\mathrm{tot}}$. Here $C_{\mathrm{tot}} = C_{\mathrm{a}} + C_{\mathrm{s}}$. The thermal time constant of the detector, or pulse decay time $\tau_d = C_{\mathrm{tot}}/G$, is the time taken by the detector to return to its base temperature via the weak thermal link with thermal conductivity G. The terms ΔT and τ_d remain unchanged only if $G_{\mathrm{a-s}} >> G$ and there are no additional heat capacities. In the absorber and/or thermometer, subsystems with specific heat capacities and couplings, such as phonons and electrons are considered for their respective responses. The different types of cryogenic detectors based on their thermometers are described in the following subsections.

In order to increase the signal-to-noise ratio, a large ΔT is a requirement. This can be achieved by choosing a low-specific heat material for the absorber. Different absorber materials like insulators, semiconductors, superconductors, and normal metals can be used. In the case of normal metals as an absorber, the process of energy thermalization is quite simple. Initially, energetic electrons create a series of electron-electron collisions, rapidly reducing the mean electron energy. When the electron energy is low enough, phonon emission becomes the primary energy loss mechanism with most of the total energy transferring to the phonon system. This energy eventually returns to the conduction electrons, dispersing as heat through diffusion in the absorber. In solids at low temperatures, $C_m = C_{\mathrm{e}} + C_{\mathrm{p}}$ decreases, with a temperature dependence of the form $\alpha \mathrm{T}^3 + \gamma \mathrm{T}$, where the T^3 term arises from lattice vibrations (C_p), and the linear term from conduction electrons (C_e). At very low temperatures the electronic heat capacity dominates since it is linear in temperature while the lattice heat capacity is proportional to T^3. Once the heat is uniformly distributed in the absorber volume the temperature rises due to a deposited energy E is given by $\Delta T = E/C_m$.

The little overlap between the valence and conduction bands in semi-metals, on the other hand, makes them resemble metals with very low conduction electron densities. Compared to ordinary metals, this results in a lower electronic specific heat, but it still makes a considerable contribution to the total specific heat. In addition, the lattice-specific heat must be taken into account because it is no longer insignificant in contrast to the electronic specific heat.

1.4.3.1 . Semiconductor thermistors

A thermistor is a device characterized by a resistance that changes with temperature. In semiconductors, the thermal ionization is reduced at low temperatures. For materials like silicon and germanium, room temperature conditions lead to near-complete ionization of shallow impurities with binding energies in the tens of millielectronvolts range. As the temperature decreases, the ionized fraction diminishes rapidly, restricting its usage as low-temperature thermometers. To facilitate their operation as low-temperature thermometers, semiconductors are heavily doped in a process involving variable range hopping conduction. This method requires charge carriers tunneling between randomly dispersed, strongly doped locations in the semiconductor, allowing thermistors to function at low temperatures. In the crystalline lattice, the doping atoms replace the host crystal's atoms. The tunneling process, contingent on the dopant type and concentration, needs additional phonon energy and typically occurs at extremely low temperatures where phonons are sparse. Tunneling spans

various lengths and is only viable between sites with energy levels matching the available phonon energy [62].

Early x-ray calorimeters utilized doped semiconductor thermistors fabricated from neutron transmutation doped (NTD) germanium and ion-implanted silicon. The benefit of silicon is its amenability to monolithic array fabrication through established micro-machining methods. Ion implantation, a standard procedure in the semiconductor industry, permits penetration depths up to 1 µm, creating a Gaussian density distribution. Specific implant layering or diffusion post-implantation can result in a uniform distribution. Germanium can be doped via neutron irradiation in nuclear reactors, ensuring homogeneous doping even in extensive batches. This material, however, requires post-processing to form connections. Unlike germanium, silicon thermistors allow photolithography to define implant regions and contacts across an entire wafer, though NTD Ge thermometers offer greater size diversity. The chief advantages of NTD germanium include repeatability and uniform doping density [63].

The thermal pulse arising from an energy release in the absorber translates to a resistance change in the thermistor, proportional to the energy released. The thermistor is included in a bias circuit, converting the resistance fluctuation into a voltage signal. Determining the optimal bias current for the thermistor is crucial for maximizing detector performance. This optimization is often assessed by examining the current-voltage (I-V) curve, allowing the identification of the optimal operating point. They are sensitive mainly to thermal phonons since athermal phonons have a low probability of interacting in the small volume of the thermistor are glued. The metal-insulator transition (MIT) zone, where the resistivity demonstrates a strong temperature dependence, is where the semiconductor enters when the doping concentration reaches a critical point. The thermistor resistance dependency on temperature is defined at sub-Kelvin temperature by

$$R(T) = R_0 \left(\frac{T_0}{T} \right)^{\frac{1}{4}}$$

In the above equation, R_0 and T_0 depends on the crystal's doping concentration and geometry. These high-impedance devices are read out by comparatively traditional, low-noise preamplifiers that employ a JFET (junction field-effect transistor) at the entrance stage. To enhance the noise performance, the JFET is frequently cooled to 130 K [64].

1.4.3.2 . Transition edge sensors (TES)

The Transition-Edge Sensor (TES), also known as a superconducting phase-transition thermometer (SPT), is a type of thermal sensor that detects energy deposition through changes in the resistance of a superconducting film. This film is biased in the specific temperature region where the superconducting material is transitioning to its normal state (see Figure 1.9). In this narrow temperature range, the electrical resistance of the material shifts between its normal value and zero [65]. A TES thermometer can be used in a bolometer (for power measurement) or a calorimeter (the energy of individual particles). In 1941, physicist D.H. Andrews conducted an experiment in which he applied an electrical current to a thin wire made of tantalum, while it was in its superconducting transition region at a temperature of 3.2K. He then detected the alterations in resistance in response to an incident infrared signal. This constituted the initial demonstration of a Transition Edge Sensor (TES) bolometer [66]. Later, in 1949, Andrews continued his research by applying a current to a strip of

niobium nitride within its superconducting phase transition at 15K. He subsequently measured the voltage pulses produced when the strip was exposed to alpha particle radiation. This marked the first documented Transition Edge Sensor (TES) calorimeter demonstration [67]. In the initial years of their development, there was a limitation in matching their noise to FET amplifiers. They were usually read out using a cross-correlation circuit to cancel noise ac biased with a step-up transformer or built-in long meander lines with high normal resistance to noise match. W. Seidel [68] first resolved this issue through the employment of superconducting quantum interference device (SQUID) current amplifiers, which can be readily impedance-matched to low-resistance TES detectors [65].

The operation of Transition Edge Sensor (TES) detectors within the extremely constrained superconducting phase transition has been one of the challenges in their effective usage. When they are current-biased, Joule heating of the TES by the current can lead to thermal runaway, and small fluctuations in bath temperature significantly degrade performance. When the TES is instead voltage-biased and read out with a current amplifier, the devices can easily be stably biased and they self-regulate in temperature within the transition with much less sensitivity to fluctuations in the bath temperature.

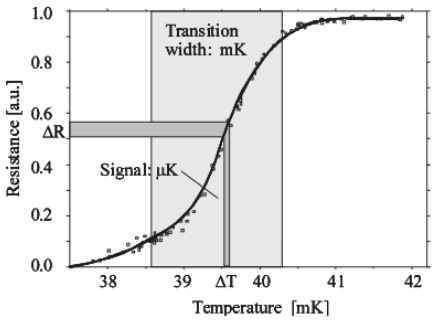

Figure 1.9: Principle of Transition Edge sensors.

The Figure 1.10 shows the schematic of a single TES read out with a SQUID amplifier. In this circuit, the stray inductance is kept small by mounting the first-stage SQUID chip at the base temperature of the cryostat, adjacent to a chip with the TES. The shunt resistor (R_{shunt}) is fabricated on the TES chip, and the TES chip is connected to the first-stage SQUID chip by wire bonds. The first-stage SQUID is voltage-biased in series with the input coil of a series-array-SQUID second-stage amplifier. The series-array SQUID amplifies the signal sufficiently to couple to room-temperature electronics. A temperature signal in a TES is transduced into an electrical current signal by the change in the resistance of the TES. In turn, the electrical current signal in the TES is feedback into a temperature signal by Joule power dissipation in the TES. This electrothermal feedback (ETF) process is analogous to electrical feedback in a transistor circuit. Feedback can be positive or negative. An amplifier is prone to instability while operating with positive feedback and the open-loop gain is one intrinsic parameter that tends to vary significantly in high-gain transistor amplifiers. Thus, negative feedback is employed and the bias circuit's extrinsic parameters—rather than the amplifier—determine the (closed-loop) gain, resulting in more consistent and repeatable circuit performance. Negative feedback also linearizes detector re-

sponse and broadens the dynamic range. A voltage-biased TES has the particularly interesting feature that it automatically maintains its temperature within the phase transition region based on the input signal power and bias voltage. This is a crucial aspect, especially in applications that require an array of these sensors. If multiple pixels in an array have superconducting phase transition regions that do not overlap in temperature, it is impossible to bias them all at the same temperature. However, if they are voltage biased, and the bath temperature is much lower than the transition temperature, the Joule power dissipation in each pixel causes it to self-heat to within its respective phase transition. When the bath temperature is well below the transition temperature, the TES performance is also less sensitive to fluctuations in the bath temperature, easing the requirements for temperature stability.

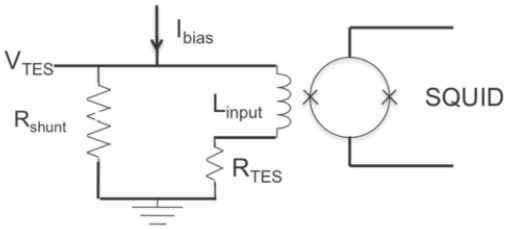

Figure 1.10: Schematic of a single TES read out with a SQUID amplifier. The TES is maintained at a constant voltage bias via a shunt resistor with $R_{\mathrm{shunt}} << R_{\mathrm{TES}}$ [68].

TES detectors differ from other thermal detectors mainly in their use of a superconducting thermometer. The type of superconducting material, specifically its transition temperature (T_c), greatly influences the detector's performance by affecting factors like thermal conductance, heat capacity, and thermal noise. The choice of T_c also has implications in design, often restricted by refrigeration considerations. Most TES transition temperatures are near 400 mK (for $^3\mathrm{He}$ cryostat operation) or 100 mK (for adiabatic-demagnetization and dilution refrigerators). To achieve these ranges, three techniques are usually employed: elemental superconductors, proximity multilayers, and magnetically doped superconductors, with proximity multilayers being the most common. In proximity multilayers, a composite superconductor is constructed using layers of both a superconductor and a normal metal. If these layers are thinner than the superconducting coherence length and the interface is clean, the composite's critical temperature (T_c) is lower than that of the pure superconducting film. This phenomenon is known as the proximity effect.

TES detectors are employed in various applications. In radiation metrology, TES is used at NIST for developing quantum metrology for monitoring radiation interactions at the atomic scale and to maximize achievable precision on SI units for ionizing radiation. TES are also used in single photon detectors due to their high efficiency and low noise [69]. In the case of X-ray metrology, for the requirement of absolute energy measurements of the X-ray energies below 10 keV, TES has shown promising results. TES are used at LANL in alpha spectrometry for nuclear forensics and environmental monitoring, requiring the isotopic analysis of trace radioactive samples [70]. They are also used in astronomical telescopes to measure faint signals in microwave, infrared, and X-ray bands [71]. One example is the South Pole Telescope, which uses TES bolometers to measure the Cosmic Microwave Background [72]. They are also used in experiments searching for dark matter particles, where their ability to detect very small energy deposits is crucial [52–54].

1.4.3.3 . Metallic magnetic calorimeter (MMCs)

MMCs measure the energy of the deposited individual particle/photon as the temperature rise of the - mostly metallic - absorber. This temperature rise leads to the change in magnetization of a paramagnetic sensor in strong thermal contact with the absorber, the sensor being placed in a weak magnetic field. To read the change in magnetization, a DC SQUID magnetometer is used (see Figure 1.11 for reference). The magnetization of the thermometer may be coupled to the SQUID primarily in two different ways. The thermometer can be placed into the SQUID sensing loop, or the signal can be coupled via a superconducting flux transformer. A superconducting flux transformer consists of a pickup coil, which reads out the signal of a PM sensor, and the input coil, which couples the signal to the readout SQUID. This forms a closed superconducting circuit. The maximum sensitivity is achieved when the heat capacity of the absorber and paramagnetic sensor matches [73]. The working principle of MMCs can be written as

$$\Delta E \rightarrow \Delta T \rightarrow \Delta M \rightarrow \Delta \phi \rightarrow \Delta V$$

- ΔE= Energy deposited by the particle in the absorber
- ΔT = Change in temperature of the absorber
- ΔM = Change in magnetization of the paramagnetic sensor
- $\Delta \phi - > \Delta V$ corresponds to the SQUID voltage response to the magnetic flux coupled to it via the flux transformer

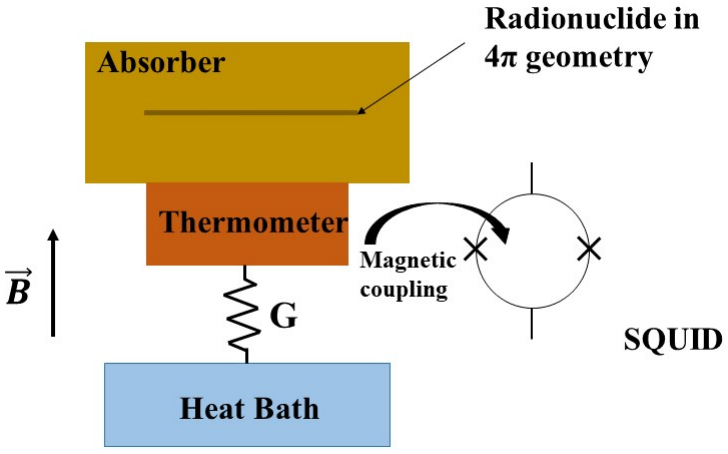

Figure 1.11: Basic idea of a an MMC, here configured for 4π measurement with the radionuclide embedded in its absorber.

The immersing the magnetic ions in a dielectric host material yields the greatest variation in magnetization per deposition of energy. Nevertheless, it was soon discovered that any practically usable detector is incompatible with the large time constant corresponding to the very weak thermal coupling between the phonons of the host material and the spins of the paramagnetic ions at extremely

low temperatures. By embedding the paramagnetic ions in a metallic host material, this issue was solved, as it was observed that even at mK temperatures, time constants of the order of a microsecond were attained due to the highly efficient thermal coupling between the spins and conduction electrons. The drawback of utilizing metallic paramagnets is that the electrons increase the interaction between the localized magnetic moments and raise the sensor's heat capacity. The enhanced spin-spin interaction can be reduced by using rare earth ions as magnetic impurities, which have partially filled 4f-shells. Erbium, one of the rare earth ions, seems to be a particularly sensible choice due to its low de Gennes factor, which is also advantageous regarding the spin-spin interaction. For a given absorber heat capacity, the combination of metallic absorbers with metallic magnetic thermometers provides the benefit of a very quick signal rise time. Conduction electrons can carry heat into the thermometer without significant thermal resistance if the contact between the absorber and thermometer is metallic, that is, if there is no oxide or other insulating layer present between sensor and absorber. Even at low temperatures, the thermometer's electron-spin coupling is extremely quick; thermal equilibrium between conduction electrons and spins is often achieved in less than a microsecond. Thermal equilibrium is reached over the whole calorimeter in a matter of microseconds, even with absorber heat capacities of several nJ/K [61, 73, 74]. More details about the MMC detectors are given in chapter 2.

1.4.3.4 . Kinetic inductance detectors (KIDs)

A kinetic inductance detector (KID) is an integrated superconducting resonator. When its superconducting material absorbs a photon, the circuit's resonance frequency changes. Should this change in frequency be measurable, determining the energy associated with a single photon event becomes feasible. The term "kinetic inductance" refers to the inductance of a material governed by the inertia of charge carriers, which are the Cooper pairs and quasiparticle excitations in the context of superconductors. Below the critical temperature T_c, the kinetic inductance of Cooper pairs plays a more prominent role in the surface impedance compared to the quasiparticles. The relationship between kinetic inductance and temperature may be employed to gauge temperature fluctuations in superconductor thin films. McDonald initially suggested this phenomenon for utilization in cryogenic detectors in 1987. Subsequent work in 2002 by Zmuidzinas et al. and Sergeev et al. introduced a detector incorporating a SQUID to monitor variations in bias current within a small superconducting circuit. Furthermore, J. Zmuidzinas and collaborators proposed using a microwave resonator composed of a superconducting thin film to scrutinize alterations in resonance circuit attributes and perceive changes in the superconducting film's surface impedance. This particular detector was named the Microwave Kinetic Inductance Detector (MKID) [76].

When the radiation strikes a superconducting thin film, Cooper pairs are broken, and as a result, quasi-particles are generated. The density of the Cooper pairs is inversely proportional to the kinetic inductance of the superconducting thin film. The absorption of radiation leads to a rise of kinetic inductance. A microwave resonator measures the resonant frequency changes due to radiation absorption. KIDs are helpful in applications requiring large detector arrays, as a single microwave tone can treat each KID, and many detectors can be monitored using a single broadband microwave channel. This method is known as frequency-division multiplexing. The KIDs have various applications from X-rays astronomy to the far-infrared region, as they are very fast with low noise and relatively

simple to build and implement in large array detectors [77].

The two major realizations of superconducting kinetic inductance detectors are the quarter wavelength transmission line resonator and the lumped element resonator. A quarter wavelength transmission line resonator uses a microwave resonator whose one end is grounded, and the other is capacitively coupled to the transmission line. Changing the length of the transmission line allows for customization of the resonance frequency. To have the maximum sensitivity, the incident radiation is coupled to the shorter end of the transmission line where the voltage is the lowest, and the current is the highest. Instead of using a transmission line for the resonator, the lumped element resonator type detector known as LEKID, the lumped components, inter-digitated fingers for capacitance, and a meander for inductance is used. The resonant frequency is modified by changing the inter-digitated capacitors capacitance while keeping the overall detection area equal. The simplified fabrication of the LEKIDs is its advantage over the quarter wavelength transmission line resonator type. For the whole device, just one material layer is required, eliminating additional processes and interfaces. Its disadvantage is its weak stopping power for highly energetic photons, as the increase in the thickness of the film leads to an increase in detector volume and hence decrease in sensitivity [78].

1.4.3.5 . Superconducting tunnel junctions cryogenic detectors (STJs-CDs)

A Superconducting Tunnel Junction (STJ) comprises two superconducting layers that operate as radiation absorbers and are separated by a thin insulating layer. Hf, Nb, Al, or Ta thin films can be superconducting layers. Below the critical temperature T_c, electrons in a superconductor are organized in Cooper pairs, with a binding energy of 2Δ with Δ denoting the superconductor's energy gap, which is inversely proportional to T_c. The absorption of a photon with energy E in a superconductor is followed by a sequence of fast events involving both electrons and phonons. By breaking Cooper pairs, photon energy is transformed into quasi-particles having densities larger than the thermal density. The time scale of this conversion process for typical transition metals covers from nanoseconds (niobium) to microseconds (hafnium) [79–81]. A schematic representation of a superconducting tunnel junction is shown in Figure 1.12.

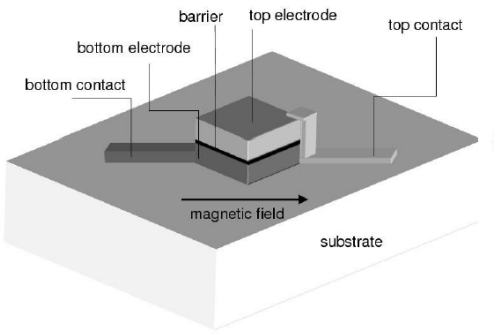

Figure 1.12: Schematic representation of a superconducting tunnel junction [79].

At finite temperature, a percentage of the Cooper pairs are broken into excited states known as quasi-particles (QP) by continuous pair breaking by thermal phonons with energy greater than 2Δ and

recombination of QPs with phonon emission. These rates are material dependent and tend to slow down for lower-T_c superconductors. QP-associated charge carriers can tunnel quantum mechanically over the insulating barrier. Four tunnel processes are available and are shown in Figure 1.13.

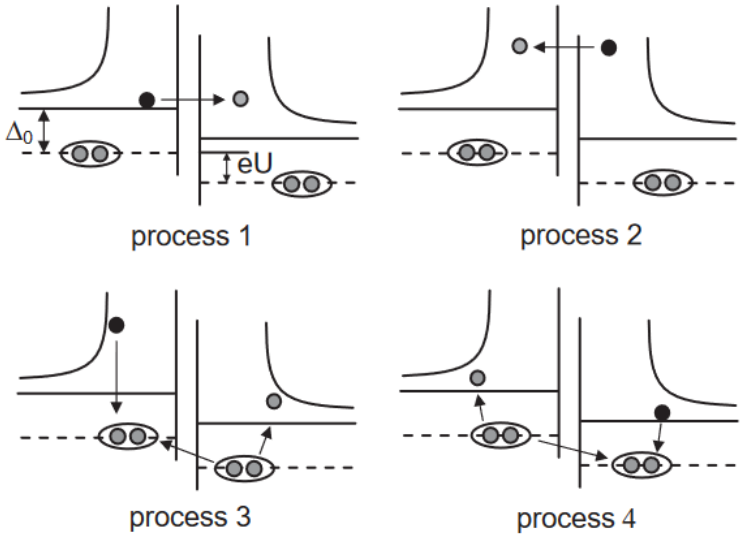

Figure 1.13: Schematic representation of the two possible tunnel processes in an STJ for the case of a symmetric STJ under a bias voltage $\mathrm{U_b}$ [81].

Processes 1 and 3 involve the direct transmission of a quasiparticle from left to right and vice versa and correspond to the transfer of an electron in the same way. Processes 2 and 4 involve the additional annihilation of a Cooper pair in one film and creation in the other film. In process 2, a QP is effectively moved from right to left, while an electron continues to go from left to right, as in process 1. When the bias voltage is sufficiently high, the occupancy of the higher energy levels is low enough that only processes 1 and 2 contribute considerably to the tunnel current [80, 81].

The excess quasiparticle population generated by photo-absorption in one of the electrodes of a voltage-biased STJ will be detected as a tunnel-current pulse with a magnitude proportional to the energy of the incoming photon. Absorptions in either electrode of the STJ will produce the same polarity current pulse, and quasiparticles transferred to the other electrode by one of the two processes 1 or 2 described above can continue to contribute to the signal by 'back tunneling' as long as they are present in the electrode volume. The STJ is operated at T, low enough to avoid many thermally excited quasiparticles. The loss rate is contributed by processes like QP diffusion out of the electrode volume or trapping and recombination in defects at surfaces, edges, or bulk impurities. Adding layers of a lower-gap material on either side of the barrier can improve the rate. This keeps quasiparticles confined close to the barrier and away from potential loss locations like surfaces. The plus point of STJs is that they are extremely fast compared to MMCs and TES; their drawback is a somewhat lower energy resolution. The thermal processes on which calorimeters rely are often slower than quasiparticle relaxation. This implies that STJs can be used with higher photon-counting rates.

1.5 . MMCs for spectrometery in radiation metrology

Metallic magnetic calorimeters are preferred for the measurements concerning the decay data. MMCs offer significant advantages, including exceptional linearity across a broad energy spectrum and a consistently high-energy resolution that is almost independent of energy, a characteristic attributed to their nature as near-equilibrium detectors. By optimizing the absorber's heat capacity, a fast response in terms of signal rise time can be achieved. Another advantage of MMCs is their potential to approach a near-perfect detection efficiency of 100% at low energy. This is achieved through their high stopping power and a very low energy threshold. In terms of the fractional electron capture probability measurements, MMCs in the decay energy spectroscopy (DES) technique measure the whole of the decay energy except that of neutrino. This technique allows us to have completely experimental values that do not rely on theoretical calculations, which is very challenging with any conventional detector and not possible for higher than L shell captures [82]. These measured values can then be used to verify the theoretical calculations. The measurement of ratios of the electron capture probabilities $P_{\mathrm{K}}, P_{\mathrm{L}}$ and P_{M} of $^{55}\mathrm{Fe}$ gave consistent results with both theoretical as well as literature values, and the energy threshold was low enough to allow for clear separation of the M captures (~ 80 eV) from noise [83].

The Beta spectrum is required in the primary activity measurement technique: Liquid scintillation counting (LSC). The LSC needs precise knowledge of the beta spectrum to model light emission, particularly on the low-energy spectrum where detection efficiency significantly decreases. The activity standard's uncertainty budget must account for knowledge about this parameter. MMCs exhibiting excellent energy linearity and low energy threshold work as the best detection methods for low to medium energy beta spectrometry [37, 84]. The recent measurement of the beta decay of $^{151}\mathrm{Sm}$, yielded a beta spectrum with a high-energy resolution of about 70 eV (FWHM) at 22 keV and a low energy threshold below 400 eV. The spectrum showed unexpectedly elevated beta emission probabilities at very low energy, which were not reproduced in theoretical studies. The spectrum was compared to advanced theoretical modeling, which accounts for atomic exchange effects, precise radiative corrections, and realistic nuclear structure—critical for first forbidden non-unique transitions [85].

Our MMC group at LNHB-MA, CEA Paris-Scalay does perform the measurements concerning electron capture probability ratios, beta spectrum shape, absolute activity measurement, and X-ray, gamma, and electron spectroscopy spectrometry. In the case of measuring photon emission intensities in complex spectra, the X- or gamma-ray line separation using semiconductor detectors is not possible due to their insufficient energy resolution [86]. A high-resolution spectrometer, based on MMCs, has been developed to meet this need. The L X-ray spectra from $^{241}\mathrm{Am}$ and $^{210}\mathrm{Pb}$ decays measured with this spectrometer show a full-width half-maximum (FWHM) energy resolution of 26 eV and a constant detection efficiency between 5 and 26 keV, allowing for the determination of about 30 relative L X-ray intensities for $^{241}\mathrm{Am}$ and $^{210}\mathrm{Pb}$ [87].

2 - Metallic Magnetic Calorimeters

2.1 . Physical principle

Metallic magnetic calorimeters (MMCs) are highly sensitive energy dispersive low-temperature particle detectors. MMCs properties differ significantly from other cryogenic particle detection systems in two significant ways. To begin with, an MMC is a well-known thermodynamic device comprising an absorber, a paramagnetic metallic sensor, and a heat bath. The working principle of MMCs is based on the measurement of the temperature change (ΔT) that occurs when the energy (E) of an individual photon or particle is deposited in the detector. When a photon or particle is absorbed by the detector, it creates a small amount of heat due to the transfer of its energy to the absorber material. This heat causes a small temperature rise in the detector, which is measured using the paramagnetic temperature sensors. The temperature rise causes a change in the magnetic susceptibility of the paramagnetic material, which leads to a change in the sensor magnetization in the presence of a magnetic field. This change in the magnetic flux is read out using a SQUID magnetometer. A superconducting pickup coil couples a magnetic field into the SQUID's input terminals. The calorimeter's response to energy absorption can be precisely estimated if the thermodynamic parameters of the sensor and absorber are understood. This results in a well-defined relationship between the size of the magnetic sensor, the pickup coil, the input coil of the SQUID, and the measured signal. The signal of MMC is proportionate to the change in flux in a SQUID circuit and is based on the equilibrium thermodynamic characteristics of the sensor material rather than a transport attribute [73, 74, 94].

The absorber and paramagnetic sensor (thermometer), as shown in Figure 2.1 are in strong thermal contact with each other and this absorber thermometer ensemble is connected by a weak thermal link of conductivity G to a heat bath maintained at a constant temperature T_0. The absorber-thermometer ensemble is characterized by their respective heat capacities C_a and $C_s$and total heat capacity $C = C_a + C_s$. After each energy deposition, the detector returns to its equilibrium temperature T_0 with a time constant $\tau_d = C/G$. The temperature rise of the absorber, according to the thermodynamics, is described as

$$\Delta T = \frac{E}{C} \tag{2.1}$$

This temperature rise leads to a change in magnetization of the paramagnetic sensor as

$$\Delta M \simeq \frac{\partial M}{\partial T} \Delta T \tag{2.2}$$

This change in magnetization is detected by the pickup coil as a change of magnetic flux and we get information on the absorbed energy in the absorber as :

$$\Delta \phi \propto \frac{\partial M}{\partial T} \frac{E}{C} \tag{2.3}$$

The sensitivity and the thermalization time are important for applications in particle detection. Since the magnetic characteristics of many materials are substantially dependent on temperature.

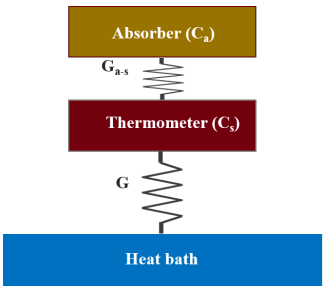

Figure 2.1: Basic representation of working principle of MMCs.

The magnetization measurements are widely applied for thermometry at low temperatures. It is crucial to identify the proper material to be used as a thermal sensor because it must combine a strong temperature dependency of magnetization with a low heat capacity C and a fast response. Magnetic thermometers are the most sensitive ones in use.

In 1986, W. Seidel's diploma thesis at the Technical University of Munich first introduced the concept of low-temperature magnetic calorimetry for particle detection [88]. At the Walther-Meissner-Institute in Munich, a development project to use para magnetism for particle detection was subsequently launched. Umlauf and colleagues showed the effectiveness of measuring small energy inputs to an absorber utilizing the magnetization of 4f ions in a dielectric host material. They focused on detectors with a paramagnetic ion system as the sensor inside a dielectric host. The candidate was cerium magnesium nitrate (CMN) due to its high sensitivity at low-temperature regions. Even in the concentrated paramagnetic salt, the bipolar interactions were very weak due to the unique crystal structure of CMN and the high anisotropic g-factor of the cerium ion in this crystal [89]. Only at very low temperatures does magnetic ordering occur, and although it has larger spin-spin interactions, there was relatively little effect on heat capacity and sensitivity. Due to its intrinsically slow response time, magnetic calorimeters based on dielectric host materials were hardly suitable for any practical applications in particle detection. This main issue results from the weak coupling of phonons to magnetic moments at low temperatures, restricting the use of spin-para magnetism for particle detection [90].

It was proposed in 1993 [91] that utilizing magnetic ions in metallic or semi-metallic host materials may solve this issue. In noble metals as hosts, the characteristics of isolated ions of the d and f transition series elements have been examined. The energy deposited in the sensor is shared between the conduction electrons and the magnetic moments in the sensor material, giving rise to the signal. The fraction of a particle's energy that enters the spin system during thermal equilibrium is proportional to the ratio of the spin heat capacity to the total heat capacity (C_{spin}/C_{total}). To attain the maximum sensitivity, the heat capacity of the spins must be roughly equal to that of the heat capacity of the conduction electrons of the sensor and the absorber. Relaxation time in metals is many orders of magnitude shorter than in insulating hosts due to the strong interaction of the magnetic moments with the conduction electrons. The localized magnetic moments of the ions interact with the conduction electrons in such a way that their thermal relaxation time is 10^{-9} sec or less above 1 K. The coupling in the millikelvin zone continues to be quicker than 10^{-6} sec. The response time (τ) can be expressed by the Korringa relation ($\tau = \kappa/T$), κ is the Korringa constant [91]. The consequence one has to ac-

cept for the benefit of the quicker response is that the presence of conduction electrons enhances the sensor's heat capacity and stimulates stronger interactions between magnetic moments. These are undesirable as they reduce the sensor sensitivity.

The usable concentration of spins has a limit, though, due to magnetic interactions. Using a metallic host material like gold has two negative impacts. At low temperatures, the conduction electrons have a significant heat capacity. Moreover, a spin-spin indirect exchange interaction known as the Ruderman-Kittel-Kasuya-Yosida (RKKY) also results from the coupling of spins with conduction electrons. This indirect exchange interaction reduces the temperature dependence of the magnetization. It adds extra heat capacity to the system, and both are detrimental to the performance of magnetic calorimeters. Technical considerations like the convenience of fabrication, stability, etc., and the requirement for a modest RKKY exchange interaction influence the choice of host metal and paramagnetic ion. Due to their weaker interactions with the conduction electrons, ions in the 4f series perform better in this regard than those in the 3d and 4d transition series. Due to its significantly smaller radius than the filled 5s and 5p shells, the 4f shell is better protected from the crystal field. It exhibits less interaction with conduction electrons than the 3d electrons of transition metals. For the same reason, it is desirable to use rare earth elements that have a limited projection of the intrinsic spin of the ion onto the effective spin of the crystal field ground state. One of the most promising choices in this regard is Er^{3+} ion [73, 74, 93]. More details about the sensor are discussed in the subsection 2.1.2

2.1.1 . Absorber material

In this thesis, the radionuclide to be measured is embedded in the metallic particle absorber to get a 4π geometry. This measurement technique is also called Decay energy spectroscopy [95]. Gold is commonly used as an absorber in metallic magnetic calorimeters (MMCs) [37, 82, 84, 95–97], and the advantages of using a gold absorber are listed below.

- High thermal conductivity: Gold has a high thermal conductivity at mK temperatures, which means it can quickly and efficiently transfer heat within its volume and toward the sensor.
- Ionizing radiation has the ability to excite meta-stable states in some materials, such as trapped electron-hole pairs, on a time scale similar to or longer than the detector time constants. This is not applicable to normal metals.
- High density: It has a very high stopping power due to its high atomic number and density.
- Chemically inert: In the 4π geometry, the radionuclide is embedded in the absorber. The radioactive source solutions are often chemically aggressive and can react with the absorber material. With gold being chemically inert, there is no risk of a chemical reaction between the absorber and the source.
- Ease of fabrication because gold, as a normal metal, is a soft and ductile metal, which leads to the ease in fabrication of 4π geometry absorbers if they cannot be micro-fabricated.

At the mK temperature, gold has a higher specific heat than superconductors like tin and lead or semi-metals like bismuth. Nevertheless, using a gold absorber in MMCs provides excellent performance characteristics with high energy resolution and intrinsic detection efficiency, making it an

ideal material for its application in radiation metrology. However, energy escape processes can distort beta spectra. Bremsstrahlung photons may escape from an absorber if a high initial energy beta electron is stopped. This phenomenon may lead to detecting high-energy decay events at low-energy decay. The atomic mass of the material in which the electron decelerates and the electron energy affect the likelihood of bremsstrahlung generation. Hence, a low atomic mass absorber material can lower the number of bremsstrahlung photons produced. However, there are two drawbacks to using a low atomic mass absorber material.

- The lower photon absorption probability of a low atomic mass absorber material.
- The advantages of the lower bremsstrahlung production are partially offset by the need for a larger absorber with a higher heat capacity, which reduces the energy resolution and raises the detector energy threshold.

A solution could be the use of a bi-layer absorber [97,149]. A high atomic mass outer layer reduces the overall absorber thickness necessary for stopping the electrons while increasing the probability of photon absorption. In contrast, an interior layer with low atomic mass reduces bremsstrahlung production when the electrons still have high energies.

Insulators as an absorber material have also been studied. The interaction of ionizing radiation with the insulator absorber produces energetic electrons. These energetic electrons produce high-energy optical phonons, which decay within nanoseconds to acoustic phonons of roughly half the material's Debye frequency. Acoustic phonons spontaneously decay into two phonons, and if the insulator has more than one isotope of any element, they scatter elastically (isotope scattering). The decay rate is given as $\tau_d \sim 0.1\gamma\omega_D \left(\frac{\omega}{\omega_D}\right)^5$, ω is the phonon frequency, ω_D the Debye frequency and γ is a material specific constants. The factor 0.1 comes from energy conservation, and momentum conservation states that only longitudinal acoustic phonons can decay, as transverse acoustic phonons occupy the lowest branch of the phonon dispersion relation. The decay rate differs considerably with frequency. Thus, the first few phonon generations decay quite fast, but the phonon frequency drops after a few tens of microseconds. At this point, the phonon temperature is still several Kelvins above thermal equilibrium, and the thermalization of the phonons in the bulk solid is extremely slow. Phonons can propagate diffusively at the highest energies, ballistically at somewhat lower energies, and eventually thermalize. Thermalization depends on processes such as impurities, isotopes present in the material, grain boundaries, or inelastic surface scattering due to a shortage of phonons available for phonon-phonon interactions in the temperature range of cryogenic detectors, and hence proceeds very slowly, taking time in the scale of ms or s [98].

Other materials like superconducting rhenium as an absorber for MMCs have also been studied. In the article [99] discussing superconducting rhenium as an absorber, the authors observed that the heat capacity of the rhenium absorber is several orders of magnitude greater than that of rhenium in the superconducting state. This value was proposed to be due to normal metal regions, making up about 1% of the absorber volume. In the studied temperature range, it was discovered that, regardless of temperature, around one-third of the deposited energy was initially stored in athermal systems. The decay time of the observed pulses was roughly an order of magnitude longer than that of similar MMCs without a superconducting absorber. It may be related to the recombination of quasi-particles

in the absorber due to the presence of the normal metal region. In the reference [100], the authors study the response of a magnetic calorimeter with an X-ray absorber made of sapphire crystal ($2 \times 1 \times 0.5\,\mathrm{cm}^3$) as a function of temperature. A gold film of $2 \times 2\,\mathrm{mm}^2$ having 4 spokes (30 µm wide and 115 µm long) at its center was deposited on the surface of the crystal to thermally connect it to the magnetic sensor of the MMC to have faster decay time. Two further, considerably smaller Au films were deposited on the sapphire crystal. One acted as a heater (superconducting leads with low thermal conductivity), while the other offered thermal contact to the heat bath via an Au wire. An Am-241 source provided 60 keV gamma rays to the sample. It was observed that the area and thickness of the film affect the percentage of the X-energy rays caught by the gold film without first being down-converted to thermal phonons in the sapphire. The electron/phonon interaction in the gold films determines the energy transmission rate between the sapphire's thermal phonons and the film's electrons. Moreover, a higher heat capacity was seen in sapphire, which is attributed to the tunneling mechanisms. The diversity of materials that can be used as absorbers is also an advantage of cryogenic detectors.

2.1.2 . Paramagnetic sensor

The term "metallic" in metallic magnetic calorimeters refers to the paramagnetic sensor's metallic host (Ag or Au), which is required for fast response to particle detection. Low concentration (on the order of 0.1%, typically ~ 300 ppm) of erbium combined with gold/silver to generate a diluted alloy. In typical fcc lattice locations, erbium in the 3^+ state replaces Ag or Au, donating three of its electrons to the conduction band. Dilute paramagnetic alloys with an Au or Ag host that have been doped with a few hundred ppm erbium are the sensor materials that were utilized for MMCs in this thesis. The electron configuration of Er^{3+} is given by $[Kr]\,4d^{10}4f^{11}5s^25p^6$. The electrons of the partly filled 4f shell, which is located deep inside the 5s and 5p shell as shown in Figure 2.2, give rise to the paramagnetic properties [101–103].

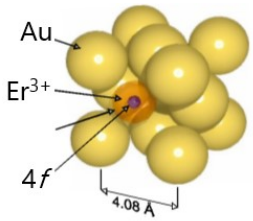

Figure 2.2: Au:Er FCC lattice structure.

At temperatures above 100 K, the influence of the crystal field effect is minimal due to the position of the 4f shell deep inside the ion. Hund's rules can be used to calculate the magnetic moment $\mu = g\mu_B J$, where $\mu_B$is the Bohr magneton. The Lande's g factor is calculated as:

$$g = 1 + \frac{J(J+1) + S(S+1) - L(L+1)}{2J(J+1))}, \tag{2.4}$$

The ground state of the Er^{3+} ion has a total angular momentum of $J = 15/2$, orbital angular momentum of $L = 6$, and a spin angular momentum of $S = 3/2$ giving Lande's g-factor $g = 6/5$.

At temperatures below 100 K, the crystal field effect can no longer be ignored. The sixteen-fold degeneracy of the Er^{3+} ground state is lifted by the fcc-symmetric crystal field, which divides it into a number of multiplets, including three $\Gamma 8$ quartets along with a $\Gamma 6$ and a $\Gamma 7$ doublet. A $\Gamma 7$ Kramers doublet is the lowest multiplet. The behavior of erbium in gold can be roughly described as a two-level system at suitably low temperatures and low magnetic fields. This system has the effective spin, $\widetilde{S} = 1/2$ and an isotropic g factor of $\widetilde{g} = 34/5$. These values were confirmed by ESR experiments in the reference [92]. To ensure that the spin-spin interactions do not significantly reduce the temperature dependence of the magnetization, the interactions between spins must be weak. In order to do this, the diluted concentration of paramagnetic ions are randomly dispersed across a host material (Au or Ag) rather than a concentrated spin system. The temperature, the concentration of Er ions, and the external magnetic field also affect how the magnetization changes. Due to the low de Gennes factor of Er^{3+} and the quick electron-spin relaxation time allowing for sub-100 ns signal rise times, diluted alloys of erbium and noble metals are well suited to be such a sensor material.

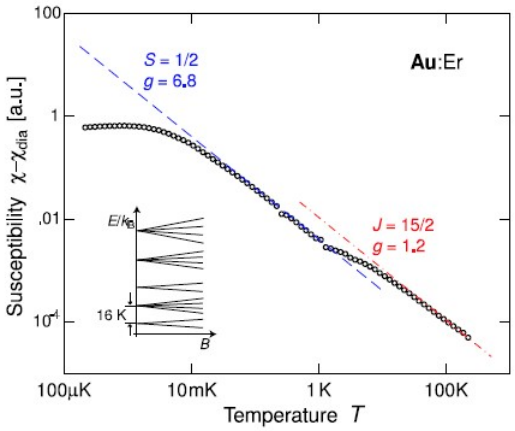

Figure 2.3: Paramagnetic contribution to the magnetic susceptibility of Au containing 600 ppm Er as a function of temperature [73, 74].

In Figure 2.3, the paramagnetic contribution to the magnetic susceptibility of Au containing 600 ppm Er as a function of temperature in the temperature range between 100 mK and 300 K is plotted. There are four temperature zones. The plot follows the Curie law at T > 100 K. A deviation can be observed in the region 1.5 - 100 K due to the depopulation of the multiplets with higher energies. Below 1.5 K, the plot again follows the Curie law but with a smaller Curie constant in accordance with the ground state doublet's effective spin $\widetilde{S} = 1/2$ and $\widetilde{g} = 34/5$. Below $T = 50\ mK$ the magnetic susceptibility becomes substantially less temperature dependent due to the result of the exchange interaction between the magnetic moments. Ultimately, a maximum in magnetic susceptibility of 600 ppm sample is seen at a temperature of roughly 0.9 mK, which is the result of a transition to a spin glass state [73, 74].

In the starting days of MMCs, the sensor was made from Er^{3+}ions embedded in gold metal being the host material. In recent years, gold has been replaced by silver as a host material. The comparison between Au:Er and Ag:Er is explained in the following. For Au:Er, the electron shell energy gap $\boldsymbol{\Delta} E$ is 16 K, while for Ag:Er, it is 25 K. Thus, both alloys operate as a two-level system with an effective spin

of $S = 1/2$ and an isotropic g-factor of 34/5 at the normal operating temperatures (mK) of MMCs. While the dipole-dipole interaction strength is the same for both alloys, the RKKY interaction strength varies. RKKY interactions are contributed from the polarization of conduction electrons of the Au or Ag host material in the vicinity of an Er^{3+} due to their spin angular momentum and the interaction of the next spin. For Au:Er, RKKY=(0.10±0.02) eV and Ag:Er, RKKY=(0.16±0.03) eV [93]. Because of this, the RKKY interaction is roughly three times stronger for Ag:Er than for Au:Er, resulting in a smaller total signal size.

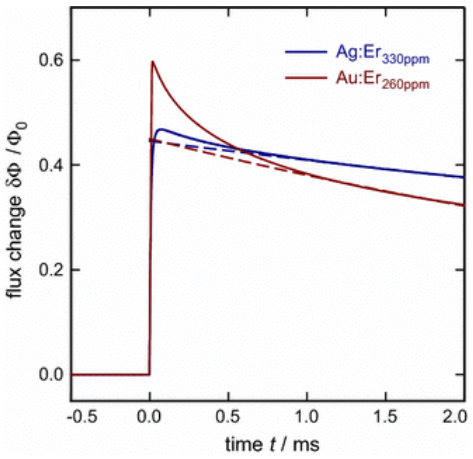

Figure 2.4: Comparison of MMC detector responses following the absorption of 5.9 keV photons using detectors that had an Au:Er or Ag:Er sensor. The observed signals were fitted with a single-exponential signal decay to produce the solid lines for t >1ms [93]

However, as Ag has ½ nuclear moment, it does not have a nuclear quadrupole moment, while Au does. Due to the Er ion's different charge distribution, which leads to host material lattice symmetry distortion and strong electric field gradients at the sites of the surrounding nuclei, the energy eigenstates of Au:Er are no longer degenerate, and a nuclear quadrupole splitting is consequently induced. Hence, below 30 mK Au:Er has an increased heat capacity because of nuclear quadrupole splitting. This splitting initially causes the signal to decay quickly in Au:Er [93], as shown in Figure 2.4. While in Ag:Er, as Ag does not have a nuclear quadrupole moment, there is no initial fast signal decay, and the overall heat capacity is reduced. The lack of fast signal decay results in equivalent performance to Au:Er. However, the absence of the fast decay time makes the signal shape simple and consequently the data analysis simpler, sometimes resulting in a higher energy resolution.

2.2 . Signal of the MMCs

One main advantage of MMCs is that the signal can be accurately predicted. There are two steps in optimizing the detector response.

- The calculation of thermodynamic properties like magnetization and heat capacity of the sensor containing paramagnetic ions embedded in the nobel metals.

- Optimization of the sensor geometry and the characteristics of the readout circuit (inductance of the pickup coil and its match with the DC-SQUID magnetometer, magnitude of the field current) that maximize the signal-to-noise ratio.

2.2.1 . Thermodynamic properties of sensor

The calculation of heat capacity and magnetization of Au:Er (or Ag:Er) based magnetic calorimeters helps in estimating the signal effectively. There are two descriptions for the calculations. One is the qualitative description from the assumption of non-interacting spins, while for the quantitative description, the dipole-dipole and RKKY interactions are also taken into account. The operating temperature region of MMCs is 10–100 mK, so only the calculations for the ground state crystal field doublet, i.e.$\Gamma 7$ Kramers doublet, are taken into consideration.

- **Qualitative description using non-interacting spins**

At low temperatures and low magnetic fields, the Au:Er behave like a two level system. Thus, the heat capacity for this Zeeman ensemble is derived from the Schottky equation as:

$$Cz = Nk_B \left(\frac{E}{k_B T}\right)^2 \frac{e^{E/k_B T}}{(e^{E/k_B T}+1)^2} \tag{2.5}$$

In the equation 2.5
N is no. of independent magnetic moments
k_B is Boltzman constant
$k_B T$ is thermal energy
E is energy splitting between two spin orientations of the ground state = $\widetilde{g}\mu_B B$, μ_B is the Bohr magneton.

A Schottky anomaly in observed (Figure 2.5). At very low temperatures, the heat capacity follows the dominant $\mathrm{e}^{-\mathrm{E}/\mathrm{k_B T}}$term, $\mathrm{C_Z}$ reaches a local maximum at $k_B T \approx 0.42E$, whereas at higher temperature the curve starts decaying $\sim B^2/T^2$.

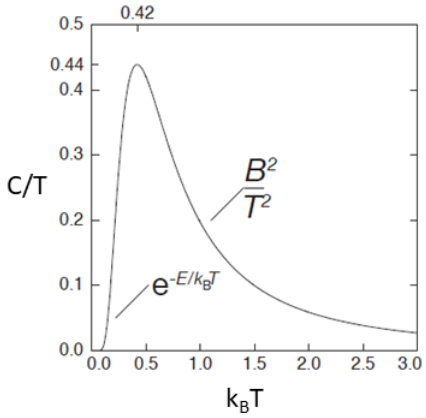

Figure 2.5: Schottky anomaly of the heat capacity for a two-level system.

The magnetization of the ensemble with the volume V is :

$$M = \frac{N}{V}\frac{1}{2}\widetilde{g}\mu_B tanh\left(\frac{\widetilde{g}\mu_B B}{2k_B T}\right) \tag{2.6}$$

- **Quantitative description with the dipole-dipole and RKKY interaction**

Mean-field approximation can be used to include the dipole-dipole and RKKY interactions in calculating the thermodynamic parameters of the sensor material (Au:Er, Ag:Er) [90]. The RKKY-interaction, which occurs when conduction electrons of the host Au or Ag material in the vicinity of an Er^{3+} get polarized due to its spin angular momentum and mediate the interaction to the next spin, makes up the majority of the contribution. The calculations were performed in [90] or Au:Er sample having a concentration of 300 ppm of 97.8% enriched ^{166}Er. For the fabrication of magnetic thermometers, Er depleted of ^{167}Er is sometimes used as ^{167}Er has nuclear spin. To compare the relative strength of both the interactions, a dimensionless parameter, which is defined as the ratio of the two pre-factors $\alpha = \Gamma_{RKKY}/\Gamma_{dipole}$is introduced.

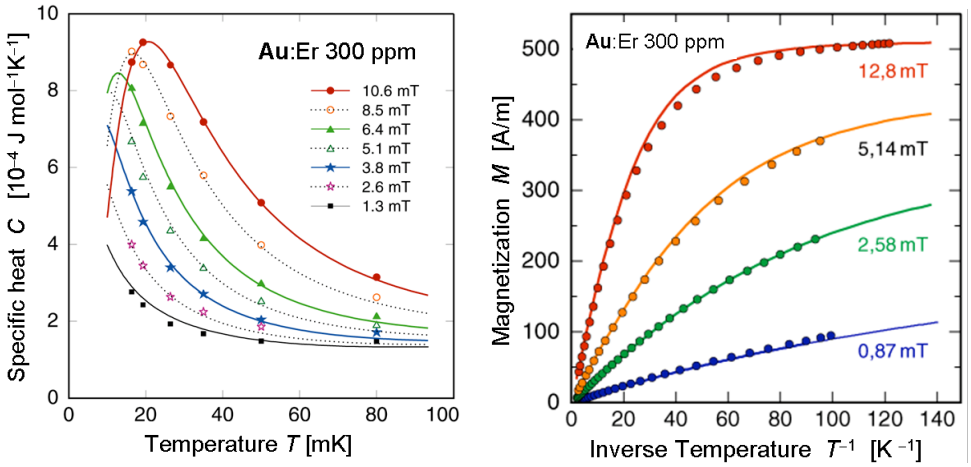

Figure 2.6: Quantitative simulation and measured data curves of a Au:Er 300 ppm sample having α=5, for the specific heat (left) and magnetization (right) as a function of the temperature and inverse temperature, respectively [73].

In the Figure 2.6, as would be expected for a Schottky anomaly, the temperature of the maximum in the specific heat depends on the magnitude of the external magnetic field. The symbols reflect measured data, while the solid lines show the outcomes of calculations performed for various magnetic fields. The calculations were performed by averaging the spin clusters to get a quantitative agreement. The maximum, however, is almost twice as wide as for a non-interacting spin system, as observed in Figure 2.5. In the plot of magnetization in figure 2.6, the magnetization deviates for the behavior of isolated spins. The authors in article [90] observed that the magnetization also deviates for the behavior of non-interacting spins. The small deviations in both C and M plots for enriched Er were observed due to:

- Due to the hyper-fine contribution of ^{167}Er, its presence in the enriched sample causes a small additional broadening of the curve.
- Due to the shape of the field coil used to magnetize the sensor, there is an additional widening caused by a fluctuation of the applied magnetic field of between 10 and 15 % over the sample.

Perhaps the most simple way to describe the magnetic characteristics of a weakly interacting spin system is in terms of the temperature dependence of susceptibility in the Curie-Weiss law, $\chi = \lambda/(T+\theta)$. Both the Weiss constant (θ), which measures the strength of the interactions, and the Curie constant (λ), which measures the concentration of spins, are proportional to one another.

2.2.2 . Detector signal readout

The magnitude of the output signal from a SQUID electronics used to measure the response of a magnetic calorimeter depends on various factors related to the calorimeter itself and the read-out electronics. A sensitive flux-to-voltage converter can be implemented using a dc-SQUID, which consists of a superconducting loop interrupted by two Josephson junctions. Each Josephson junction serves as a weak connection between the superconductors. A basic characteristic of superconducting loops is that they can contain magnetic flux solely in integer multiples of a constant known as the flux quantum Φ_0. This implies that a superconductive loop permits the penetration of an external magnetic field into its interior only when the flux passing through it is an integer multiple of the magnetic flux quantum Φ_0. The schematic diagram of a dc-SQUID is shown in Figure2.7.

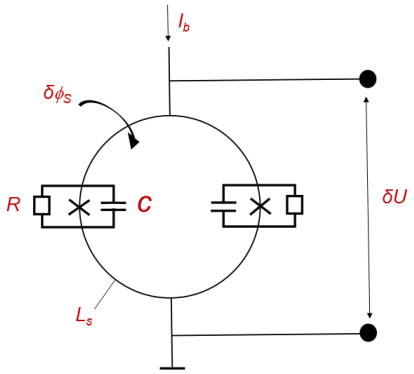

Figure 2.7: The schematic diagram of a dc-SQUID.

The links in which the superconductivity is suppressed are thin enough for cooper pairs to tunnel. The small distance between the electrodes of each junction causes parasitic capacitance. In order to inhibit the device's hysteretic behavior, each junction is shunted by a resistor R. The shunt resistors R produce noise regarding current and voltage, reducing the SQUID's apparent flux sensitivity. The electrons in the shunt resistors remain warmer than the substrate because poor electron-phonon coupling limits heat transfer efficiency from the shunt resistors to the substrate at very low temperatures. So even if the substrate temperature T is reduced, the shunt temperature will level off at a minimum value depending on the bias current, and the SQUID noise ($\propto \sqrt{T_{\text{shunt}}}$) will remain higher

than one would expect from the substrate temperature. When a small current is passed via the device. The current is carried without dissipation by tunneling Cooper pairs. However, if the device is biased at a current more than twice the critical current of one junction, a voltage drop occurs across the device. The weakly coupled superconducting loop of a SQUID is not fully superconducting and does not strictly speaking exhibit flux quantization but the DC voltage across the device depends on the magnetic flux through the inductance Ls of the SQUID periodically, where the periodic flux range is one flux quantum Φ_0. When operated in one (positive or negative) slope of this flux-voltage characteristic (transfer function) (Figure b 2.8), the device may be used as a sensitive flux-to-voltage converter.

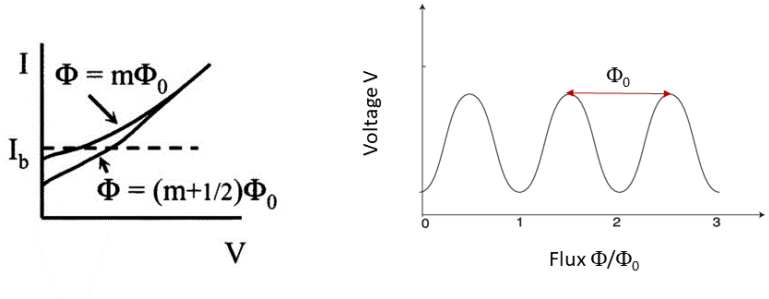

Figure 2.8: a) A typical I-V characteristic of DC-SQUID b) Flux-Voltage characteristic of DC-SQUID.

As we have seen, a SQUID has a nonlinear flux-to-voltage transfer function. In order to linearize its response, a SQUID is used in a flux-locked loop (FLL) mode, which uses a negative feedback to compensate for the flux changes caused by a signal. The flux-locked loop circuit has different parts that work together. First, a pre-amplifier amplifies the output signal from the SQUID. Then, an integrator adds up the signal from the pre-amplifier over time and sends it out. Finally, a feedback circuit is designed to provide current feedback to compensate to compensate for any variation of the flux delivered to the SQUID by the external field to be measured.

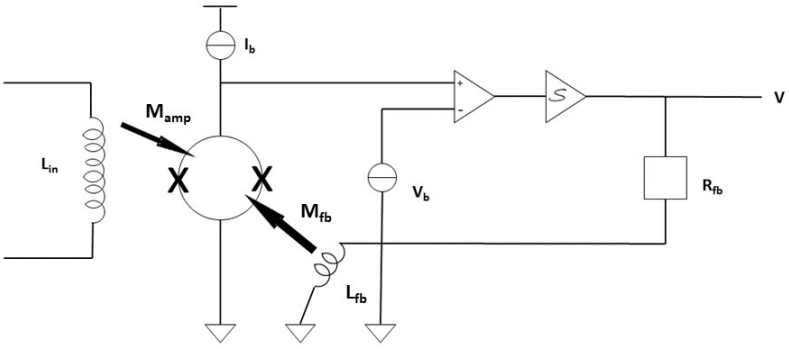

Figure 2.9: SQUID configuration in a FLL mode.

The SQUID and the sensor can be coupled using two different ways, that are discussed in the subsections below.

2.2.2.1 . Direct coupling

Direct coupling readout using a DC-SQUID is one of the simplest ways to read out an MMC. The scheme is shown in Figure 2.10. In direct coupling, the cylindrical paramagnetic sensor is placed directly within in the circular SQUID sensing loop to optimize flux coupling. The SQUID and the paramagnetic sensor are exposed to the homogeneous magnetic field perpendicular to the substrate surface. The amplitude of the signal is described by the following equation [90]:

$$\delta\phi = \frac{G}{r_{loop}}.\mu_0.V_s.\left(\frac{\partial M}{\partial T}\right)_{T_0}\frac{E}{C} \tag{2.7}$$

In the above equation,

G is the coupling constant between the change in magnetic moments and the flux change measured by SQUID magnetometer

r_{loop} is the radius of the loop of the SQUID magnetometer

μ_0 is the vacuum permeability

V_s is the sensor volume

E is the energy deposited

C is the total heat capacity of absorber (C_a) and sensor (C_s)

$\left(\frac{\partial M}{\partial T}\right)$ is the change in the magnetization of paramagnetic sensor at T_0 (temperature of heat bath).

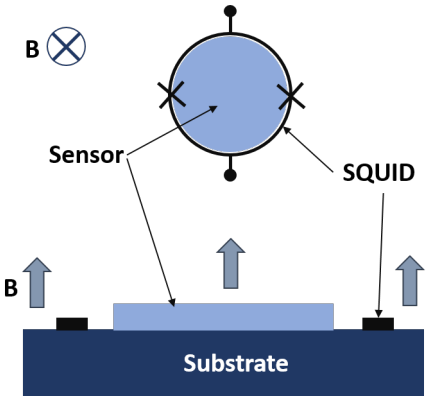

Figure 2.10: Direct coupling readout scheme via DC-SQUID (top and front view).

In the reference [90], the authors optimized the signal-to-noise ratio for the direct coupling scheme. The results showed that if the total noise is independent of SQUID, then $C_s = 2C_a$. With the circular SQUID sensing loop, the optimal sensor height (h) to radius (r) is $\xi = h/r \approx 0.25$. But if the SQUID noise greatly impacts the overall noise, then $\xi \approx 0.5$, and $C_s = C_a$. As the loop diameter of the SQUID magnetometer is usually a few micrometers, this sets an upper limit to absorber heat capacity for which the signal-to-noise ratio can be optimised. An advantage of direct coupling is the strong coupling between sensor and SQUID, a disadvantage is that the sensor temperature is given by the SQUID chip temperature, that can be substantially higher than the cryostat's base temperature, as mentioned before.

2.2.2.2 . Coupling via superconducting flux transformer

A typical superconducting flux transformer is a closed superconducting circuit consisting of a pickup coil (L_p), which reads out the signal of a magnetic sensor, and an input coil (L_{in}), which couples this signal to the readout SQUID. Initially, the pickup coil featured a spiral shape, but later on, a meander-shaped geometry was adopted. The pickup coil is a thin film placed under the Ag(or Au): Er thermometer. To provide strong inductive coupling, the distance between the sensor and the pickup coil is kept as minimal as possible by having a very thin insulation layer. The temperature sensor is connected to an on-chip heat bath formed by a layer of several micrometers thick, highly conductive, electroplated Au to thermalize the detector. For this, a thin, conductive stripe of thermal conductance G, connects the temperature sensor to the on-chip heat bath. The decay time of the pulse depends on G and the total heat capacity of the absorber and sensor as $\tau_d = C_{tot}/G$. Several small-area gold posts link the absorber and sensor, resulting in a small contact area between the sensor and absorber. This significantly lowers the athermal phonon loss during the early stage of detector thermalization that would otherwise result in an asymmetric line broadening [93].

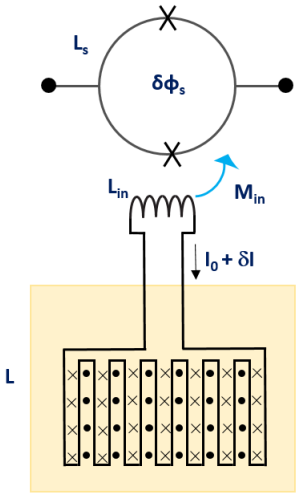

Figure 2.11: Schematic diagram of coupling of SQUID via a superconducting flux transformer using single meander.

A superconducting persistent current switch is used to inject a large persistent current I_0 into the superconducting circuit of the flux transformer. This persistent current generates the magnetic field required to magnetize the thermometer. See Figure 2.11 for reference. The current in the meander creates an inhomogenous magnetic field, but more importantly, the field is perfectly stable in time. Any magnetization change in the aligned spins affects the meander's flux. When a particle deposits its energy in the absorber, it leads to its increase in temperature and decreases the magnetic susceptibility of the sensor. A change in magnetic flux in the pickup coil ($\delta\mathbf{\Phi}$) leads to a subsequent change in magnetic flux in the SQUID ($\delta\mathbf{\Phi}_s$).

$$\delta\mathbf{\Phi}s = \frac{M_{in}}{L_p + 2\left(L_{in} + L_w\right)}\delta\mathbf{\Phi} \tag{2.8}$$

In the equation 2.8, M_{in}corresponds to the mutual inductance between the SQUID and input coil. L_w (typically of the order of a nH) is the parasitic inductance of the bonding wires that link the pickup coil of the detector with the input coil of the SQUID.

The advantage of using a flux transformer is that there is no upper limit on the absorber heat capacity for which optimizing the signal-to-noise ratio is possible. A pickup coil's size is unbounded, except its inductance must match an available SQUID's input coil: The maximum magnetic coupling occurs when the input coil's inductance is equals that of the meander. The spins of the magnetic sensor are, on average, closer to the pickup loop with the meander design than in the case of a cylindrical sensor placed in a circular pickup loop; hence, a meander coil is more sensitive than a circular loop, and the magnetic coupling between spins and the pickup loop is stronger. Also, this coupling scheme enables the spatial separation of the detector and SQUID to prevent power dissipation of the shunt resistors near the detector. The drawback of using a single meander is that due to the field current running through the input coil of SQUID, there is a degradation in its performance. The V-Φ characteristic is reduced by the magnetic field in the Josephson junctions. It reduces the SQUID sensitivity.

2.2.2.3 . Coupling via superconducting flux transformer using double meander

A second meander in parallel with the first meander is implemented in the new design to avoid the degradation of the SQUID performance. Hence, the field current runs through the two meander coils. See figure 2.12 for reference. An advantage of this coupling scheme is that the input coil of the SQUID is not required to carry the large persistent current I_0 needed to create the biased magnetic field for the sensor. Two meandering pickup coils of superconducting Nb holding a persistent current is used to create the field. The magnitude of this persistent current is large and close to the critical current of the pickup coil. It can be introduced into the superconducting loop the two meanders form together. An electric resistance heater implements a current switch between the two superconducting meandering pickup coils. An electrical bypass line connects these. By passing a current through the heater to turn it on; the bypass line turns into a conductor while the meandering pickup coil remains superconducting. Only the current change δI, which is brought on by the deposition of energy in one of the sensors, needs to be carried by the input coil and the connections between the pickup coils and the current-sensor SQUID. Another advantage of this scheme is that near the SQUID, the fields are also small, and the inductance of the interconnects is also less sensitive to fluctuations produced by the vibration of those lines. The meander is enclosed in a superconducting loop, which helps reduce the magnetic Johnson noise created inside the metallic sensors and absorbers.

In Figure 2.12, a coupling scheme for reading out two sensors at once using the pickup coil in the shape of a double meander is shown. The two meanders are linked in parallel to the input coil of a current-sensor SQUID to create a flux transformer. For optimal coupling, the inductance of the input coil (L_{in}) is half the value of the inductance of any one of the meanders (L). Mathematically it can be written as:

$$\left(\frac{\delta\Phi_S}{\delta\Phi}\right)_{max} = \left(\frac{k\sqrt{L_{in}L_s}}{L+2L_{in}}\right)_{max} = \frac{k}{2\sqrt{2}}\sqrt{\frac{L_S}{L}} \tag{2.9}$$

In equation 2.9, k is a dimensionless coupling constant. The pickup coil's connections are made in such a way that both pixels display signals with distinct polarities. Because of this, it is possible to

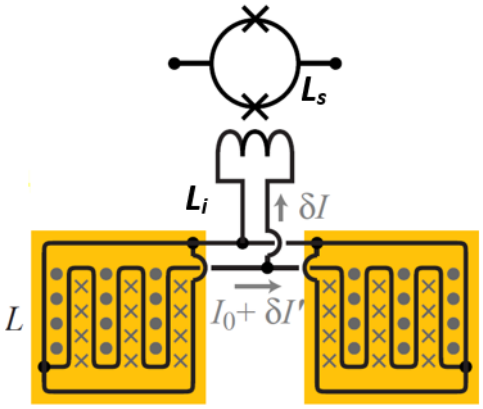

Figure 2.12: Coupling schemes to measure the magnetization of paramagnetic sensors with a dc-SQUID [108].

identify the pixel in which an event happened using the polarity of the SQUID signal. Another benefit of this wiring is that it creates a first-order gradiometer in the detector, essentially canceling out homogeneous changes in the external magnetic background fields and fluctuations in the temperature of the heat bath.

In this thesis, The MMC chips manufactured during the EMPIR (European Metrology Research) projects MetroBeta and MetroMMC are used for the measurements [107]. The MMCs are coupled to the readout SQUID via a superconducting flux transformer. The schematics are shown in the Figure 2.13.

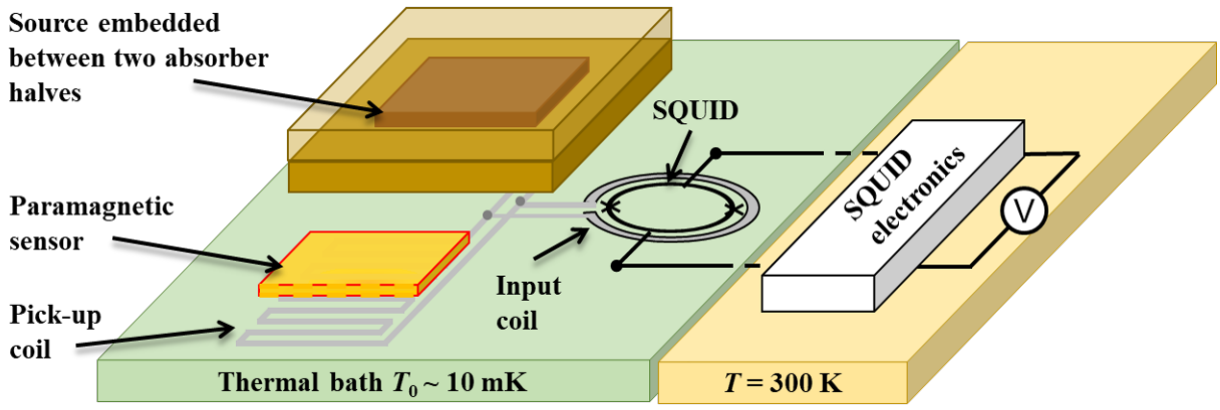

Figure 2.13: The coupling scheme of Metrobeta project MMC readout via a superconducting flux transformer [107].

2.3 . Signal to noise ratio and energy resolution

The energy resolution of metallic magnetic calorimeters is determined by the time-dependent signal-to-noise ratio and the signal's time structure. The best-energy-resolution requirement is maximizing the signal size while minimizing noise to attain the highest signal-to-noise ratio. MMCs have two types of noises associated with them. The intrinsic noise sources like thermodynamic fluctuation noise, magnetic Johnson noise, $1/f$ noise can be reduced but not entirely removed. The extrinsic noise sources like temperature fluctuation, electromagnetic interference, vibrations, amplifier noise etc can be appropriately suppressed by a well-designed detector and refrigeration system [61, 73, 90, 101].

2.3.1 . Response of the detector

The detector signal form as a function of time can be calculated by modeling the parts of the detector as a thermodynamic canonical ensemble made up of two systems. MMCs consist of three main parts. First is the normal metal absorber, where the particle or photon deposits its energy. Second is the paramagnetic thermometer for the detection of the temperature rise of the absorber and sensor, and the third component is the heat bath (or heat sink), which maintains a constant temperature, allowing the previous two components to return to their baseline temperature after energy deposition. The absorber and sensor can be treated as two thermal systems of the canonical ensemble, as shown in Figure 2.14.

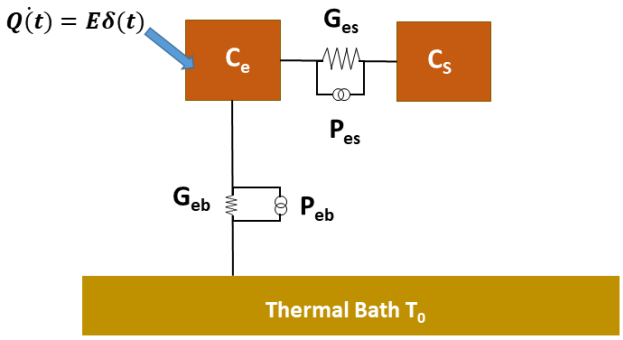

Figure 2.14: Thermal model of a magnetic calorimeter consisting of two subsystems [109].

The first system comprises the absorber, represented by the heat capacity of its conduction electrons C_e, and the second system comprises the thermometer (sensor) represented by the magnetic moments having heat capacity as C_s. For electrons to be in thermal equilibrium inside the detector, it is assumed that the absorber and the paramagnetic sensor are in strong thermal contact. In the sensor, the spin heat capacity is dominating (~ two orders of magnitude higher than conduction electrons within the paramagnetic alloy at typical Er concentrations). In the absorber, the heat capacity of the conduction electrons C_e dominates at millikelvin temperatures, while that of the phonons is viewed as negligible. Furthermore, any energy E deposited in the detector is supposed to thermalize immediately within the conduction electron system. A strong thermal link of conductance G_{es} links the two systems, and P_{es} is the corresponding noise power of this link. A conductance G_{eb} having noise power P_{eb} connects the conduction electrons to the thermal bath at temperature T_0. Here it

can also be assumed that the magnetic moments are non-interacting, as the energy of interaction between moments is substantially lower than that of Zeeman-splitting in the external field. Hence, the paramagnetic sensor's total magnetic moment (m) measures the energy content $es(es = -mB)$, of the spins. The pickup loop's magnetic flux, $\delta\mathbf{\Phi} \propto \delta m$, is proportional to the magnetic moment. The flux in the SQUID offers a direct measure of the energy content of the spin system.

The following two differential equations are used to model the time evolution of the energy contents of the two systems, E_e for electrons and E_s for spins. An external power input $P(t) = E\delta(t-t_0)$, appears due to the deposition of an energy E at timet_0 in the detector.

$$\dot{E}_e = C_e\dot{T}_e = -G_{es}\left(T_e - T_s\right) - G_{eb}\left(T_e{-}_0\right)E\delta\left(t\right) \tag{2.10}$$

$$\dot{E}_s = C_s\dot{T}_s = -G_{es}\left(T_s - T_e\right) \tag{2.11}$$

From the above equations, the spin temperature T_s is important to understand as the spin response gives the magnetic signal of the sensor.

$$\Delta T(t) = T_s(t) - T_0 = \frac{E}{C_e + C_s}\left(-e^{-t/\tau_r} + e^{-t/\tau_d}\right) \tag{2.12}$$

The equation 2.11 indicates that upon energy E deposition into the detector, the temperature increases exponentially to a local maximum value with constant τ_r, (τ_r is the rise time) and subsequently decays exponentially with constantτ_d, (τ_d is decay time) as the energy is evacuated to the heat bath. The constants are affected by thermal conductivities and heat capacities. The interaction between spins and electrons serves as a basic constraint on the rise time constant. It was pointed out in [73] that the signal-to-SQUID-noise ratio was determined to be best when the heat capacities of the sensor and absorber were equal. To get the value of rise and decay time, we will keep the assumption of almost equal heat capacities of absorber and sensor and weak thermal coupling to the heat bath $G_{\mathrm{eb}} \ll G_{\mathrm{es}}$.

$$\tau_r = \frac{C_e}{G_{es}} \tag{2.13}$$

$$\tau_d = \frac{C_e + C_s}{G_{eb}} \tag{2.14}$$

2.3.2 . Intrinsic sources of noise

2.3.2.1 . Thermodynamic fluctuation noise

The statistical fluctuations in the detector's energy content caused by random energy exchange between the absorber and the heat bath via the thermal link are the main cause of thermodynamic fluctuation noise (TFN). In detectors using metallic magnetic thermometers, the thermal connection is often made of a metal wire or film, and electrons carry the energy exchange across it. The extent of the energy fluctuations across the metal wire or film is determined by the definition of statistical mechanics:

$$< \Delta E^2 >= k_B T^2 C \tag{2.15}$$

In the above equation, $C = C_e + C_s$ is the heat capacity of the detector. Here, the energy fluctuation is independent of the thermal link conductivity. This can be interpreted as Poisson fluctuations in the number of the energy carriers if they have a mean energy of $k_B T$ in the calorimeter. This is the case when the heat capacity of the absorber is larger than that of the sensor.

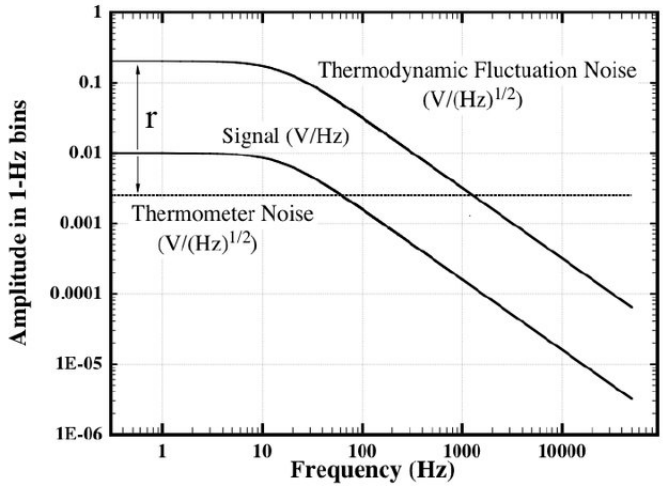

Figure 2.15: The power spectrum in the frequency domain of the exponential decay signal pulse and the noise power spectrum of the thermodynamic fluctuations [61].

In Figure 2.15, the authors in [61] showed that the power spectrum of both TFN and exponential signal pulse have the same shape. They are both constant at low frequency and start decreasing at $f_c = G/(2\pi C)$. Therefore the signal-to-noise ratio is constant throughout all frequency bins. Each bin provides an estimate of the signal amplitude, and assuming that the noise in various bins is uncorrelated, the signal-to-noise ratio will improve as the square root of the number of bins averaged increases. The usable bandwidth determines how the thermodynamic fluctuation noise affects the energy resolution: in the limit of infinite bandwidth, the energy resolution would have no limitation by the TFN. The relationship between the energy resolution and bandwidth is as $\sqrt{\Delta f}$. Averaging a bandwidth of $\Delta f = G/C = 2\Pi f_c$ will result in a root mean square of energy resolution, $\triangle E_{rms} = \sqrt{k_B C T^2}$. In reality, the usable bandwidth is constrained by at least two factors. One of them is the existence of white noise, such as the noise from a thermometer. The signal-to-noise ratio declines significantly, starting from the frequency when the thermodynamic fluctuation noise drops below the white noise level. The second factor is the signal rise time τ_r, which is caused by the thermalization of energy in the detector and its coupling to the spins in the thermometer. The signal-to-noise ratio will decrease above the frequency, $f_b = 1/\tau_r$ due to white noise. As long as the signal-to-noise ratio remains constant, the resolution improves as the square root of the bandwidth, but once it starts to decline rapidly, there is little further gain; hence the "useful bandwidth" will be proportional to the frequency f_b. Since the noise associated with thermodynamic fluctuations is decreasing as$1/f$, once the TFN drops below the level of white noise, the overall noise will be dominated by SQUID noise. Furthermore, to have a high-resolution detector, the magnitude of the TFN $\sqrt{k_B C T^2}$ and $\sqrt{\frac{f_c}{f_b}}$ needs to be minimized [106].

2.3.2.2 . Magnetic Johnson noise

Magnetic Johnson noise is a source of noise inherent to MMCs. It is noise caused by thermally induced currents (thermal motion of conduction electrons) in a conductor. The impacts of this noise source are especially noticeable in an MMC, which consists of a metallic absorber and sensor which are placed close to a pickup loop intended to measure flux changes induced by the sensor. According to Harding and Zimmerman, the reciprocity theorem can be used to compute the flux noise generated in the meander loop as a result of fluctuating currents in a conductor. A time-varying current in the meander loop causes eddy currents in the close-by conductors, and the associated losses may be characterized by the loop's apparent resistive impedance $R(\omega)$. After that, the impedance may be utilized to calculate the flux noise in the loop. Magnetic Johnson noise can be minimized by lowering the metal's conductivity with non-magnetic impurities at the price of a slower thermal energy transport across the sensor and/or absorber. The fluctuating currents that run parallel to the meander are mostly responsible for this noise production. The root mean square of flux noise is represented as

$$\sqrt{S_\theta} = \mu_0 \sqrt{C_m \sigma k_B T V} \tag{2.16}$$

In the above numerical calculation for the fluctuations, V is the volume of the sensor, C_m is a parameter regarding the meander geometry, σ is the conductivity of the sensor and $S_\theta$is the flux noise with units as $\frac{\phi}{\sqrt{Hz}}$. The Magnetic Johnson noise in a meander is determined by the characteristics of the circuit layout and its coupling to the sensor. The MMC flux noise increases with an increase in sensor volume for both cylindrical sensors with circular pickup loops and planar sensors with meander-shaped pickup loops. Yet, because the change in flux in a meander-shaped pickup coil per unit of deposited energy increases with decreasing meander pitch (pitch of the meander is the center-to-center distance between two neighboring meanders) and decreasing planar sensor thickness, the signal-to-Johnson-noise ratio in this design may be massively enhanced. The noise in a meander can be decreased by adding discontinuities (lamination) in the metallic sensor, preventing thermal currents from flowing in directions that couple to the stripes or the edges. This is possible without significantly altering the area of the sensor and hence the signal response [90].

2.3.2.3 . $1/f$ noise of sensor

$1/f$ noise is an additional noise observed in Au:Er (or Ag:Er) sensors of the MMCs due to the erbium ions of the sensor. The author in [104] compared the noise of a bare gradiometer SQUID to that of a SQUID with one Au:Er sensor with an erbium concentration of 900 ppm positioned in one of the SQUID gradiometric loops or two identical sensors positioned in both gradiometric loops. The plot in Figure 2.16 shows the results obtained. The plot shows that for frequencies less than 100Hz, the flux noise has a $1/f$ dependence that grows with the number of Er ions present. The author also pointed towards the $1/f$ dependence on the concentration of erbium ions in the sensor. This noise is also temperature-independent at temperatures between 20 mK and 4.2 K.

An explanation regarding the origin of this noise was given in [105] that spin-spin fluctuations, which exist in spin-glasses and often have a $1/f$ dependence, might explain the $1/f$ noise from the Au:Er. It was demonstrated that the source of the noise is not the interaction of erbium ions with the quadrupole moments of gold nuclei. The noise spectra of two comparable detectors, one using Au:Er as sensor material and the other using Ag:Er, were examined and revealed the same $1/f$ noise

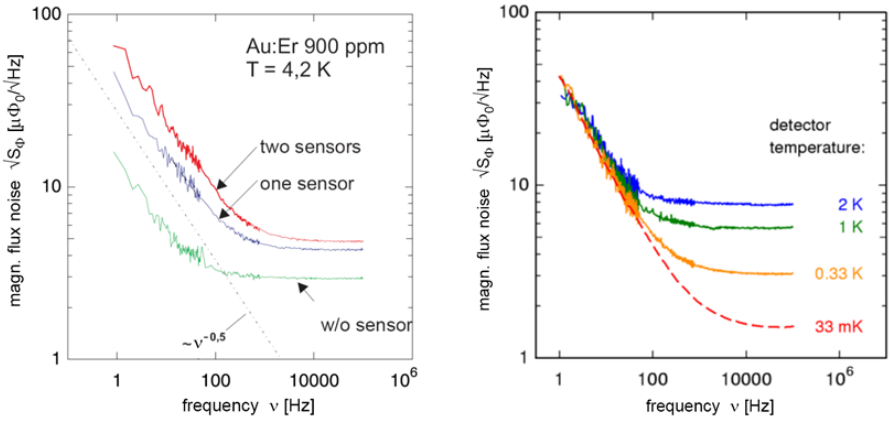

Figure 2.16: a) Plot describing the $1/f$ noise in MMCs with no, one, and two sensors. b) Noise spectra of a magnetic calorimeter recorded at different temperatures. While the white noise varies with temperature as expected, the $1/f$ noise remains constant [104].

contribution per spin. The natural Ag has a nuclear spin of $I = 1/2$ and lacks a quadrupole moment. Therefore this interaction cannot be the source of this noise contribution. The exact cause of the $1/f$-type noise is still unknown.

2.3.2.4 . Readout noise

DC-SQUIDs are read out by the room-temperature electronics. When the DC-SQUID is operated in FLL mode, its dynamic range is increased by a few tens of flux quanta. SQUID noise may severely impair the overall signal-to-noise ratio of non-optimized detector designs and can, in this case, limit the energy resolution. The noise contribution from the readout electronics to a SQUID at 4.2K or below can be decreased to minimal levels at room temperature by utilizing low-noise field-effect transistors or operational amplifiers. Modulating the SQUID with an alternating current flux significantly reduces readout circuit drift as well as high-frequency electromagnetic interference but reduces the useful bandwidth. For MMC readout, usually, non-modulated SQUID readout is employed.

The Johnson noise of the shunt resistors R parallel to the Josephson junctions is the source of the intrinsic SQUID noise. The noise is temperature dependent, and because Johnson noise is current noise, it is turned into flux noise by the SQUID's self-inductance L_S. The additional $1/f$-dependency in the intrinsic noise spectrum appears to be caused by defects in the SQUID material. First, thermal movement of trapped flux lines, or vortices, inside SQUID circuits can cause changes in critical current and $1/f$-noise. Second, trapping and de-trapping of electrons within Josephson junctions can induce variations in critical current and $1/f$-noise. Third, tunneling systems in the dielectric layers can also cause $1/f$-noise [110, 111].

2.3.3 . Energy resolution

The energy resolution is calculated using the optimal filtering as discussed in [90, 106]. This is done because the noise in different time bins is correlated if its spectrum is frequency dependent,

and the calculation of the energy resolution becomes difficult in the time domain. However, the noise in various bins is uncorrelated in the frequency domain if it is stationary. At the linear small-signal limit, it appears likely that this will apply to practically every system. Applying this to the two systems thermodynamical canonical ensemble (described in subsection 2.3.1) with the constraints that $C_s = C_e$, and non-limiting SQUID noise, The resulting rms energy resolution is

$$\Delta E_{rms} = \sqrt{4k_B C_e T^2} \left[\frac{G_{eb}}{G_{es}} + \left(\frac{G_{eb}}{G_{es}} \right)^2 \right]^{\frac{1}{4}} \tag{2.17}$$

ΔE rises linearly with temperature and the square root of the heat capacity of the absorber. This expression suggests that the energy resolution can be infinitely improved if there is perfect thermal conductance G_{es} between the absorber (electrons) and the thermometer (spins). But, in the case of Au:Er (or Ag:Er) sensor, the electron-spin relaxation time, which obeys the Korringa relation in the case of low spin concentrations, is the limiting material parameter. Hence, equation 2.17 is rewritten as

$$\Delta E_{rms} = \sqrt{4k_B C_e T^2} \left(\frac{1}{\beta(1-\beta)} \frac{\tau_r}{\tau_d} \right)^{\frac{1}{4}} \tag{2.18}$$

Here β is the relative contribution of C_s to C_{tot}, ($C_{tot} = C_s + C_e$), $\beta = \frac{C_s}{C_{tot}}$. There is only one free parameter that can be utilized to optimize the energy resolution of the detector since the signal rise time τ_r is defined by the sensor material and the recovery timeτ_d and C_e and T are chosen according to the specific application. ΔE_{rms} is a minimum for $\beta = 1/2$ and this is consistent with the discussion in subsection 2.3.1 on signal to SQUID noise ratio, that the best energy resolution is achieved when $C_e \approx C_s$. Hence, the intrinsic energy resolution is expressed as:

$$\Delta E_{rms} = \sqrt{4k_B C_e T^2} \sqrt{2} \left(\frac{\tau_r}{\tau_d} \right)^{\frac{1}{4}} \tag{2.19}$$

The results of the measurement of the noise frequency dependence of the different noise contributions in a metallic magnetic calorimeter readout by a SQUID via transformer-coupling are shown in Figure 2.17 [93].

The authors in [90] observed that the relevance of thermodynamic fluctuation noise is limited to a relatively small frequency range. Hence, in reality, the influence of $(\tau_d)^{-1/4}$is much less. One of the main causes of noise, not just at low frequencies, is the $1/f$ noise contribution attributed to the Er ions within the temperature sensor. There was very little influence of magnetic Johnson noise. The total noise was significantly impacted by SQUID white noise, including the noise of the SQUID electronics operating at room temperature. As a result, it limits the overall signal-to-noise ratio and, consequently, the detector's energy resolution. The Er concentration needs to be optimized to have an overall balance between the energy resolution degradation due to the $1/f$ noise contribution of Er ions and the influence of SQUID readout noise on the overall noise spectrum.

MMCs have a fast signal rise time due to the combination of metallic absorbers with metallic magnetic thermometers. If the contact between the absorber and the thermometer is metallic, that is, there is no oxide or other insulating layer present, the heat delivered by the conduction electrons can

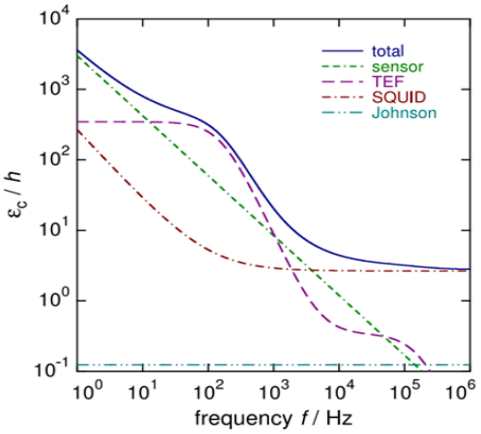

Figure 2.17: Frequency dependence of the different noise contributions in an MMC read out by a SQUID via transformer-coupling [93].

travel into the thermometer without causing any significant thermal resistance. The thermometer's electron-spin coupling is extremely quick; thermal equilibrium between conduction electrons and spins is frequently achieved in less than a microsecond, even at low mK temperatures. The decay time is affected by the conductance of the thermal link (G). A fast decay time reduces energy resolution to some extent.

3 - Experimental details

3.1 . Optimization of the detector

The MMC detectors used in this thesis were developed during the two EMPIR projects: MetroBeta (2016-2019) and MetroMMC (2018-2021). The first step towards any calorimetric decay data measurement is selecting a suitable absorber material and dimensions for each radionuclide. This task was performed by Monte Carlo simulations using a code called PENELOPE. PENELOPE stands for "PENenetration and Energy LOss of Positrons and Electrons" [112]. The simulations are performed to obtain the appropriate absorber dimensions, where all the decay energy, except that of neutrino, is deposited. The intrinsic quantum efficiency of various materials and geometries for absorbers is calculated. The results are compared to select the one with the lowest heat capacity and sufficient efficiency at the MMC working temperature, i.e., 20mK (the real operating temperature in our dilution refrigerator is in the range 10 - 15, max. 20 mK, but for the numerical MMC design optimization 20 mK was the default temperature). From the EMPIR project MetroBeta [37, 107], five sets of MMC chips with various sensor heat capacities for various absorber heat capacities were constructed to cover a broad range of energies, from a few tens of keV up to 1 MeV.

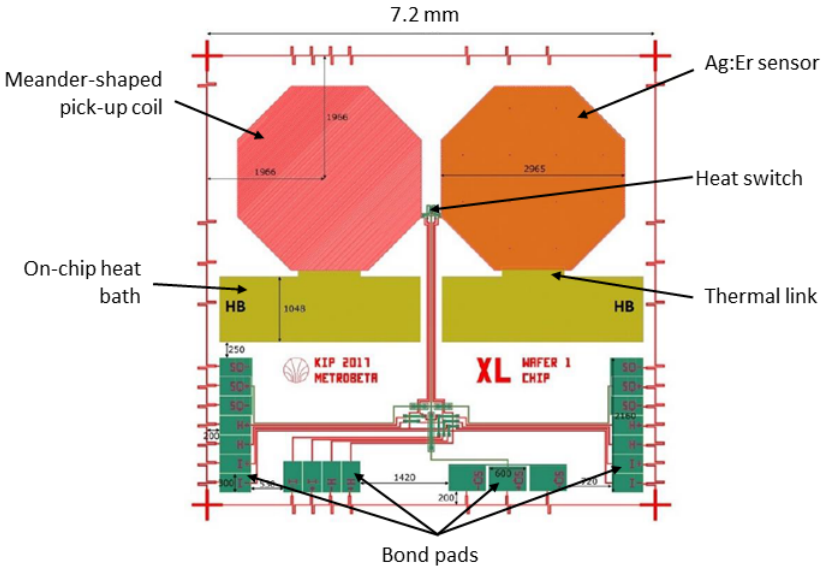

Figure 3.1: Metrobeta detector design

The design and micro-fabrication of the MMCs were performed by the Quantum sensors group of Kirchhoff Institute of Physics, Heidelberg University. There are three main constraints while optimizing the designs. These are:

- The heat capacity of the MMC sensor should be matched to that of the chosen absorber.

- The meander-shaped pickup coil's inductance should be twice as large as the inductance of the chosen SQUID's input coil.
- At the specified operating temperature (20 mK), the thermal link between the MMC detector and the on-chip heat bath pad should allow a signal decay time of ~1 ms.

The detector optimization process starts with the chosen absorber's heat capacity. Only a small number of detectors, i.e., five detector sizes, were designed and manufactured in MetroBeta and MetroMMC because, even with a 30–50 % mismatch between the sensor and absorber, the energy resolution of MMC-based detectors only declines by about 10 %, and is still significantly better than the resolution of conventional spectrometers. This is possible because the loss in signal-to-noise ratio can partially be compensated by other optimization parameters, among which the field current can be adjusted most freely once the MMCs are fabricated.

Table 3.1: Overview of MMC detector parameter values per design [37].

MMC detector type	XS	S	M	L	XL
Optimal absorber heat capacity (pJ/K at 20mK)	8	28	110	400	1700
Meander and sensor area (μm²)	249×249	335×335	538×538	1427×1427	2663×2663
MMC sensor heat capacity (pJ/K)	7.57	17.9	50.6	308	1170
Single meander inductance (nH)	3.4	3.1	8	56	196
Linewidth of pickup coil (μm)	2.5	5	5	5	5
Pitch of pickup coil (μm)	5	10	10	10	10
Expected flux coupling (coupling ratio between meander and sensor) (%)	3.8	4	2.6	0.8	0.5
Optimum field current (I_F) (mA)	38.2	67.8	75.7	63.3	67.1
Expected signal size ($m\Phi_0$/keV)	23.2	12.9	6.41	2.97	1.61
Expected energy resolution (eV)	5.17	9.46	19.1	37.5	74.4

From the set of detectors shown in Table 3.1, the best detector for a particular radionuclide embedded in an optimal absorber is then selected. Utilizing a small number of detectors to cover a wide range of heat capacities significantly reduces the amount of time and resources needed for optimization and fabrication. The parameters like the line width of the meander, pickup coil pitch, and sensor area and thickness are fixed during the optimization process, the parameters of doping concentration cannot be altered as easily. Further, detector optimization is carried out for each absorber heat capacity once these parameters have been fixed. Only variables that can be easily merged or altered on

a single substrate are utilized. This process yields a set of detectors produced in a single fabrication run and on the same wafer, and the wafer produced overs a wide range of decay energies. During the fabrication of all the MMCs designed in the project MetroBeta had a paramagnetic sensor of erbium in Ag with a concentration of 310 ppm and thickness of 3 µm. It was assumed that the SQUID white noise level is $0.35\ \mu\psi_0\mathrm{Hz}^{1/2}$ and the SQUID $1/f$ noise level at 1 Hz is $2.6\ \mu\psi_0\mathrm{Hz}^{1/2}$. The overview of all five MMC detector parameters is given in Table 3.1.

There are some differences between the MMC chip designs from the MetroBeta and MetroMMC projects. These are shown in the Figure 3.1 and 3.2.

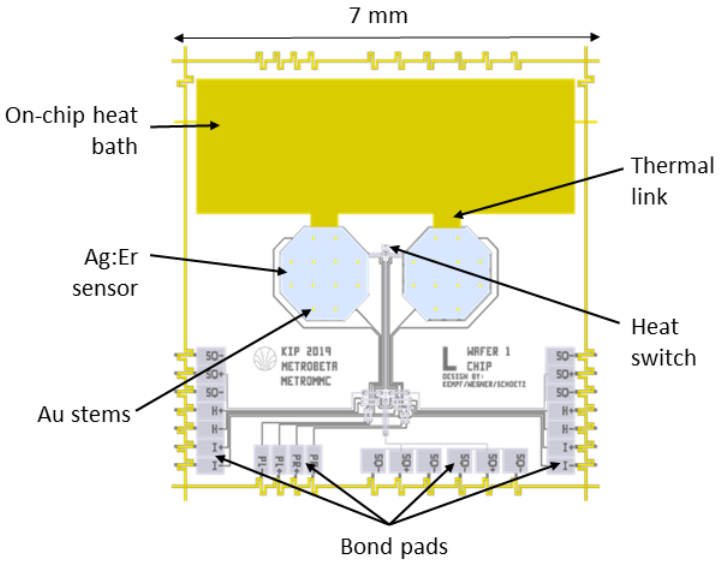

Figure 3.2: MetroMMC detector design

In both designs, an Au metal link produced by sputtering connects the sensor to an on-chip heat bath. The link's length to cross-section ratio is adjusted to correspond to the detector's target decay time. This provides the opportunity to thermally connect the on-chip heat bath to the sample holder, which is directly attached to the base plate of the cryogenic system. The parameters are given in Table 3.1 remained the same for both designs, but to allow for more uniform thermalization, the separate heat baths connected to each of the two sensors in the MetroBeta design were merged in the MetroMMC design. This also helps to reduce the temperature gradients between both sensors that potentially degrade the energy resolution. In both the designs, small cylindrical gold posts (stems) on top of the sensors are used to minimize the force application when gluing the absorber to the sensor as the pressure gets 'amplified' by the ratio between the sensor area and the overall post area. Also, these gold stems provide a metal-metal connection between the sensor and absorber as the glue drops are placed in between these stems. Another change was the addition of an optional on-chip electrical resistance heater. This enables on-chip calibration using prescribed current pulses. The distance between the pulser leads and the pickup coil is designed to be suitably large because the currents flowing through the wires connecting the pulsers can create stray magnetic fields that

might couple into the pickup coil and imitate a signal. In the two-pixel MMC chips, a second absorber without a source can be attached to the second sensor to quantify the background.

3.2 . Source and absorber preparation techniques

In this thesis, the decay energy spectroscopy (DES) technique has been used for the measurements. In this measurement mode, the source is fully enclosed between the two absorber halves to have a 4π detection geometry. The process is explained in Figure 3.3 to prepare a 4π absorber-source ensemble using diffusion welding. The decay radiation from the source, except the neutrino, is thermalized inside the absorber. Since DES detectors like MMCs have long thermal time constants, the overall energy of the decay is measured rather than the energies of the individual particles involved in the decay. High-quality sources are required to achieve optimal detection efficiency with minimum spectrum distortion.

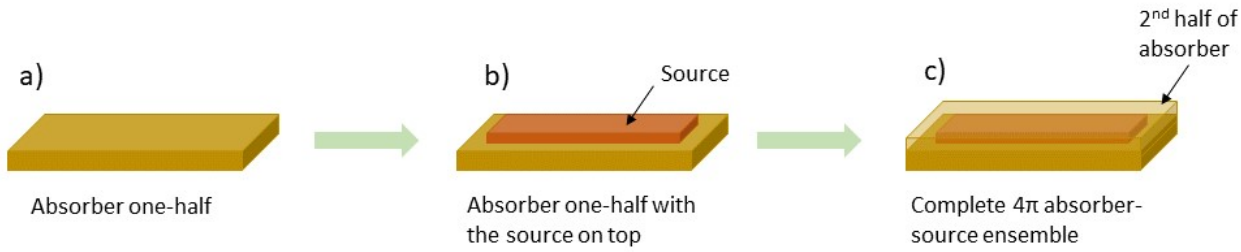

Figure 3.3: Steps to have 4π absorber-source ensemble.

This section describes the Monte-Carlo simulations performed for obtaining absorber-source geometry using a code called PENELOPE. The methods for preparing radioactive sources appropriate for EC and beta spectra measurements in 4π geometry and embedding them in metallic absorbers are also described. The preparation of the source is critical for accurate measurements with MMCs. The method of depositing the source can affect the measured spectrum shape. The previous measurements performed with MMCs showed that if salt crystals are formed in the source layer, electrons emitted in the decay process lose a part of their energy in the source material. This energy would not be entirely converted to detectable heat and leads to spectrum distortion and consequently also degradation in the energy resolution [115]. The sources to be used for the 4π measurements need to be thin and homogeneous to allow the radiation to pass through the source material into the absorber. In this thesis, the three different source preparation methods have been adapted. The manual drop deposition is used for preparing $^{125}\mathrm{I}$ on silver foil and $^{14}\mathrm{C}$ on gold foil sources, along with using electrodeposition for $^{54}\mathrm{Mn}$,$^{59}\mathrm{Ni}$ and $^{51}\mathrm{Cr}$. The source preparation using a micro-drop dispenser on gold nanofoam foil (NPAu) is used for $^{59}\mathrm{Ni}$ source.

3.2.1 . Monte-Carlo simulations using PENELOPE

Monte-Carlo (MC) simulations using PENELOPE were performed to select a suitable absorber material and the minimum necessary dimensions for each radionuclide to be measured. During the MC simulation of radiation transport, a particle's trajectory (history) is characterized by a series of random interaction events [112]. During these events, the particle may change its path, lose energy, and occasionally generate secondary particles. The MC simulation for any experimental setup consists of the numerical generation of these random histories. These histories are generated using a set of differential cross-sections (DCS) for the relevant interaction mechanisms. The DCSs establish the probability distribution functions (PDF) of the random variables that form the histories, such as interaction types that take place, all the different free paths between successive interaction events, and energy loss or angular deflection in a particular event. After determining these PDFs, we can create random histories utilizing suitable sampling techniques. Assuming a sufficient number of histories are generated, we can achieve quantitative insights into the transport process by averaging over the simulated histories.

PENELOPE simulates coupled Photon, electron, and positron transport in any arbitrary setup. This setup is made up of several homogeneous areas (bodies) that are constrained by sharp (and passive) boundaries. Photon and electron transport with energies ranging from 50 eV to 1 GeV can be simulated in PENELOPE [112]. The optimization of suitable absorber material and thickness is the first step towards MMC detector optimization, and then using the results from MC simulation to prepare the absorber and source. For each radionuclide measured in this thesis, the MC simulation was performed. In all those simulations, the main steps remain the same. First, using a geometry package called 'pengeom' in PENELOPE, random electron-photon showers are generated in material systems. A binary file called 'shower.exe,' included with the package, creates electron-photon showers in a slab and projects them onto the computer screen plane.

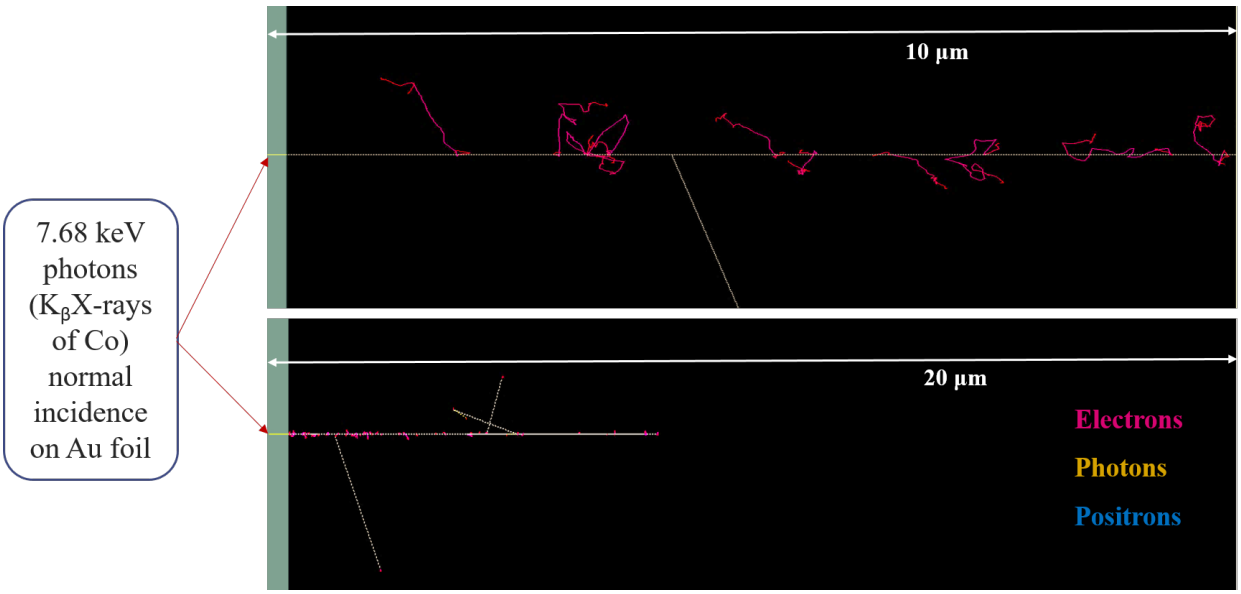

Figure 3.4: Monte-Carlo simulated showers for ^{59}Ni.

Depending on their energy and type, primary particles may begin to move in random directions (isotropic inner source) or in the direction of the lateral surface's inward normal (external or internal beams). The time passed since the emission of the original particle that launched the shower was used to calculate particle age. The colors and intensities of the electron, photon, and positron tracks change according to the particle's energy. An example of the case of $^{59}\mathrm{Ni}$ is shown in the Figure 3.4. In this case, the absorber material chosen was Au foil for the photon absorption of 7.68 keV (the highest energy photon emission in the decay of $^{59}\mathrm{Ni}$). For the Au foil of thickness 10 µm, there was the escape of high energy electrons and photons, but for 20 µm thickness,the simulated showers showed 99.99% photon absorption.

Once the appropriate absorber thickness and material have been selected, the expected decay energy spectrum for the complete absorber-source ensemble in 4π geometry is simulated. Two major programs are included in the Penelope distribution package: pencyl (which simulates electron-photon transport in cylindrical geometries) and penmain (for generic quadric geometries). The geometry for the absorber-source ensemble for measurement of $^{59}\mathrm{Ni}$ is defined as shown in Figure 3.5. PENELOPE reads the required information (interaction cross-section, physical properties, mean free path, stopping powers, etc) for the materials of the absorber source from the input material data file generated by the program 'material'. The decay data of the radionuclide to be simulated is read from the text file 'nuclide.nuc' in the specific format, which can downloaded from Nucléide - Lara Library for gamma and alpha emissions by LNHB [35]. The main programs, pencyl and penmain, provide an output file containing generic data such as the number of simulated showers, simulation speed, average numbers of generated secondary particles, average deposited energy, and so on. The result of simulations for the geometry in Figure 3.5 is shown in Figure 3.6, showing the simulated spectrum in the arbitrary outer detector. The spectrum showed that there is no escape of the photons from the $20\ \mu\mathrm{m}$ thick Au absorber.

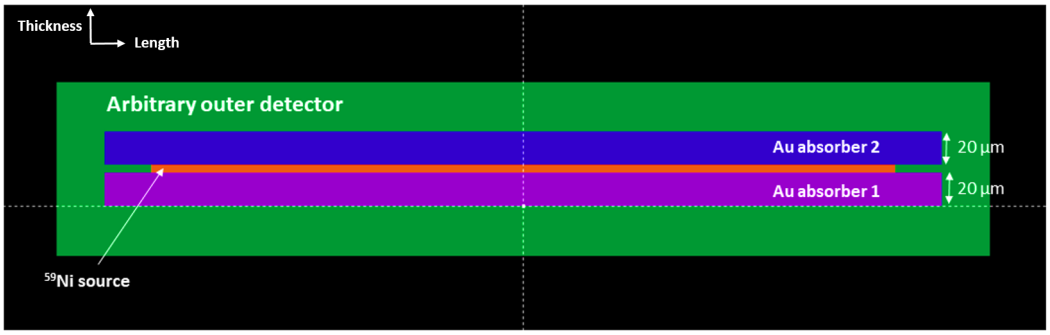

Figure 3.5: The geometry for the absorber-source ensemble for measurement of $^{59}\mathrm{Ni}$ with an arbitrary outer detector made of Au to check if there is any escape or not.

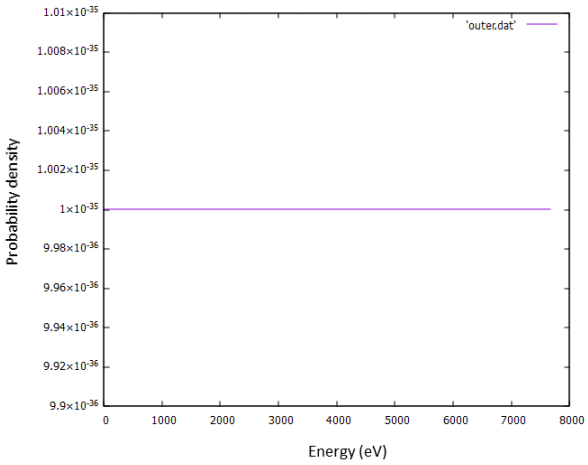

Figure 3.6: The simulated spectrum in the arbitrary outer detector for geometry in Fig 3.5.

3.2.2 . Autoradiography

Autoradiography was used in this thesis to check homogeneity and activity after each source foil was prepared. It is also used to choose an appropriate part of the source with the required activity for the measurement. Autoradiography is a non-destructive technique used to characterize activity intensity and relative distribution in prepared sources [126, 127].

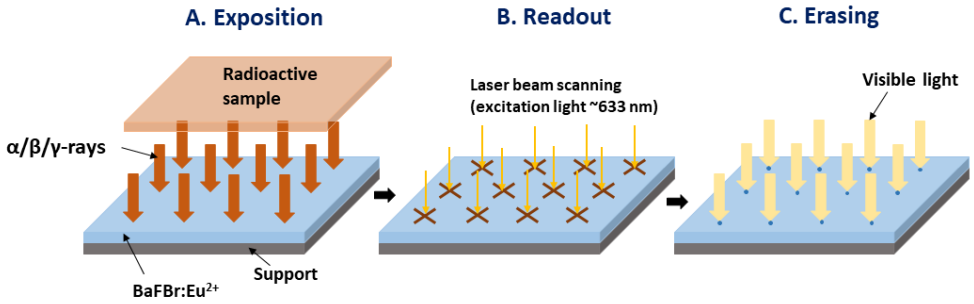

Figure 3.7: The autoradiography process.

The digital autoradiography method is based on the Phosphor image plate (IP) technology. In IP systems, the photosensitive grain is made of barium fluorohalide crystals doped with europium activator (BaFX: Eu^{2+}; X = Cl, Br, I), and the image is created using photo-stimulated luminescence (PSL). The latent image is created when incident radiation oxidizes the Eu^{2+} to Eu^{3+} and promotes electrons to the conduction band. In fluorohalide vacancies known as F-centers, electrons are held captive until the laser light scanning the IP stimulates them to return to the Eu^{3+} activator. A photo-multiplier tube (PMT) detects the characteristic light that is released during this transition. The electrical signal from PMT is then converted into digital information by A/D conversion for image display and analysis. The autoradiography process is described in Figure 3.7. To perform the autoradiography, the source

impression is made, placing the source on the IP, which is then read out. In the thesis, the high-resolution imaging plate BAS-SR 2040 from Fujifilms is used with the scanner Amer-sham Typhoon.

3.2.3 . Manual drop-deposition

Drop deposition is a standard method for producing radioactive sources with a manual pipette or pycnometer, as shown in Figure 3.8. In this method, a small droplet of a radioactive solution is dropped onto a substrate and allowed to dry to form a thin coating of the radioactive material. The activity of the deposited source can be traceable through the weight of the deposited solution. Typical radionuclide solutions contain certain salt loads (carrier). To maintain thermodynamic stability and to not lose any activity on the vial walls, radionuclide solutions used for metrology usually contain a minimum concentration of carrier, i.e., a stable isotope of the same element or, if no stable isotope exists, a stable element with similar chemical properties.

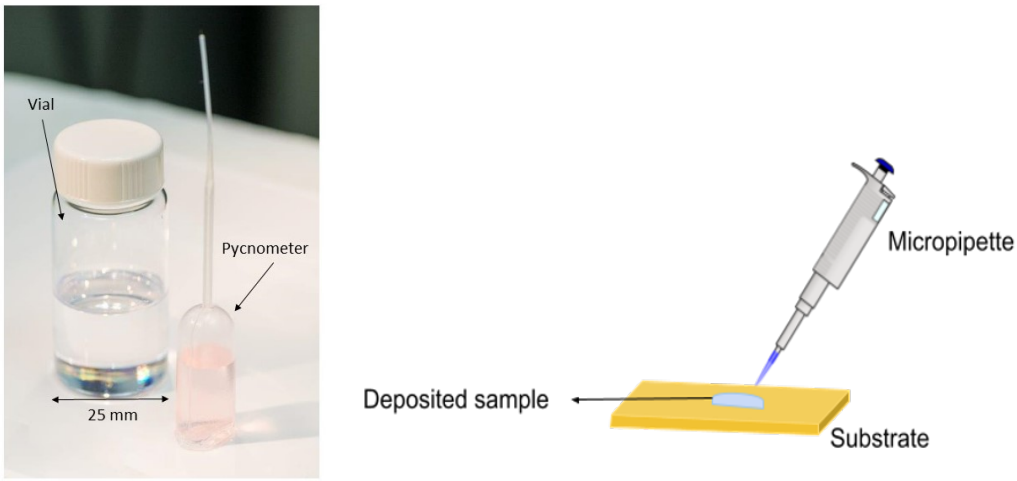

Figure 3.8: Drop deposition using a pycnometer and using a micropipette.

This means that drop deposition often leads to the formation of large (of the order of micrometers) salt crystals. Previous studies have revealed that salt crystals can cause considerable spectrum distortion due to incomplete thermalization. It was shown by numerical calculations in [132] that recoil nuclei are absorbed in a few tens of nm of material. If the thickness of the deposited source is in few µm, then the majority of the recoil energy is absorbed in the source layer rather than the absorber. Monte Carlo simulations in our group have revealed that (beta or Auger) electrons lose a considerable amount of energy within a few nanometers of typical salts composing radioactive sources (unpublished). In the case of α-decay, the impact of nuclear recoil is significant in the obtained spectrum. Therefore, only a portion of this energy is released as heat to the metallic absorber, and some of it is not even converted to heat. Instead, it creates dislocation defects or metastable states such as long-lived electron-hole pairs, distorting the spectrum [97, 113, 115, 116].

Drop deposition can also be performed using a micro-drop dispenser; see Figure 3.9 for reference. With the micro-drop dispensing machine, the individual drop size can be decreased to a few picolitres, avoiding the formation of large salt crystals. With a placement precision of better than 20 µm, commercial micro-dispensing systems can deposit single droplet quantities of less than 50 pL;

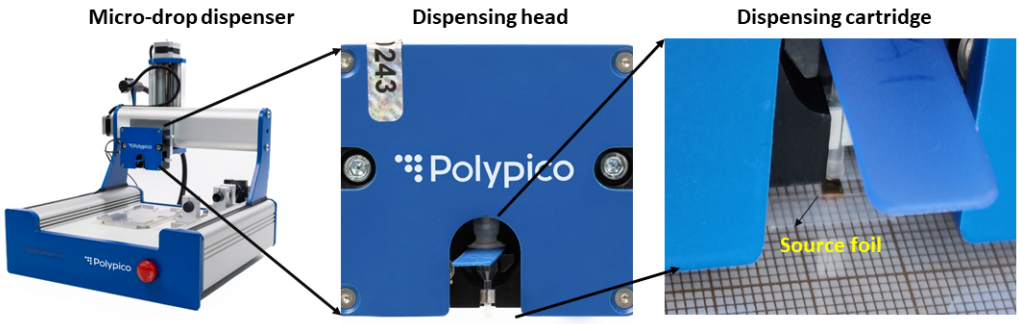

Figure 3.9: Drop deposition using automated micro-drop dispenser. The foil shown in the third figure is the nanofoam foil (2.5 ×2.5 ×0.01 mm^3) used for $^{59}\mathrm{Ni}$ source preparation.

also, the solution can be dispensed over a large area. Also, instead of using a planar metal substrate, metallic nanofoam can be used to improve the quality of the sources. Incorporating radioactive solutions in nanoporous metal samples leads to fine source dispersion into foil material, constraining the crystals to the pore size of tens of nanometers.

3.2.3.1 . Iodine-125

$^{125}\mathrm{I}$ disintegrates by 100% electron capture via the excited level of 35.5 keV of $^{125}\mathrm{Te}$ into the ground state of $^{125}\mathrm{Te}$ and it is an allowed transition. It has a half-life of 59.388 days. The decay scheme is shown in Figure 3.10. Although iodine cannot be electrodeposited, it has a strong chemical affinity for silver. When silver is exposed to an iodine-containing solution, it forms an extremely thin layer of AgI, ideally a single and complete mono-layer. The ideal situation will be preparing a new highly polished silver surface in order to exclude any oxidation on the surface and to immerse it in a sufficiently concentrated iodine solution to get a mono-layer. The critical task here is to obtain a single silver iodide mono-layer on a smaller surface than that of an MMC absorber, containing sufficient activity to obtain a well-defined spectrum in terms of statistics within an acquisition time of a maximum of a few weeks. This is determined by the nuclide's half-life and the ratio of active-to-inactive material. The available bonding sites on the silver surface that radioisotopes can occupy depend on the stable-to-radioactive isotope ratio.

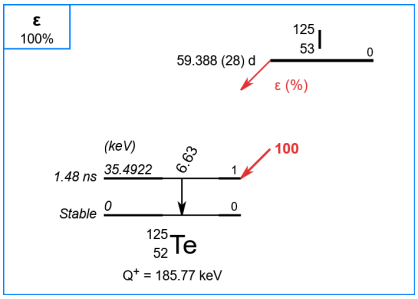

Figure 3.10: Decay scheme of $^{125}\mathrm{I}$ [35].

The $^{125}\mathrm{I}$ solution obtained in the MetroMMC project had a mass activity of 3.2 MBq/g, a concentra-

tion of 50 µg/g $Na_2S_2O_3$ and 50 µg/g NaI in January 2021. The requirement for the measurement was to have ~ 10 Bq activity on a small area of a few tenths of a mm^2 of a silver iodide (AgI) mono-layer. The source solution was deposited on a 10 µm thick silver foil. Four sources with varying activity levels were prepared because it was unknown how far a complete silver iodide mono-layer would form. The details are given in Table 3.2 and in Figure 3.11. Source 1 and 2 was deposited from the original mass activity solution, and source 3 and 4 were from a water-diluted solution of activity 300 kBq/g. Subsequently, the foil was rinsed with water to remove crystallization that might lead to spectrum distortion and air-dried. The resulting sources should essentially consist of a very thin AgI layer and have higher spectroscopic quality than standard drop-deposited sources of a dried compound crystallized in arbitrary crystalline sizes. However, the deposits had a visible boundary, indicating the formation of salt crystals that remained even after rinsing the foil with water and air drying. An autoradiography (Figure 3.12) performed with the sources reveals that the source activity distributions are in-homogeneous. The activity is concentrated in a ring-like structure near the edge of the source. This kind of activity distribution is typical of drop-deposited sources. It is likely that during the drying of the solution, when the activity was more and more concentrated towards the edge, a thicker AgI layer formed. However, it cannot be excluded that despite the rinsing, some crystallized material has remained on the foil surface.

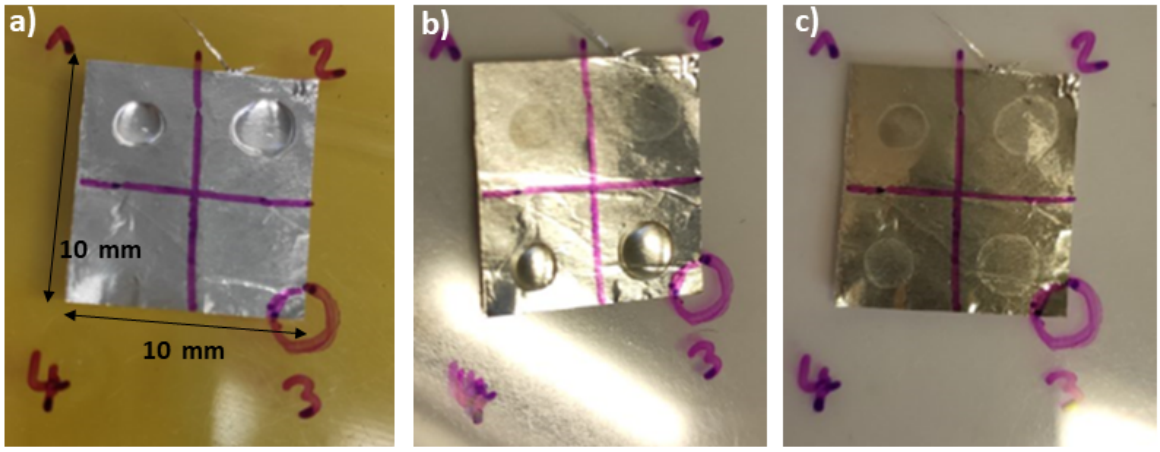

Figure 3.11: a) Drop deposition of two sources (3 mg; 6 mg) from an ^{125}I solution of 3.2 MBq/g. b) Drop deposition of two sources (3 mg; 6 mg) from an ^{125}I solution of 300 kBq/g. c) The silver foil with the four sources after drying and rinsing to remove crystallization.

In principle, this can be found by scanning electron microscope (SEM) imaging. However, since usually, one will not introduce a potentially contaminating radioactive sample into an SEM, the imaging can only be performed on a sample made from non-radioactive material of the same composition and prepared with the same technique. In the given case, in the middle of the source, the deposit was hardly visible, and we considered that the salt load, if any, was sufficiently small. After determining the approximate activity density from the autoradiography, a small part of the source foil with approximately 10 Bq activity was cut out. To further enhance the source's spectroscopic quality, the source foil's cut-off piece was repeatedly folded, laminated, and diffusion welded, thus spreading and

Table 3.2: Main characteristics of the ^{125}I source deposits. The indicated activity levels correspond to the activity of the deposited drop but not necessarily to the activity of the AgI layer. Some of the activity may have formed salt crystallization that was dissolved when rinsing the foil with water.

Source no.	Mass (mg)	Mass Activity (MBq/g)	Deposited activity (kBq)	Activity after rinsing (kBq)	Diameter (mm)
1	3	3.2	9.6	0.98	2.9
2	6	3.2	19.2	1.18	3.75
3	6	0.3	1.8	0.11	3.7
4	3	0.3	0.9	0.09	3.0

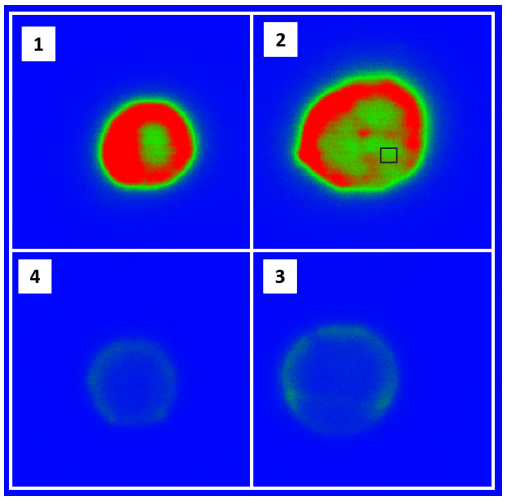

Figure 3.12: Autoradiography of deposited sources. The source number 2 was selected. The black square marked in source 2 is the place from where the source of the 10 Bq activity was cut out.

incorporating the active material into the silver foil volume. This technique, referred to as "kneeding," is somewhat time-consuming but can considerably reduce the spectrum distortion due to salt crystallization in 4π measurements. It can also be used to improve the quality of standard drop-deposited sources. It has been shown that with increasing number of kneeding cycles, the radioactive deposit is broken into ever smaller particles, reaching a nanometric scale after at least ten cycles. At the end of the kneeding process, the silver foil with the embedded ^{125}I activity was laminated to a thickness of 6 µm, and a 260 µm × 260 µm square with an estimated activity of 10 Bq was cut out [116].

3.2.3.2 . Carbon-14

The ^{14}C beta spectrum measurement was part of the MetroBeta project. ^{14}C has a half-life of 5700 years and decays by 100 % β^- transition to the ground state of ^{14}N. It is an allowed transition. Its decay scheme is shown in Figure 3.13.

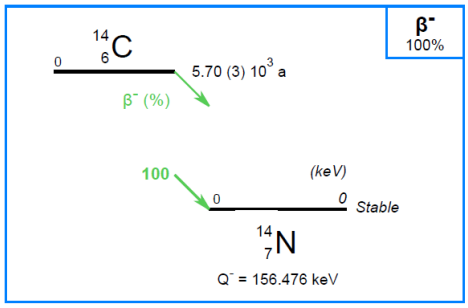

Figure 3.13: Decay scheme of $^{14}\mathrm{C}$ [35].

The first measurement was performed in 2019 [37], before the start of the thesis. Due to a broken glue layer that attached the MMC to the detector holder, the energy resolution of the spectrum was deteriorated during the 2019 experiment. To address this, a subsequent measurement was carried out within this thesis. A carrier-free solution of high activity of 370 MBq/g was chosen to obtain a high-quality source. The $^{14}\mathrm{C}$ atoms were bound in the volatile organic compound 1,3-thiazole. It was directly drop deposited on a 25 µm thick gold foil, see Figure 3.14, thick enough to stop all beta particles up to the end point of the spectrum (156.5 keV).

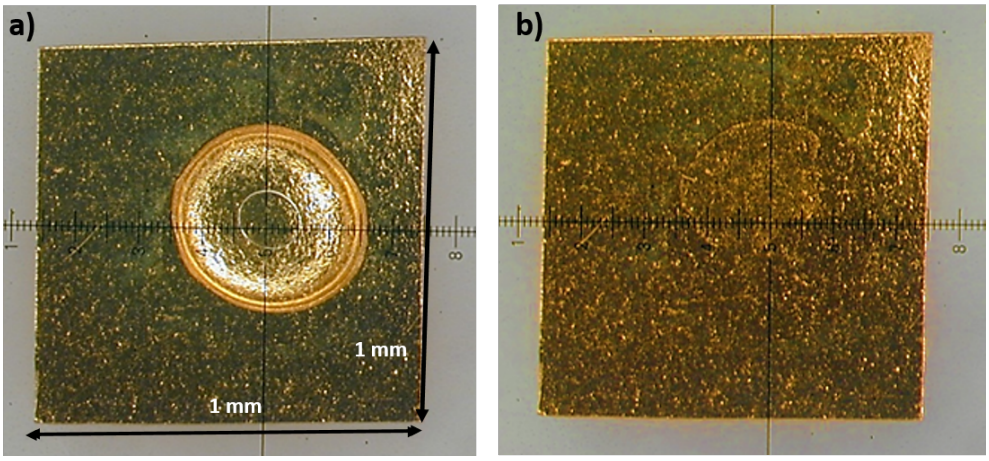

Figure 3.14: a) Drop deposition of $^{14}\mathrm{C}$ bound in 1,3-thiazole on the 25 µm thick Au foil b) Source foil after air drying.

After drying, the deposit was barely visible, even under an optical microscope, so the source was considered high quality. Since 1,3 thiazole is a volatile organic compound, diffusion welding was not a viable option for source enclosure. The absorber source foil was folded over and slightly pressed to enclose the source. Gold is highly ductile and retains its form after folding; no beta electrons can escape from being absorbed in the gold absorber. Because gold is an excellent thermal conductor at very low temperatures, the thermal contact between the two halves of the absorber via the bending is sufficient. The activity of the deposited source was 22 Bq. The final dimensions of the gold absorber were $1\,\mathrm{mm}^2 \times (2 \times 25\,\mu\mathrm{m})$.

3.2.3.3 . Nickel-59 with micro-drop dispenser

Nickel-59 disintegrates by electron capture directly to the ground state level of $^{59}\mathrm{Co}$. This is a 2^{nd} forbidden non-unique transition and has a half-life of 76,000 years. The decay scheme is shown in Figure 3.15.

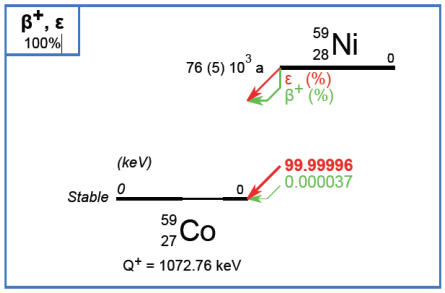

Figure 3.15: Decay scheme of $^{59}\mathrm{Ni}$ [35].

Two different types of sources were prepared for this measurement, one by micro-drop dispenser on gold nanofoam foil and the second by electrodeposition on gold foil. De-alloying is a simple process for creating metals in nanoporous form. To prepare the gold nanoporous foil (NPAu), a wet etching using 20% $\mathrm{HNO_3}$ for 2 hours at 50°C was performed. Usually, the NPAu is very fragile, so to support it first, the $\mathrm{Au_{0.3}Ag_{0.7}}$ (wt%) alloy foil (2 ×2 ×0.006 $\mathrm{mm^3}$) was diffusion welded to gold foil (2.5 ×2.5 ×0.01 $\mathrm{mm^3}$). See Figure 3.16 for process steps. The diffusion welding was performed at 400°C for 2 hours. The diffusion welding of NPAu onto the surface of one-half of the gold absorber supports the NPAu [113, 114]. After diffusion welding, the final thickness of joined foils was 14 µm.

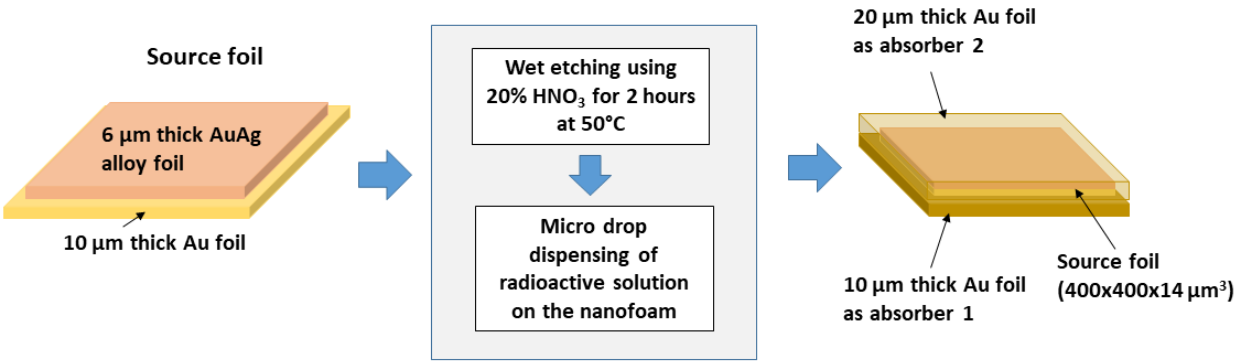

Figure 3.16: Steps for preparing the $^{59}\mathrm{Ni}$ drop deposited source on Au nanofoam (NPAu) foil.

After performing wet etching, the silver from the alloy is completely dissolved. The remaining gold creates a nanoporous structure. The SEM images are shown in Figure 3.17. The duration of the etching process, temperature, $\mathrm{HNO_3}$ concentration, and stoichiometry of the AuAg alloy will affect how large the pores will be in the gold.

The drop deposition was performed using an automated micro-drop dispenser. The composition of the radioactive solution obtained from NPL as a part of EMPIR project MetroMMC was $1\mathrm{NHCl} + 0.1\ \mathrm{N}\ \mathrm{HNO_3} + \mathrm{N}$

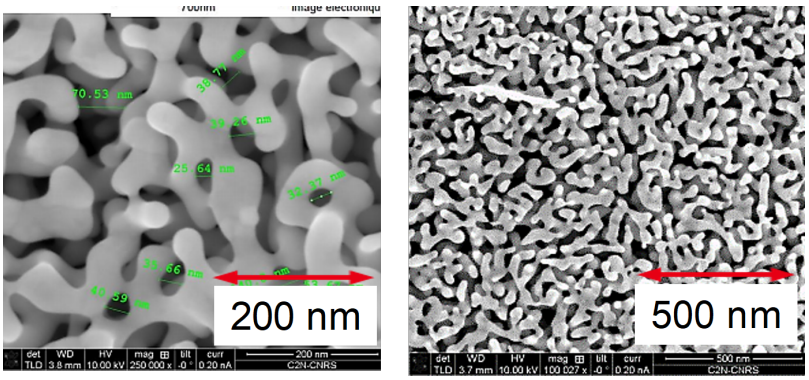

Figure 3.17: SEM image of the NPAu foil.

with an initial mass activity of 81 kBq/g in March 2021. The concentration of Ni in the electrolyte was 28 µg/g in 10 mL of the solution. After the source foil is dried, a thin deposit is formed as the solution fills the NPAu cavities and is dried on a very large surface.

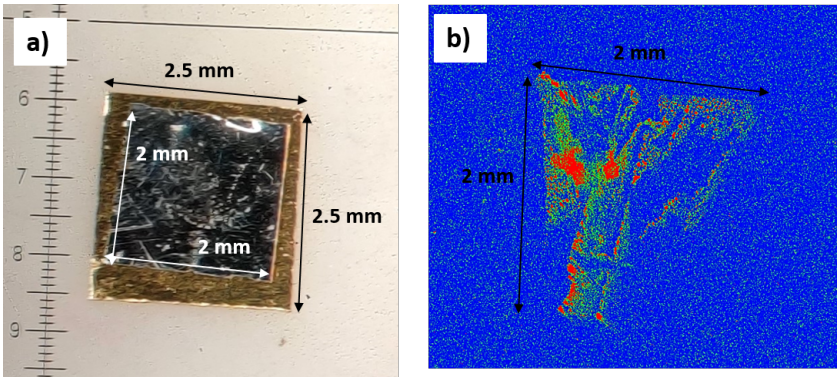

Figure 3.18: a) AuAg alloy on Au foil after diffusion welding. b) Autoradiography of the prepared source. The autoradiography does not really represent the full activity distribution since a major part of the radiation from the activity enclosed in the nanofoam pores is stopped within the nanoporous gold.

The initial parameters of the automated micro-drop dispensing machine were adjusted to achieve a radioactivity level of 3-4 Bq on the NPAu foil source with dimensions 400 x 400 µm. Four positions on the 2000 x 2000 µm NPAu foil were selected to drop the solution. For 3 Bq activity, the drop volume was 41 nL (1216 drops), and for 4 Bq, it was 55 nL (1671 drops). Autoradiography was also performed after the solution was dried to get the activity distribution of the prepared source, which is shown in the Figure 3.18.

3.2.4 . Electrodeposition

Electrodeposition is another process by which thin and, in some cases, metallic source layers can be produced. This thesis uses this technique to prepare sources for three radionuclides: $^{51}\mathrm{Cr}$, $^{54}\mathrm{Mn}$, and $^{59}\mathrm{Ni}$, for their fractional electron capture probability measurements. During electrodeposition, if no metallic deposit can be obtained, often an oxide/hydroxide layer will form. This can still be a

high-quality source if the thin, homogeneous layer exhibits very low self- absorption. Unfortunately, electrodeposition can only be used with metals, and the process is not universally applicable; instead, it must be customized to the desired element. For this thesis, an in-house adapted two-electrode cell electrodeposition setup was used, as shown in Figure 3.19

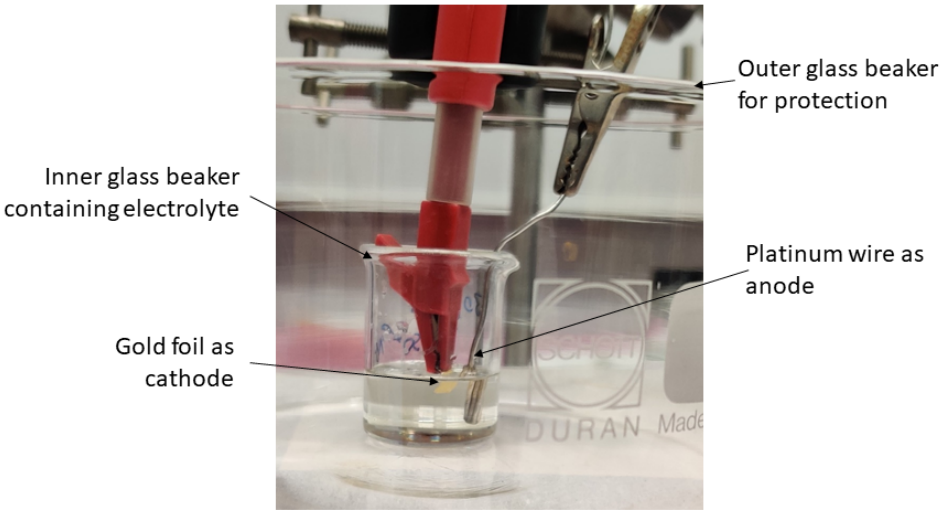

Figure 3.19: In-house adapted two-electrode cell electrodeposition setup.

Furthermore, the electrolytes used for radionuclide deposition typically contain only trace amounts of the desired element. A high deposition yield of more than 10% is required to reduce the amount of often expensive and scarce radioactive material required. The high deposition yield also helps in minimizing the dose rate for the operator performing the process. Aside from the difficulty of fabrication, a disadvantage of electrodeposition is that the process in not fully quantitative. Even with a very well-characterized process, the precise amount of deposited material and the total activity of the source will still be unknown to some extent. We calculate the deposition yield using liquid scintillation counting and by gamma spectrometry to verify the amount deposited. Also, autoradiography was performed for each source prepared to check homogeneity.

3.2.4.1 . Chromium-51

$^{51}\mathrm{Cr}$ decays by electron capture to the ground state of $^{51}\mathrm{V}$ (90.1%) and to the 320 keV excited level (9.9%). The transition is allowed. $^{51}\mathrm{Cr}$ has a half-life of 27.704 days. The decay scheme is shown in Figure 3.20.

Chromium plating is a well-studied procedure in the plating industry. At the industrial level, the electroplating is performed using a chromic acid solution which usually contains a Cr(VI) compound. The hexavalent chromium compound is highly toxic and needs to be reduced to Cr(III), which is less toxic. However, due to a highly stable $[\mathrm{Cr}(\mathrm{H_2O})_6]^{3+}$ complex, it is not easy to deposit the Cr coating from a simple aqueous Cr(III) solution [117, 118]. Therefore, in this thesis, the plating was performed with Cr(III) compound in an organic solvent. The electrolyte was prepared from water and Dimethylsulfoxide (DMSO), an organic solvent. The $^{51}\mathrm{Cr}$ was obtained as a solution of $\mathrm{CrCl_3}$ in 0.5M HCl.

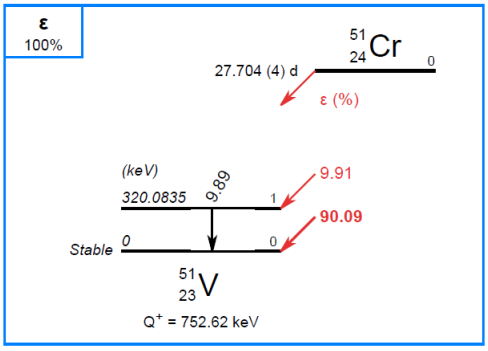

Figure 3.20: The decay scheme of $^{51}\mathrm{Cr}$ [35].

Chromium was electrodeposited onto the surface of the gold foil (7x7 mm^2, thickness 5 µm) cathodes (99.99% Au) in an in-house adapted two-electrode cell with platinum wire used as an anode. The electrolyte contained 5 ml of DMSO with 50 µL of $\mathrm{CrCl_3}$ solution. At the time of source preparation, there was around 110 kBq of activity in the electrolyte. The constant current source for reducing Cr(III) to Cr(0) was used at a current of 5 mA and 200V for 30 minutes.

Two sources for Liquid Scintillating Counting (LSC) were prepared with a Hionic-Fluor (HF) LSC cocktail to measure the deposition yield. The first LSC source was prepared after the first 15 mins of electrodeposition and the second after 30 mins. The Au foil corners were observed to turn brown between 25-30 mins from the start of electrodeposition. The electrodeposition yield determined from the two LSC sources was 71.6% for LSC-1 (after 15 mins) and 92.4% for LSC-2 (after 30 mins), respectively. The deposit obtained was metallic and thin. The autoradiography of the source also pointed towards a homogeneous deposit, as shown in Figure 3.21b. The final activity of the sources obtained was $1.02\ \mathrm{kBq/mm^2}$. As the activity was quite high to work with the source immediately, the source was kept for 3 half-lives without any manipulation to reduce the activity to a handleable amount of 127.5 Bq.

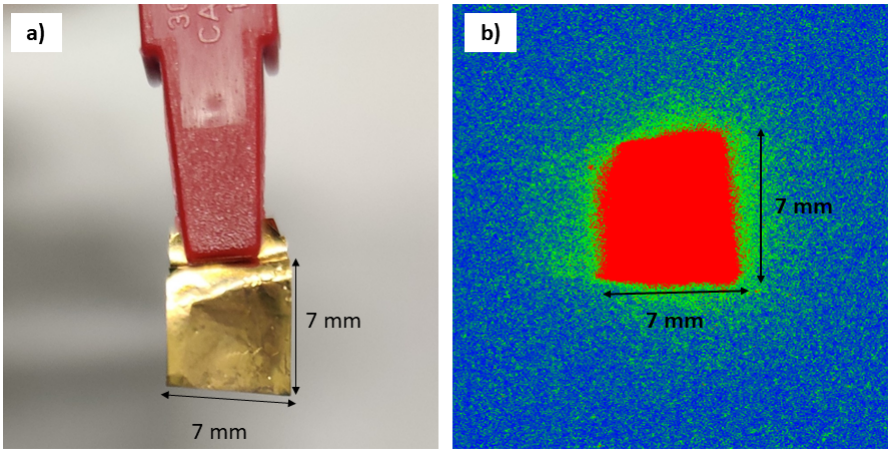

Figure 3.21: a) $^{51}\mathrm{Cr}$ source foil just after electrodeposition. b) Autoradiography of the source foil.

3.2.4.2 . Manganese-54

^{54}Mn decays by electron capture (99.9997(3) %) to the 834.855-keV excited level (2+) of ^{54}Cr and by very weak electron capture and beta plus transitions to the ground state (0+) of ^{54}Cr. The transition to the excited state is allowed while the transition by EC and β+ is a unique 2nd forbidden transition. ^{54}Cr has a half-life of 321.19 days, and the decay scheme is shown in Figure 3.22.

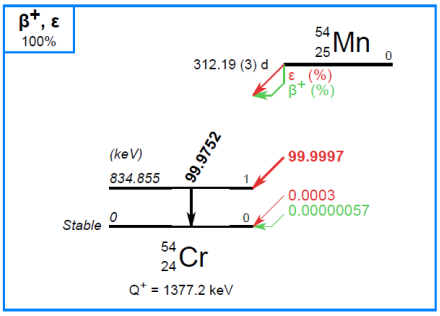

Figure 3.22: The decay scheme of ^{54}Mn [35].

This radionuclide was part of the EMPIR project MetroMMC, and the source was prepared by one of the partner institutes, the PTB Braunschweig, Germany. The recipe followed for this source preparation was adapted from reference [119]. The source was electroplated on 3 µm thick Au foil with dimensions of 15x15 mm^2. The foil was fixed with Kapton adhesive tape to a stainless-steel backing as mechanical support. The stainless steel disk has a diameter of 25 mm and a thickness of 0.4 mm, and the inner part of the backing with a diameter of 10 mm was the dedicated area for the radionuclide deposition. The setup contained a sintered glass filter between the cathode and anode (Platinum). Two different solutions were used in the anode and cathode compartments. This was done to reduce the deposition of manganese on the anode, which is possible due to the electrochemical properties of manganese. The composition details of the electrolytes are given in Table 3.3.

Table 3.3: Composition of the electrolyte for ^{54}Mn electrodeposition.

Ingredient	Amount
Catholyte	
HNO_3 with ^{54}Mn	1 ml with ~ 177 kBq ^{54}Mn (1.8.2021)
HNO_3 (pH = 4)	5 ml
Ultra pure ethanol	1.5 ml
Anolyte	
HNO_3 (pH = 2)	1.5 ml

The electrodeposition was performed at 70 °C with a voltage set to 30V and a duration of 2.5 h; the distance between the two electrodes was 8 mm. During the deposition, there was a decrease in the measured current value from I = 2 mA to practically I = 0 mA in the first hour of deposition. The resulting activity was 7.36 kBq, with a deposition efficiency of about 4.2 %. The autoradiography of the source foil (Figure 3.23 b) shows that most of the radioactivity was concentrated on the edge. As

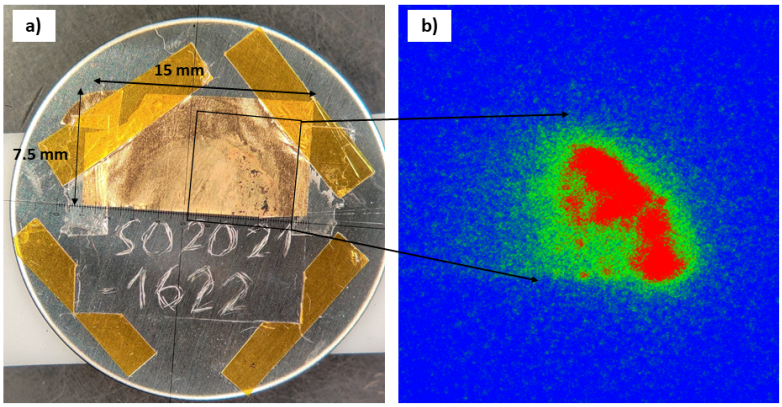

Figure 3.23: a) Electrodeposited $^{54}\mathrm{Mn}$ source foil. b) Autoradiography of the source foil.

can be seen in the photograph in Figure 3.19 a, only half of the actual source foil was shipped to LNHB; the other half stayed at PTB. The small blackened areas point towards an oxide layer rather than a metallic layer.

3.2.4.3 . Nickel-59

This is the second type of source prepared for EC measurement of $^{59}\mathrm{Ni}$. See subsection 3.2.1.3 for the first type of source preparation. The electroplating of nickel using aqueous electrolytes has a drawback in that they cause hydrogen to evolve and lead to its incorporation in the deposits. In the literature [121–123], it was reported that the crystallographic structure of the metallic deposits and their properties are altered due to the inclusion of hydrogen and hydroxides. To avoid this drawback, non-aqueous solvents like organic solvents are a better choice for nickel electroplating. The electrolyte for this plating was prepared using Dimethylsulfoxide (DMSO) organic solvent. $^{59}\mathrm{Ni}$ was electrodeposited onto the surface of a gold foil of 10x5 mm^2, with a thickness of 5 µm. The cathode was 99.99% Au foil in an in-house adapted two-electrode cell with platinum wire used as an anode (Figure 3.19).

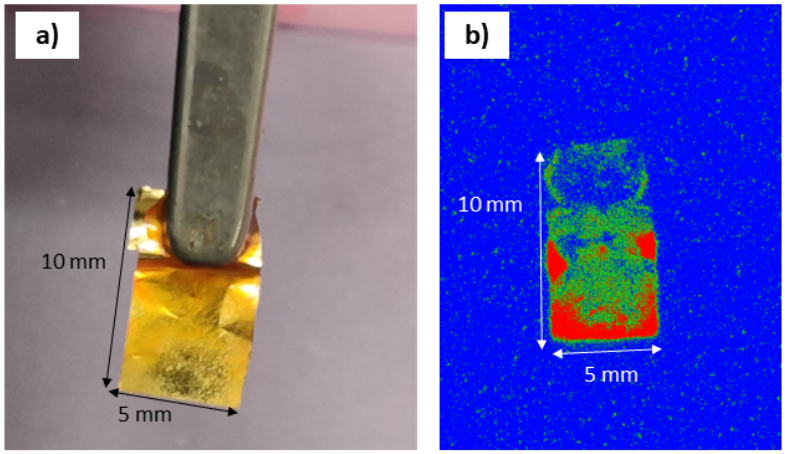

Figure 3.24: a) Electrodeposited $^{59}\mathrm{Ni}$ source foil. b) Autoradiography of the source foil.

The electrolyte was prepared using 5ml of DMSO with 100 µl of $1\ \mathrm{N\ HCl} + 0.1\ \mathrm{N\ HNO_3} + \mathrm{NiCl_2}$. The initial mass activity of the radioactive solution was 81 kBq/g in March 2021. The concentration of Ni was 28 µg/g in 10 mL of the radioactive solution obtained from NPL as a part of the EMPIR project MetroMMC. The electroplating was performed using a constant current source at I= 10 mA and V = 150 V for 20 mins. The deposit obtained was metallic and thin. The autoradiography of the source also pointed towards homogeneous deposits, as shown in Figure 3.24a. The final activity obtained on the source was 2.77 kBq. The activity required for the source was 10 Bq, and using the autoradiography (Figure 3.24b), a piece with the required activity was cut out.

3.2.5 . Ion Implantation

Ion implantation is the best way to deposit the source directly on one-half of the absorber. Since each radioactive nucleus is individually implanted directly into the absorber material, in principle, there can be no spectrum distortion due to the source. This technique has been used in the projects ECHo [124] and HOLMES [125] to attempt a measurement of the neutrino mass using $^{163}\mathrm{Ho}$. The implantation is performed by employing a mass separator to selectively ion-implant only the wanted nuclide into the fully optimized multi-pixel MMC with electroplated lower absorber halves. Subsequently, the $^{163}\mathrm{Ho}$ is enclosed by electroplating the top absorber halves on top of the source implants. This technique will be used for the first time for another radionuclide than $^{163}\mathrm{Ho}$ in the project PrimA-LTD to perform the high-precision electron capture decay spectrum measurement of $^{55}\mathrm{Fe}$. This process requires large-scale facilities and is, in general, a complex process. However, it is very promising from the results obtained using $^{163}\mathrm{Ho}$. The results showed no visible spectrum distortions and no enhanced background.

3.2.6 . Absorber preparation

For the DES technique, gold or silver (99.99 % or higher) is the preferred material for the absorber [97]. More details are given in Chapter 2, section 2.1. Once the geometry optimization by MC simulations is performed, the absorber and the source dimensions are fixed. To have the 4π geometry, the source carrier foil is sandwiched between the bottom and top absorber foils to enclose the sources; see Figure 3.3 for steps. Diffusion welding is then used to join each stack of foils. The diffusion welding press is shown in Figure 3.25.

The fabrication of the 4π source-absorber assemblies involved varying the temperature, pressure, and processing time. The radionuclide, the chemical composition of the source material, the absorber material, and other factors greatly influence the parameters needed to perform diffusion welding. If the radionuclide source is volatile, then diffusion welding cannot be performed, or it is performed at a temperature less than the melting point of the compound for a longer duration. Another technique, like cold-welding or just folding and pressing the absorber foil, like in the case of $^{14}\mathrm{C}$, can also be used in such cases. In most of the cases the diffusion welding is performed in a furnace at 400 °C, usually for 2 hours.

In the case of $^{125}\mathrm{I}$, direct diffusion welding of silver on gold is very difficult. The silver source foil could be sandwiched between two silver foils forming the absorber; silver has already successfully been used as an MMC absorber. In the case of $^{125}\mathrm{I}$, this is, however, not advisable. The decay of $^{125}\mathrm{I}$ is followed by a 35.5 keV gamma (see decay scheme in Figure 3.10) emission that must be absorbed with high efficiency for a meaningful EC measurement. The necessary large thickness of a silver absorber

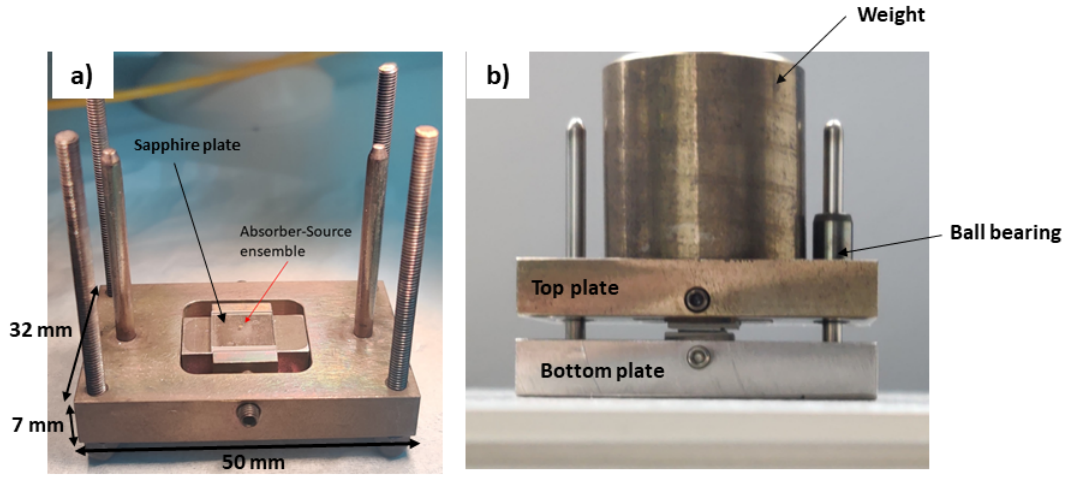

Figure 3.25: a)The complete absorber-source ensemble on the bottom plate of diffusion welding setup. b) Complete diffusion welding setup. The force applied during the diffusion welding process is defined by a weight piece placed on the top plate.

would imply a prohibitively large absorber heat capacity. To be able to bond the silver source foil to gold absorber foils, thin (about 10 µm) layers of $Au_{0.3}Ag_{0.7}$ (wt%) alloy were diffusion welded to the Au absorber foils before diffusion welding the source foil between the alloy layers. So the layer sequence is gold – gold-silver alloy – silver source foil – gold-silver alloy – gold.

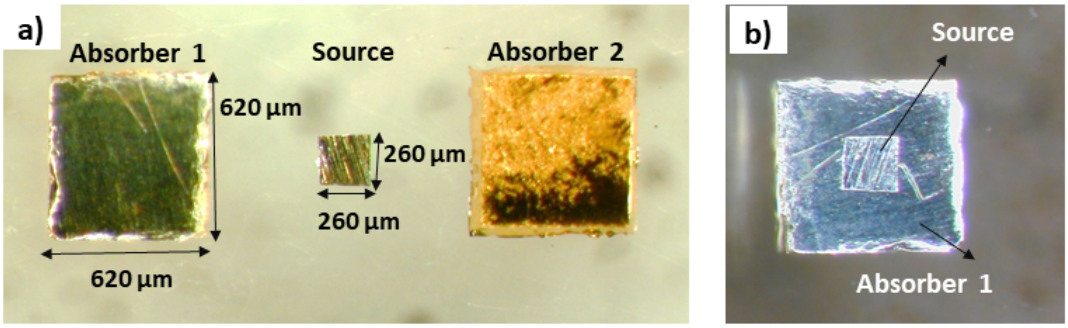

Figure 3.26: a) Lower absorber half with the gold-silver alloy layer on top (620 µm × 620 µm × 150 µm thickness); silver source foil with embedded 125I activity (260 µm × 260 µm × 6 µm thickness); upper absorber half with the gold layer on top (same dimensions as lower absorber half). b) Source foil placed on the lower absorber half.

The absorbers used for each radionuclide measured in this thesis are described in Table 3.4.

The absorbers were glued to the sensor using Stycast 1266 epoxy glue. The MMC chips and the SQUID chips were glued to the copper detector holder plate with GE 7031 varnish. The on-chip heat bath on the MMC chip was heat sunk to the copper detector holder with several 25 µm diameter gold

Table 3.4: Absorbers and sources Composition for each radionuclide

Radionuclide	Absorber Material	Absorber dimen-sions (μm^2)	Absorber thickness (µm)	Source carrier foil	Source type	Source di-mensions (μm^3)	Enclosure method
^{125}I	Au + AuAg alloy	620 x 620	2 x 149	Ag	Self deposition	260 x 260 x 6	Diffusion welding
^{14}C	Au	1000 x 1000	2 x 25	direct deposition on Au absorber	Drop deposition	-	Folded over and slightly pressed
^{54}Mn	Au	490 x 490	2 x 10	Au	Electro-plated	400 x 400 x 3	Diffusion welding
^{59}Ni (Electroplated)	Au	500 x 500	2 x 20	Au	Electro-plated	420 x 420 x 5	Diffusion welding
^{59}Ni (Drop-deposited)	Au	500 x 500	Absorber 1 = 10, Absorber 2 = 20	Au Nanofoam	Micro drop dispensing	400 x 400 x (6NPAu + 8Au)	Diffusion welding
^{51}Cr	Au	450 x 450	2 x 10	Au	Electro-plated	190 x 190 x 5	Diffusion welding

bonding wires. The detector module and the complete MMC chip with all its components are shown in Figure 3.27

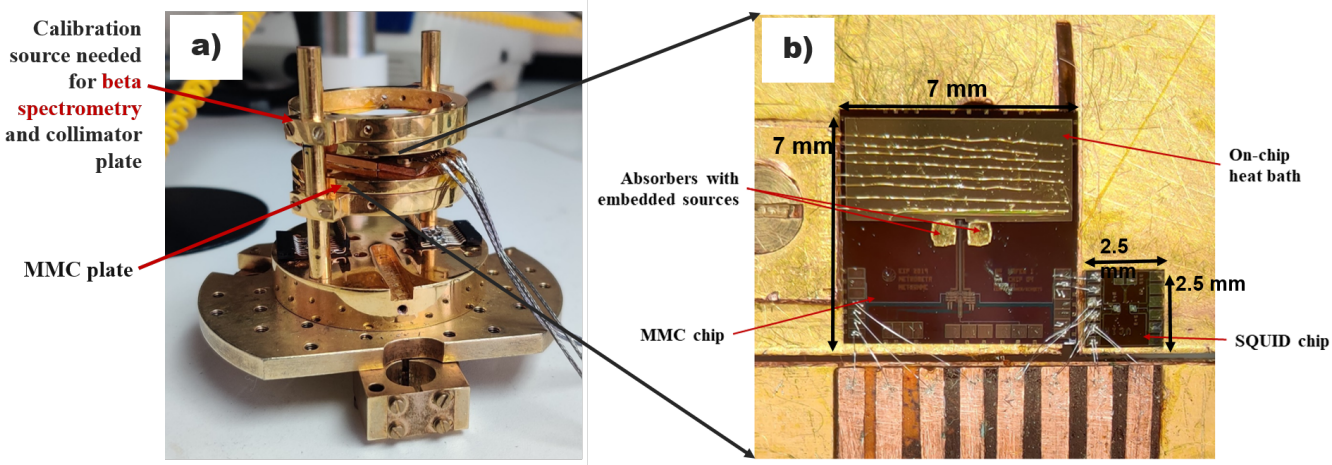

Figure 3.27: a) Detector module. b) Complete MMC detector setup.

3.3 . Cryogenics

The operating temperature of the MMCs is between 10-20 mK. At LNHB-MA, the low temperature is achieved by using a wet dilution refrigerator (DR). A dilution refrigerator is a type of cooling apparatus that provides continuous cooling in the low millikelvin range. The DR at LNHB can achieve the base temperature of 10 mK with a cooling power of 100 µW at 100 mK. The experiment space has dimensions of 290 mm in height with a diameter of 92 mm. Three detector modules can be simultaneously measured at the time of this thesis, each with an external radiation source, collimator, and individual magnetic shielding. In this thesis, a new detector setup was also designed to measure 10 detectors simultaneously to reach high statistics of the order 10^8 counts within a typical measurement duration of $\sim$ two weeks. The details of this setup are discussed later in the chapter 5. The details of the cryogenic system, along with its wiring, are described in this section.

3.3.1 . Dilution refrigerator

Liquid helium inside a cryostat is a method for achieving and maintaining low temperatures. However, even when pumping ^{4}He to low pressures, the lowest achievable temperature is about 1.2 K. A combination if ^{3}He and ^{4}He is used to achieve lower temperatures. A ^{3}He-^{4}He dilution refrigerator enables continuous cooling to temperatures as low as 2 mK. The dilution refrigerator uses a mixture of ^{3}He and ^{4}He isotopes to absorb and dissipate heat. It utilizes the mixing enthalpy when ^{3}He atoms migrate across a boundary from a phase of concentrated 3He to a phase of dilute ^{3}He and hence cools down [128–130]. The general schematic diagram of the "wet" dilution refrigerator, i. e. one that uses liquid helium to precool to 4.2K, is shown in Figure 3.28. Recent dilution refrigerators mostly use pulse tubes to precool to ~ 3.5 K and are referred to as "dry" dilution refrigerators.

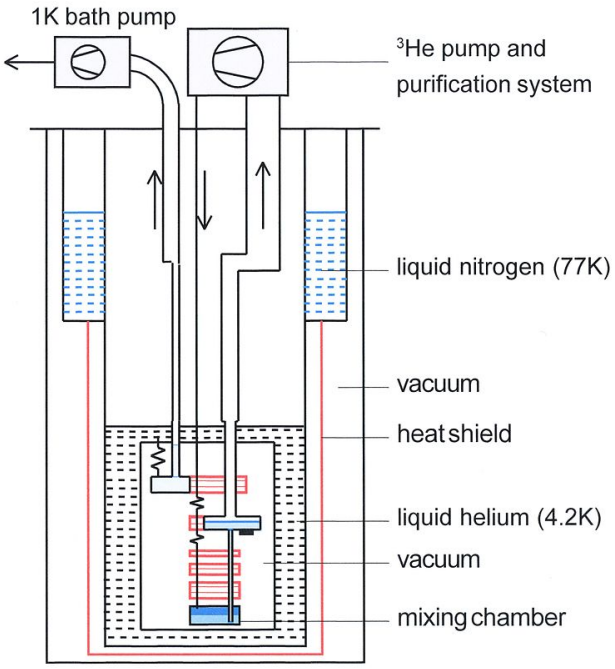

Figure 3.28: Schematic diagram of a typical wet dilution refrigerator.

There are 4 components of the dilution unit: 1 K pot, still, continuous and discrete heat exchangers, and mixing chamber. The dilution unit is enclosed in an inner vacuum chamber (IVC); the vacuum is necessary to thermally isolate the dilution unit (DU) from the warmer surroundings. Before mixture condensation can start, the dilution unit must be cooled from 300 K to 4 K. To achieve this, the IVC is immersed first in liquid nitrogen (77 K) and subsequently in liquid helium (4.2 K). During the precooling phase, a small amount of helium exchange gas is introduced into the IVC to evacuate the heat from the DU to the IVC walls via convection. Before further cooling, the exchange gas must be pumped out. At LNHB, we frequently use $^3\mathrm{He}$ as exchange gas, its advantage being that it is being pumped much more efficiently. Although $^3\mathrm{He}$ is in principle very expensive, given the very small amount of exchange gas required for efficient convection, its cost for a cooldown of the refrigerator is negligible compared to the cost of the liquid helium used to precool and maintain the IVC at 4.2 K.

Condensation of the $^3\mathrm{He}$-$^4\mathrm{He}$ mixture is performed in many wet dilution refrigerators by passing it through a 1K pot, a small cylinder filled with liquid helium from the dewar through a capillary, and cooled to 1.2 K by continuously pumping on the liquid surface. In the LNHB refrigerator, the $^3\mathrm{He}$-$^4\mathrm{He}$ mixture is condensed by driving it through a series of Joule-Thomson expansion stages. It additionally has a 1K pot that is not necessary for the operation of the dilution but serves to heat sink the cables coming from higher temperature stages and, if necessary, to cool preamplification SQUIDs below 4 K.

The process of phase separation needs a temperature of 0.86 K, which is the tricritical point. To reach this temperature, the mixing chamber is connected via a capillary with a secondary chamber called still. The amount of mixture condensed into the refrigerator is adjusted such that its surface

is lying in the still volume. Pumping on the surface of the mixture permits cooling to well below 0.86 K. The mixture descending towards the mixing chamber is running through the still and thereby cooled to below 0.86 K, thus leading to phase separation and enabling the dilution process to start. To maintain a dynamic equilibrium, the operating system removes $^3\mathrm{He}$ from the dilute phase and returns it to the concentrated phase. This is accomplished by pumping $^3\mathrm{He}$ away from the still's liquid surface at a temperature where its vapor pressure is orders of magnitude greater than that of $^4\mathrm{He}$. As a result, the concentration of $^3\mathrm{He}$ in the dilute phase of the mixture decreases, forcing a flow of $^3\mathrm{He}$ through the phase boundary driven by osmotic pressure. The time taken by this whole process to reach the base temperature is somewhere between 1.5 and 2 days [131].

3.3.2 . Wiring and Connections

The detectors are placed in the experimental space shown in Figure 3.29, below the mixing chamber. The detector holder and the pieces fixing it to the mixing chamber plate are made of copper to ensure efficient cooling of the detectors. It is crucial to maintain the minimum heat load inside the cryostat. To lessen the heat load on the mixing chamber and restrict the heat exchanges with the outside, all connections to the room-temperature equipment are heat sunk at various temperatures throughout the cryostat.

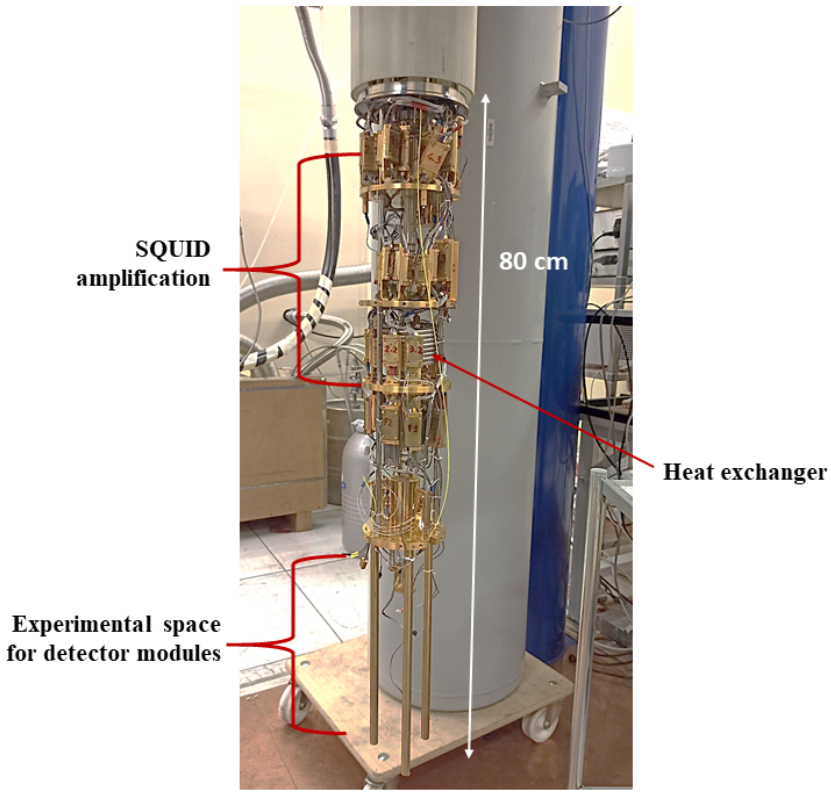

Figure 3.29: The IVC part and the experimental space in dilution refrigerator setup at the LNHB.

The wires are chosen to be of a low thermal conductivity material. Unfortunately, excellent electri-

cal conductivity is often accompanied by high thermal conductivity. Superconductors are one exception to this rule, as they exhibit negligible thermal conductivity and no electrical resistance. Hence, the heat load is reduced on the detector stage using superconducting wires below 4.2 K. Between 300 K and 4.2 K, brass wires have been chosen as they have sufficiently low thermal conductance but lower ohmic resistivity than e.g. manganin, another commonly used material for cables in cryogenics. Wires inside the cryostat can also expose SQUIDs to electromagnetic perturbation picked up outside the cryostat, so, they are twisted and shielded in a CuNi ground braid. The single-stage SQUID sensor from Supracon called VC1A was used in this thesis. To control their operating parameters, i.e., the bias current and feedback resistance, the software provided by Magnicon (written in Labview) is used. Two TRMC2 resistance bridges are used to read the thermometers at different temperature levels of the cryostat.

3.3.3 . Vibrations and noise

The wires also have an electrical capacitance and inductance that fluctuate with vibrations and can cause stray currents. MMCs are not particularly sensitive to vibrations as a noise source. However, e.g. vibrating bonding wires between the MMC and SQUID chips can cause fluctuating inductance and hence induce vibrational noise on the flux injected by the input coil to the SQUID. The cryostat is hanging from a plywood plate to reduce vibrations. This is based on sand-supported compressed air shock absorbers. Steel pylons are used as support for everything. The injection and pumping pipes for the ^{3}He-^{4}He mixture and the pumping pipe for the 1 K pot could transmit vibrations from the pumping bench to the cryostat. These pipes are partially buried in a sandpit to disconnect the head of the cryostat from the pumping bench. The installation is shown in Figure 3.30.

Figure 3.30: Installation of cryostat at LNHB.

3.3.4 . Magnetic field generation in the MMC

The magnetic field required to magnetize the paramagnetic sensor is mostly generated when the dilution unit (DU) has reached 4.2 K. The steps are illustrated in the Figure 3.31. In step a) a heater current is injected to open the heat switch while running the field current through the meander circuit, in step b) the interruption of the heater current closes the heat switch, and in step c) the field current is frozen into the closed superconducting circuit formed by the meander coils. However, there is no way of checking whether we have succeeded in freezing the current at this stage. We can only be sure once we reach mK temperatures, and it is possible to repeat the injection step at low temperatures, but there is the risk of heating the cryostat to a few hundred mK.

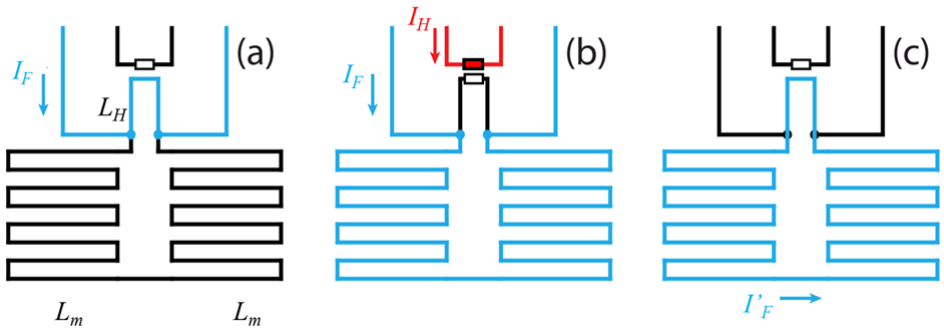

Figure 3.31: Magnetic field generation in the MMC.

In Figure 3.31, L_m is the inductance of the meanders, and L_h is the inductance of the heather path. I_f is the field current and I'_f is the persistent current and its value is $I'_f = I_f \frac{2L_m}{2L_m+L_h}$.

3.4 . Data Acquisition and analysis

The SQUID electronics comprises an auto-reset mode: when the baseline crosses a threshold chosen by the operator, an internal reset is triggered in SQUID electronics, bringing the SQUID back to its initial operating point. The SQUID output data is acquired continuously, typically for two to three weeks at 10-20 mK, to have sufficient statistics for the decay spectrum. The analog output voltage from the Magnicon SQUID electronics is amplified and filtered using a low-pass or band-pass filter with an SR560 amplifier from Stanford Research Systems. The signal can be filtered with a high pass to reduce the fluctuations in the baseline. The low pass filter is set to Nyquist frequency (less than half the sampling frequency) to prevent aliasing in the input signal. The cut-off frequency is set high enough to avoid filtering the pulse's decay time, which might degrade resolution and lead to strong undershoots. The output from the SR560 amplifier is connected to a PCI acquisition card P25M from Innovative Integration, which digitizes the signal.

The P25M acquisition card has two channels that are scanned using 16-bit resolution and have a maximum 2.5 MHz sampling frequency. In this thesis, the data was recorded at two sampling frequencies: 100 kHz and 250 kHz. The recording at the higher sampling frequency (250 kHz) necessitates storing and analyzing excessively vast amounts of data, so in most cases, 100 kHz was chosen. When

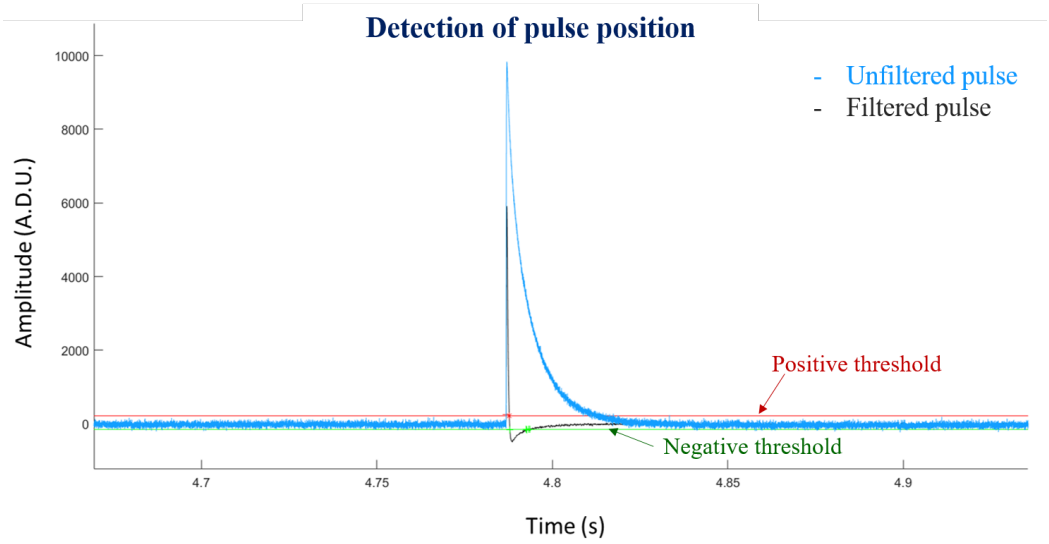

Figure 3.32: Detection of the position of the pulses in the record (blue plot is unfiltered pulses and black plot is filtered pulses).

the baseline crosses a threshold, an internal reset happens on SQUID electronics. The data is stored continuously (untriggered) on a solid-state device. All electronics are linked to the ground to prevent ground loops.

The obtained data is analyzed offline using digital signal processing routines written in MATLAB. By analyzing the signal in the time or frequency domain, it is possible to determine the amplitude value of the pulses, proportional to the total energy deposited in the absorber. In addition, parametrization in the frequency domain can suppress contributions at some harmonics where the noise spectra are of significant amplitude. The main steps followed by these routines are listed below, and their objective is to obtain an energy spectrum with the best possible energy resolution and no spectrum distortion.

- Detection of the position of the pulses by triggering on the continuous data stream

By employing two trigger thresholds to trigger the pulses of opposite sign from the two sensors of each gradiometric double meander circuit, the time position of the pulses is determined (see Figure 3.32). With cut-off frequencies generally between 400 and 700 Hz, high-order Butterworth band-pass filters filter the streams before applying the thresholds. Throughout the recording, positive and negative thresholds are established with constant values. Each signal's time stamps for crossing the thresholds, both upwards and downwards, are recorded and given the names t_{start} and t_{stop}, respectively. The polarity of the signal, which indicates which threshold is triggered, "+1" for positive and "-1" for negative and "0" if the signal is saturated, is kept as a third parameter in the time stamps binary file.

- Application of extended dead-time window

A minimum amount of time is necessary after detecting a pulse before detecting another event; else, a pileup will occur. The purpose of the dead-time function is to suppress the time stamps associated

with the pileup on the pulse baseline or the timestamps from artifact signals such as noise triggering, undershoots, etc. An extended dead-time function is applied to the timestamps after all the pulse timestamps have been recorded. For all the t_{start} timestamps, the dead-time window duration T_{Dead} is given as $T_{\text{Dead}} = F_{\text{Dead}} \times (t_{\text{stop}} - t_{\text{start}})$. F_{Dead} must be greater than the ratio between the duration of raw pulses and a pulse that has undergone bandpass filtering. Instead of a conventional fixed dead-time window, an extendable dead-time window with a length proportional to pulse duration minimizes the dead-time percentage. All signals with t_{starts} that fall into a dead-time window are suppressed, and the initial dead time is of the suppressed pulse (hence the name extendable dead time). The applied extendable dead time is also used to calculate the live acquisition time. The whole acquisition time minus the total dead time equals the live acquisition time.

- Construction of the average pulse [$M(t)$] and its noise spectrum [$S(f)$]

As explained in the introduction of section 3.4, two methods called time domain (TD) and frequency domain (FD) are used to determine the pulse energies. Both methods require the construction of a template pulse, and the mean noise power spectral density is needed for the frequency domain (FD). The construction of the template pulse is done by averaging about 100 pulses. In the starting, the first five pulses are selected just by observing them and making sure that the select pulses have a low baseline RMS value and a clean shape without pile-up to make an average pulse. After this selection, the remaining pulses are chosen automatically from an upper limit value on the standard deviation of the pulse baseline and the χ^2 (chi-square) between the template and detected pulse fit. The number of samples of the pulse template is a power of two of the signals, which is more convenient for the Fast Fourier Transform (FFT) of the frequency domain. The first half of the template pulse is the baseline, and the second half is the pulse rise and the main part of the pulse decay. The mean noise power spectral density is the mean of 8192 FFTs of the chosen clean baseline, with low standard deviations and a mean value near zero.

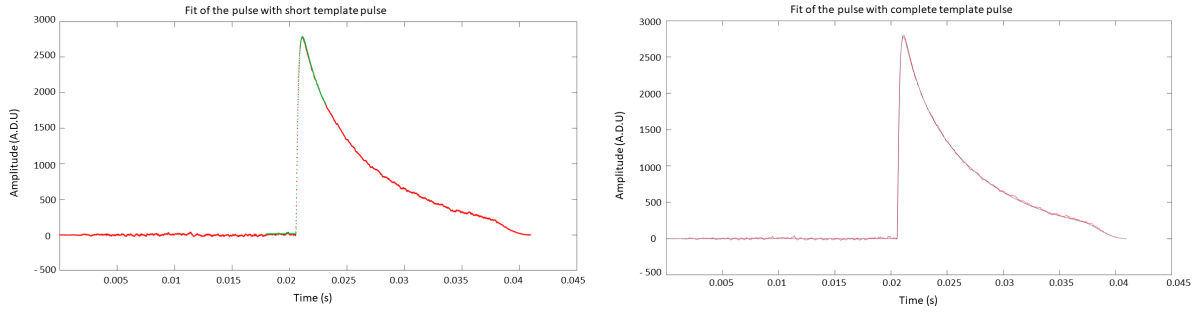

Figure 3.33: Fit of the pulse with short and complete template pulse.

In time domain (TD), a template pulse $M\,(t - t_{start})$ is linearly fitted to the pulses detected $m\,(t - t_{start})$ using equation 3.1. In this equation, A_{TD} is the pulse energy, and $B_{TD}$is the baseline level.

$$m\,(t - t_{start}) = A_{TD}.M\,(t) + B_{TD} \tag{3.1}$$

In the frequency domain (FD), the optimal filtering method is implied. FD is preferred if the detected pulses have the same shape and the noise doesn't vary over time. To estimate the pulse amplitude (A_{FD}) equation 3.2 is used, where S_n^* is the Fast Fourier Transform (FFT) of the pulse template normalized to 1 in TD, J is the noise power spectral density and $\nu_n$is the FFT of the detected pulse.

$$A_{FD} = \frac{\sum_{n=-\frac{N}{2}}^{\frac{N}{2}-1} \frac{\widetilde{S_n^*}\nu_n}{J(f_n)}}{\sum_{n=-\frac{N}{2}}^{\frac{N}{2}-1} \frac{|\widetilde{S_n^*}|^2}{J(f_n)}} \tag{3.2}$$

- Determination of pulse energies

Each pulse whose t_{start} falls in the live time is analyzed to determine the pulse energies. A low pass filter with a cutoff frequency of f_e/10 pre-filters the pulse. This ensures enough samples in the leading edge since an insufficient number of sampled data points will affect the energy resolution with optimal filtering. The baseline level before the pulse is measured and removed from the pulse. The amplitude is determined using the two methods given in the previous step. In TD, the detected pulses are fitted using two different lengths. One template has the entire length of the template pulse, and the other has a reduced length of about 1 ms to 2 ms. Because it reduces the contribution of low-frequency noise, using a reduced template length yields a better estimation of the parameter A_{TD} in the equation 3.1. During this step, some other essential parameters are also measured, like the pulse area and the maximum of the pulse, the 10% to 90% rise time along with the t_{max} timestamps of pulse maximum, the pulse baseline level, and its standard deviation.

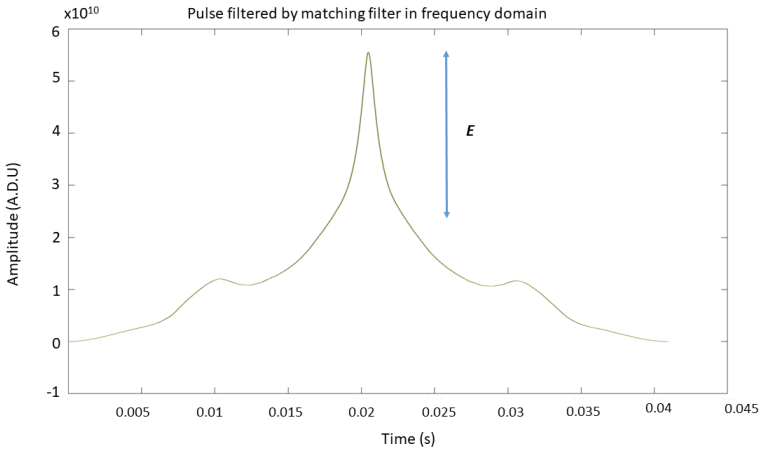

Figure 3.34: Pulse after filtering in frequency domain.

- The correction of the temperature drift

The temperature of the detector stage is not regulated and is determined by the cryostat base temperature. Some parts of the recording exhibit significant temperature instability, primarily due to

the filling of the cryostat with liquid helium, and the pulses observed during these periods are eliminated. But also, in continuous operation, the base temperature is not perfectly stable, and the pulse amplitude is prone to temperature drift, which can be corrected in two ways.

The first method uses the pulse height fluctuation at an energy level as a reference. These pulse heights can, for example, be provided by one of the calibration source's X-ray or gamma-ray lines or electron capture lines. One of the lines with the highest statistics is used to get a good sampling of the temperature drift. Also, a line with relatively high energy is used compared to the rest of the spectrum to have excellent sensitivity to the temperature drift. A spline fit function $f_{amp}(t)$ is derived as a function of time from these amplitudes, and all of the amplitudes A are corrected by $A_{corr} = A/f_{amp}(t_{start})$.

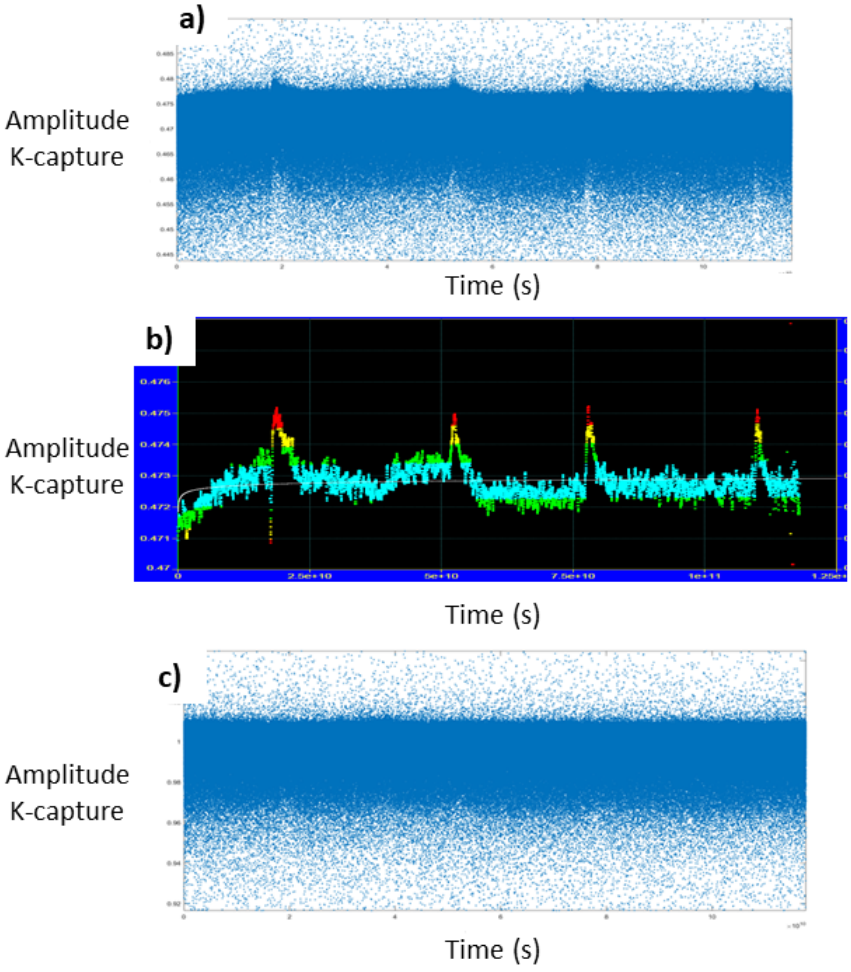

Figure 3.35: The correction of the temperature drift in the K-capture line in the plot of amplitude as a function of time by averaging the pulse height function of the K shell line. a) before correction b) Average fitting of pulse heights c) after correction.

The second method is to use the baseline level of each raw pulse. The baseline level indicates the

detector's relative temperature. The plot of pulse amplitudes as a function of pulse baseline level for a particular energy yields a linear relationship used to correct the correlation amplitude-vs-baseline level and temperature drift.

- Rejection of the pile-ups on the pulse decays

By using the extendable dead-time, pile-up is removed on the pulse baseline, but the pile-up on the pulse decay is not removed. To remove the pile-up on the pulse decay, the amplitude as a function of χ_{comp} is plotted. χ_{comp} corresponds to the χ^2 of the fit between pulse and the full pulse template. The pulses with large χ_{comp} value are rejected (see Figure 3.36 for reference) as they are pulses whose shape deviates from the template shape. The deviation is mostly due to the pile-up on the pulse decay. Hence, by removing these large χ_{comp} value pulses, the pile-ups on pulse decay are removed. Generally, the χ^2 is dependent on the pulse energy and this dependence needs to be taken into account. The χ_{comp}-vs-amplitude plot is fitted using a quadratic function $\chi_{fit} = a\chi.A^2 + b\chi$, χ_{fit} is the mean value of χ_{comp} at a given amplitude. Hence the χ^2 limit to reject the pile-up is $\chi_{limit} = A.\chi_{fit}$.

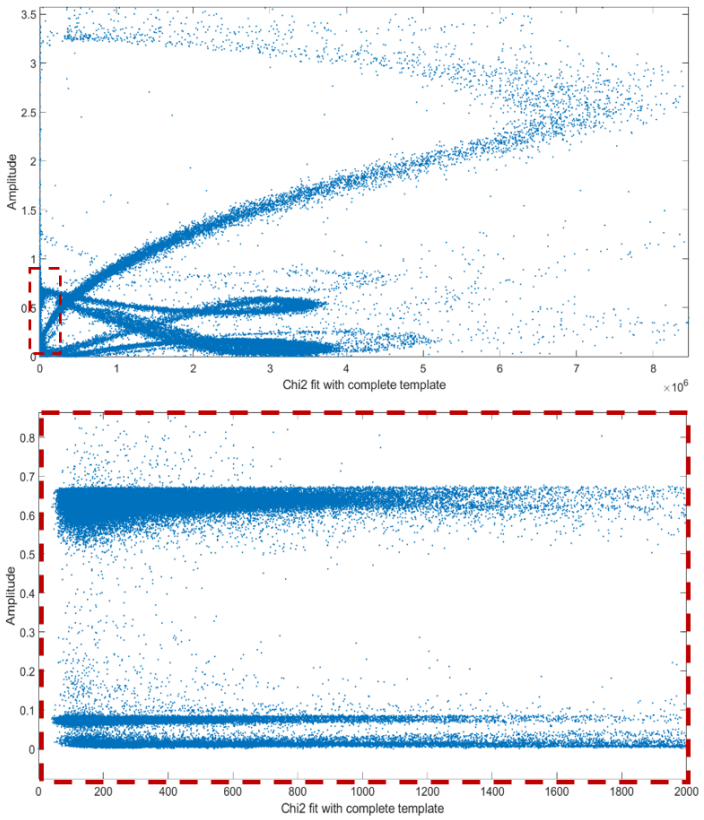

Figure 3.36: Plot of χ^2 from the complete fit template and amplitude before the rejection of pile-ups on the pulse decay (top plot) and the red square shows the pulses with small χ^2 values that are selected (zoomed in bottom plot) .

- And finally, the energy spectrum is constructed. There are different methods of determining the amplitudes, with each having their advantages and disadvantages. The amplitudes can be given by: -The maximum of the pulse, the area of the pulse, the adjustment factor A of an averaged pulse ($M(t)$) on the measured pulse ($m(t)$) by minimizing the chi-square in $m(t)$ and $AxM(t)$ and the maximum of the pulse after matched filtering. Also, the spectrum obtained is calibrated using the known energy line.

4 - Measurement results and analysis

This chapter analyzes and discusses the results from the measurements performed for fractional electron capture probability ratios and beta spectrum shape. The radionuclides analyzed for the EC spectrum are $^{125}\mathrm{I}$, $^{54}\mathrm{Mn}$, $^{59}\mathrm{Ni}$, and $^{14}\mathrm{C}$ for the beta spectrum.

In a 4π measurement of an electron capture (EC) nuclide, the source is embedded between two absorber halves. In the ideal case, a single line is observed in the energy spectrum for each electron shell on which the capture occurs, corresponding to the captured electron's binding energy. This is because the detector sums the total energy emitted in a cascade of Auger electrons and/or X-rays for each individual decay. The lines have a natural line shape, and individual sub-shell lines should be observable for shells higher than the K shell. Due to multi-hole states, higher-shell lines frequently feature additional satellite structures. This has the potential to complicate spectrum analysis in general. However, the detector performance and statistics do not reveal most of these structures in most circumstances.

Additional complications can arise from various phenomena related to the absorber/source or detector properties, such as peak tailing due to incomplete thermalization of the energy lost by electrons in the source material, escape peaks, or Compton background due to gamma photons underlying the line spectrum if a gamma transition follows the EC transition. The first and sometimes challenging step in analyzing a 4π EC measurement is identifying all features present in the spectrum. If the lines are sufficiently separated, and significant background is absent, the populations from the different electron shells can be quantified by counting the events in a defined energy region. However, usually peak fitting is applied to quantify the content of each line.

4.1 . Iodine-125

Iodine-125 is of particular interest due to its role in cancer therapy [133, 134]. It is a very significant candidate for interstitial brachytherapy, as it is a very localized radiation source due to it being an EC nucleide. Auger electrons are emitted after electron capture or internal conversion. In tissues, their energy is deposited over nanometer to micrometer distances, resulting in high-yield linear energy transfer. The EC nucleides are the perfect choice for cancer treatment, where they need to be radiated extremely close to cancer cells [135–137]. Use in nuclear medicine requires explicit and precise knowledge of decay data, such as half-life, radiation energies, and emission probabilities. The measured data can be used to revise recommended dose values for minimum damage to healthy tissues. $^{125}\mathrm{I}$ decays 100% by electron capture through the first excited state of $^{125}\mathrm{Te}$ into its ground state with 35.49 keV gamma deexcitation energy. The gamma transition is highly converted: 93.37% of the gamma deexcitation emits conversion electrons, and only 6.63% emits gamma photons. The spin and parity of the ground state of $^{125}\mathrm{I}$ are $\frac{5}{2}^{+}$ and that of the first excited state of $^{125}\mathrm{Te}$ is $\frac{3}{2}^{+}$, and spin – parity selection rules state this transition to be allowed. The decay scheme and the binding energies of the electrons are shown in Figure 4.1.

In our $^{125}\mathrm{I}$ measurement, due to the 4π geometry, the binding energy of the captured electron

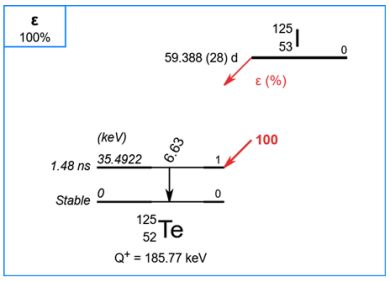

Electron shell	Energy (keV)
K	31.8138
L	4.9392
M	1.0060
N	0.1683
O	0.0116

Figure 4.1: ^{125}I decay scheme and the binding energies of the electrons [35].

released in the atomic rearrangement was summed with the daughter nucleus' 35.49 keV gamma de-excitation energy, such that all events, even the very low energy N capture atomic rearrangement events, occur at energies larger than 35.49 keV. A peak corresponding to capture from each electron shell (K, L, M, and N) is observed in the DES spectrum shown in linear Y scale in Figure 4.2 and in log Y scale in 4.3. The log Y scale gives more details of the decay spectrum.

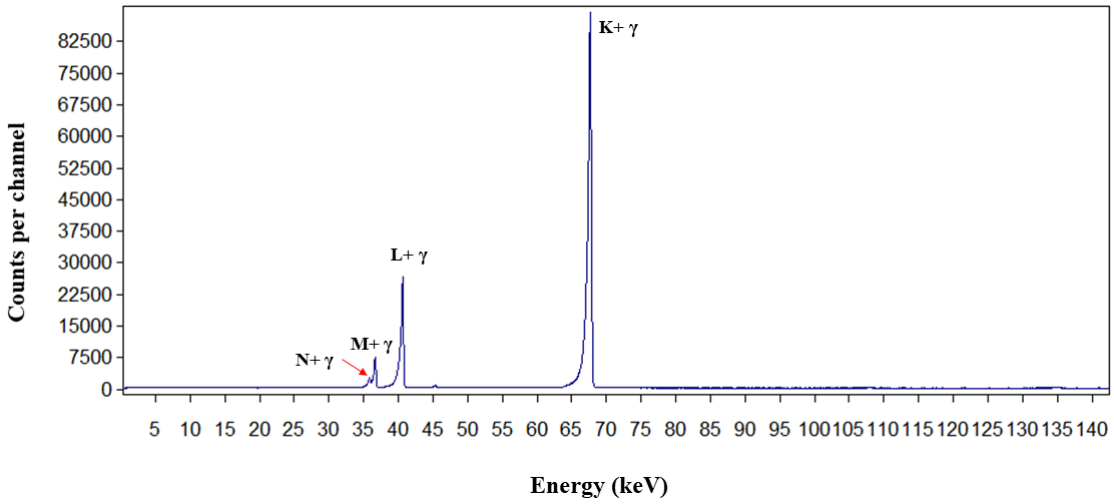

Figure 4.2: The energy spectrum of ^{125}I in linear Y scale.

The pulses had 10-90% rise times of ~337 µs, and the pulse decay follows an exponential, giving a 1/e decay time of 9.5 ms. The decay time in conjunction with 4 Bq source activity results in a small fraction of pile-up events both for K and L capture as seen in Figure 4.3. An extendable dead time summing up to 0.20% was applied to eliminate pulses with a non-constant baseline under the assumption that the pulse was rising on the decay of a preceding pulse. An optimal filter was used to determine the pulse energy. In the plot of χ^2 (obtained from the template fit of the actual events) vs pulse height, pile-up on the decay, and other spurious events were eliminated, and cuts were made on the value of the root mean square of the pulse baseline. Finally, temperature drift was corrected in the plot of pulse height vs. time (see Figure 3.35 for reference) by fitting the pulse heights of the K shell line as an average height function. The final spectrum contains about 3×10^6 EC events after

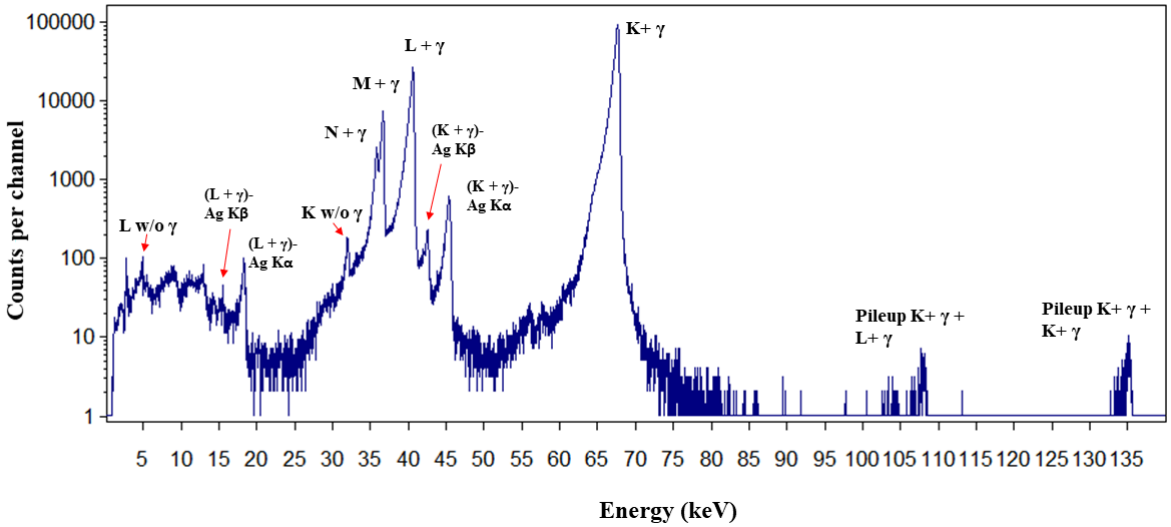

Figure 4.3: The energy spectrum of ^{125}I in log Y scale.

filtering, cuts, and corrections.

In the energy spectrum, three different population types were observed, first one are the full decay energy lines, second the escape peaks, and third the pile-up.In all peaks, probably due to the loss of a portion of the energy of Auger electrons in the source material in a non-thermal form, a low-energy tail is observed. These are described in detail below:

- Full decay energy peaks

In the Figure 4.3, the K, L, M, and N capture peaks are well distinguished and separated from the noise triggering as they occur at energies equal to the electron binding energy plus 35.49 keV from the gamma de-excitation energy. As the energy of this low-energy gamma transition is also detected with high efficiency, the energy of the gamma transition is summed with the energy of the atomic rearrangement process. There are two populations where the gamma photons escape from the absorber, these are titled as K w/o γ and L w/o γ. See Table 4.1 for reference.

Table 4.1: The energy of the peaks observed in the spectrum.

Peak	Energy (keV)
K+γ	67.30
L+γ	40.43
M+γ	36.50
N+γ	35.66
K w/o γ	31.81
L w/o γ	4.94
γ	35.49

- Escape peaks

For the two populations where a gamma photon (35.49 keV) has escaped, K w/o γ contains 0.49% of events with respect to the principal K line, and for L w/o γ it is 0.87% with respect to the principal L capture events. The two populations at $\sim$ 8 keV and $\sim$ 13 keV, respectively, that are not labeled in the spectrum are due either to the escape of two $^{125}\mathrm{Te}$ K X-ray photons following a single K capture or to a single $^{125}\mathrm{Te}$ K X-ray escape after an L capture. These additional K X-ray emissions follow the emission of conversion electrons from the K shell during the gamma transition. The O capture (11 eV) events are few in number to be separated from the N line and should be hidden in the low energy tail of the latter. Escape peaks due to Ag X K_α and K_β photons escaping from the absorber are visible for both the K and L capture lines. The peaks for Ag are observed as the inner layer of the absorber is AgAu alloy, and as the source is drop deposited on Ag and formed AgI and the kneading process was performed to break down the AgI layer and to incorporate AgI into Ag (see the section on source preparation in chapter 2 for more details).

Likewise, there should be a population of gammas summed only with low-energy Auger electrons from the events where a $^{125}\mathrm{Te}$ K X-ray from the daughter atom escapes from the absorber, but this population is invisible in the spectrum since it coincides with the M + γ line (for an escaping $^{125}\mathrm{Te}$ Kα photon) and N + γ line (for an escaping $^{125}\mathrm{Te}$ Kβ photon). See Table 4.2 for reference for energy values. The effect of Te K X-ray escape coinciding with the M and N peaks must be smaller than the gamma photon escape probability giving < 1% escape of Te K X-rays. Therefore, the M and N capture probabilities are probably slightly overestimated. This effect is difficult to quantify since no full theoretical description of the complex atomic rearrangement process is available. We tried to quantify this effect by using a Monte Carlo simulated spectrum, but it did not match the obtained experimental spectrum.

Table 4.2: Energies and origin of escape peaks in the spectrum.

Elements	X-ray Energies (keV)	Ag escape peaks	Energy (keV)	Te escape peaks	Energy (keV)
Ag K_α	22.16	K_α from K+γ	45.17	K_α from K+γ	39.83
Ag K_β	24.94	K_β from K+γ	42.36	K_β from K+γ	36.31
Te K_α	27.47	K_α from L+γ	18.27	K_α from L+γ	12.96
Te K_β	30.99	K_β from L+γ	15.49	K_β from L+γ	9.44

- Pile-up

In the Figure 4.3, a small percentage of unresolved pileup (< 0.02% for K+γ) results in the tail on the right side of the peaks. The two populations labeled as pile-up K+K and K+L correspond to 0.005%

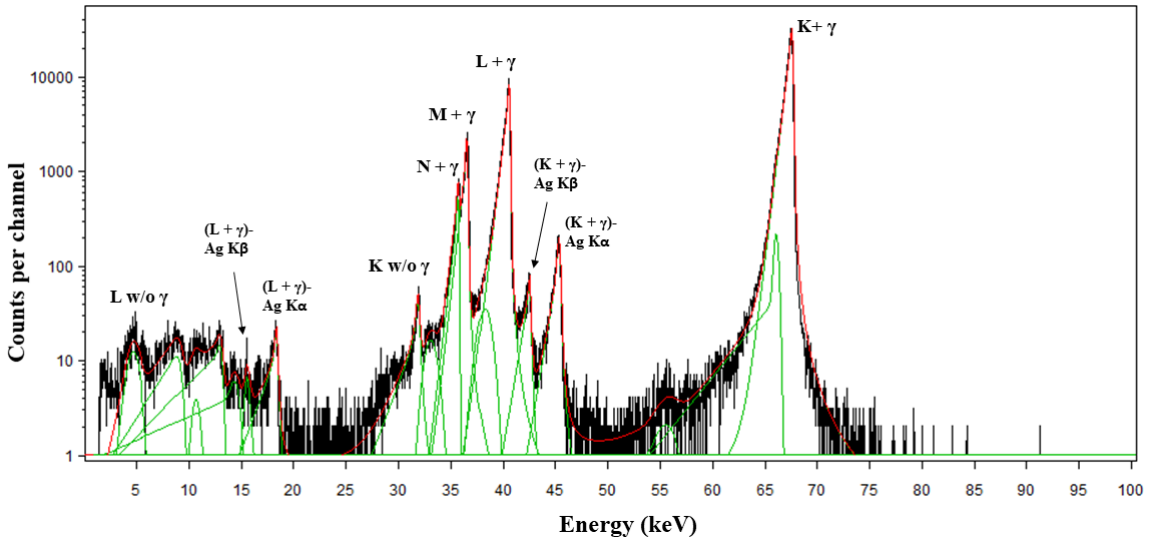

Figure 4.4: Spectrum processing of ^{125}I.

for pile-up K+K and 0.004% for pile-up K+L events. They were accounted for as 2 K capture events for each K+K pileup event and as 1 k and 1 L captures for each K+L pileup event.

- Fractional electron capture ratios

The fractional electron capture probabilities correspond to the ratio of peak areas. The peak area of each capture was determined using the spectrum fitting tool COLEGRAM developed at LNHB. While calculating the peak area for the capture lines, the escape peaks including those with gamma escape ("w/o gamma" in Figure 4.3) were added to their respective origin shells, as well as the K+K and K+L pileup populations. Because of the physics involved in 4π detection using a cryogenic detector and the decay physics, the shapes of the peaks are not consistent with common peak shapes and cannot be reproduced by any single available peak shape function, either Gaussian or Voigt or any other.

So different fits using Gaussian and Voigt functions with or without tails were performed for three different template lengths (see Figure 4.4 for reference to one of such fittings). No set of individual lines could perfectly fit the whole peak population. Some arbitrary peaks were also placed to fit the low and high-energy tails. The peak area for each of the populations corresponds to the sum of the individual fit functions. Additionally, more or less stringent cuts in the χ^2 vs. pulse height plots for pile-up rejection were applied, leading to slight differences in the resulting spectrum and peak areas. The resulting peak areas from the combinations of cuts and fits of the spectra were averaged to calculate the fractional capture probability ratios. The obtained values from the measurement are given in Table 4.3.

The reported uncertainties include the contribution of statistical uncertainty u(stat) and systematic uncertainty u(sys). systematic uncertainty is an error resulting from the scatter of the peak areas obtained with the different combinations of cuts and fits. It is the relative deviation of the fractional EC ratio divided by the average of EC ratio. The total uncertainty was calculated using the following formula:

Table 4.3: Fractional EC probabilities ratios of ^{125}I.

Fractional EC probabilities	Experimental	BetaShape [17]	Literature
$P_{\mathrm{L}}/P_{\mathrm{K}}$	0.2388 (26)	0.1947 (29)	0.23 (3) [144]
$P_{\mathrm{M}}/P_{\mathrm{K}}$	0.0575 (16)	0.0447 (22)	-
$P_{\mathrm{N}}/P_{\mathrm{K}}$	0.0156 (21)	0.0101 (10)	-

$$U(\frac{P_L}{P_K}) = \frac{P_L}{P_K} \times \sqrt{(u(stat))^2 + (u(sys))^2}$$

Previous measurements of fractional EC ratios of ^{125}I mentioned in the literature were performed either by embedding the radionuclide in NaI scintillation detectors [138, 139, 141] or by using an external source with an HPGe (High-Purity Germanium) detector [140]. These measurements provided the value for $P_{\mathrm{L+M+...}}/P_{\mathrm{K}}$ (L+M+.. corresponds to the summing peaks associated with electron capture from the L, M, or higher shells, followed by nuclear gamma-ray or internal conversion electrons, in detectors that cannot separate the individual populations) rather than the individual ratios $P_{\mathrm{L}}/P_{\mathrm{K}}$, $P_{\mathrm{M}}/P_{\mathrm{L}}$. In the reference [138] the authors measured $P_{\mathrm{L+M+N}}/P_{\mathrm{K}}$ using an ^{125}I source as a constituent of the NaI-lattice in NaI(Tl) scintillation crystals by measuring the intensity ratio of peaks A and B. The peak A was the summing peak of the 35.4 keV transition of ^{125}Te and the Te K-binding energy and peak B was the summing peak of the 35.4 keV transition and Te L and M-binding energies. The authors in [139] measured L+M+.../K electron capture ratio using the well-type NaI(Tl) internal source scintillation spectrometer technique. They observed two peaks at 67 keV and 39 keV in the measured pulse-height spectrum. The first peak was due to the summation of the effectively simultaneous 35.4 keV de-excitation energy of the daughter nucleus with the K-shell radiation (either X-rays or Auger electrons), signaling a K capture event and the second was from the combined contributions from electron capture from one of the L-, M- or higher shells and the nuclear gamma-ray or internal conversion electron. The L+M+.../K electron capture ratio was the ratio of two peak areas. The authors in [140] measured P_{K} using an external source with an HPGe detector. The experiment was performed in a close geometry in order to achieve efficient summing of X-rays due to electron capture and the following gamma rays. In the obtained X-γ spectrum, 35.46 keV gamma line, 35.46 + K_α sum line along with escape peak of Te K_α were observed. The P_{K} was obtained using formula: $N_{35.46+K_\alpha} = f_{K_\alpha}\omega_K\varepsilon_{K_\alpha}P_{\mathrm{K}}N_{35.46}$. In the formula, f_{K_α} is the fractional K_α intensity, N is the intensity of respective lines, ω_K is the K-fluorescence yield, ε_{K_α} is the absolute efficiency of the K_α line. In the reference [141], the authors measured $P_K\omega_K$ using a Ge(Li) X-ray detector. In [142], the authors measured $P_K\omega_K$ by means of the coincidence measurement in a windowless 4π Si(Li) and scintillation counter. In [143], the authors measured $P_K\omega_K$ by means of K X-ray-γ coincidences with semiconductor detectors. An HPGe detector was used for K x-ray detection and a planar Si(Li) detector for γ-rays. In all these measurements no direct measurement of $P_{\mathrm{L}}/P_{\mathrm{K}}$ has been performed. The only available direct experimental value of $P_{\mathrm{L}}/P_{\mathrm{K}}$ is given by E. Der Mateosian (1953) [144] using a NaI scintillation detector. But the author gave no detailed description of either the dimensions of the source or the details of the detector. In the obtained spectrum, the author observed peaks corresponding to the

addition of conversion electrons and x-rays. Both L and K X-ray peaks were shifted by the 35.5 keV energy from the gamma transition. The $P_{\mathrm{L}}/P_{\mathrm{K}}$ corresponds to the ratio of peak areas.

- Discussion

Our value of the $P_{\mathrm{L}}/P_{\mathrm{K}}$ fractional capture probability ratio of $^{125}\mathrm{I}$ is in agreement with E. Der Mateosian's value, which is the only direct measurement found in the literature. Using the calculated value for P_{O} = 0.001318, the absolute fractional capture probabilities can also be inferred: P_{K} = 0.7216 (17), P_{L} = 0.1991 (17), P_{M} = 0.0590 (32) and P_{N} = 0.0190 (28). The values obtained in this measurement are quite different from those obtained from the BetaShape code. The reason behind this large variation can be that during the preparation of the absorber-source ensemble, the thickness of the absorbers was reduced by quite a large fraction. From the Monte-Carlo simulation, the correct thickness to absorb all the decay energy is 210 µm, but during the diffusion welding process, the thickness was reduced to 149 µm. Unfortunately, this error was observed only after the spectrum was obtained, and as it was mentioned, there were several escape peaks observed in the spectrum, and there was a population related to escape peaks. As the absorber was a combination of an AuAg alloy on the inner part and Au layer on the outside, certainly most of the reduction in thickness happened in the Au layer since the alloy is harder than gold.

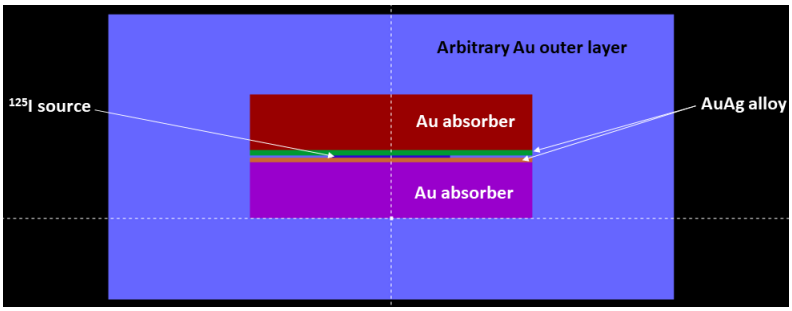

Figure 4.5: Geometry of the detector having an arbitrary Au layer to observe the escape peaks in the Monte-Carlo simulations.

This observation was also verified using the Monte-Carlo simulation performed with the dimensions of the actual detector. The simulated detector was surrounded by a virtual outer detector of Au; see Figure 4.5 for reference. The obtained spectrum shown in Figure 4.6 shows the peaks observed in the non-existing (arbitrary) outer detector of Au, and peaks both from Te and Ag were observed. As in the Monte-Carlo simulation, there is no integration of time, the gamma and X-rays appear at their respective energies.

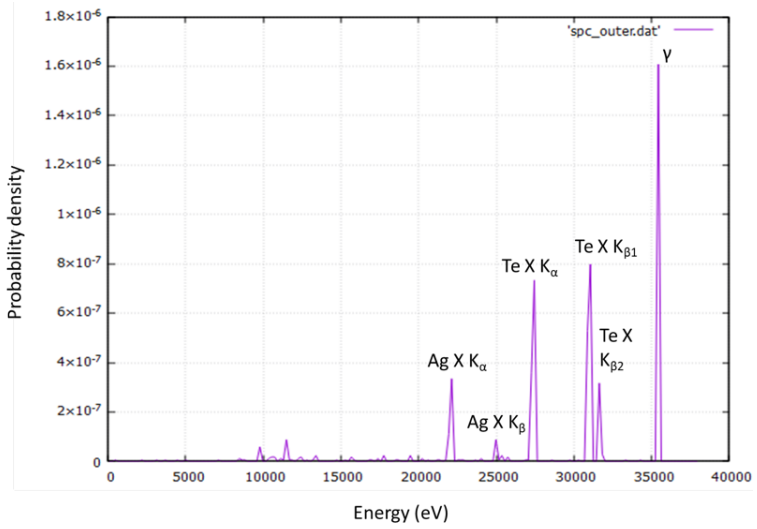

Figure 4.6: Energy spectrum from the Monte-Carlo simulations.

4.2 . Manganese-54

Manganese-54 is a versatile radiotracer that can be used in a variety of applications. It is used to calibrate and determine the efficiency of counting systems used in gamma spectrometry. Its K X-ray lines are also used for low energy efficiency calibration (< 6 keV) of low energy Si (Li) and HPGe detectors. $^{54}\mathrm{Mn}$ disintegrates by electron capture (99.9997 (3) %) to the 834.855 keV excited level (2+) of $^{54}\mathrm{Cr}$, and by very weak electron capture and β^+ transitions to the ground state (0+) of $^{54}\mathrm{Cr}$. It has a half-life of 312.3 days. The decay scheme and the binding energies of the electrons are shown in Figure 4.7. The EC transition is allowed while the β^+ is a unique 2^{nd} forbidden transition.

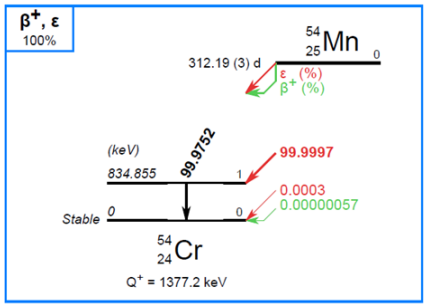

Electron shell	Energy (keV)
K	5.9892
L1	0.6946
L2	0.5837
L3	0.5745
M1	0.0741

Figure 4.7: The decay scheme of $^{54}\mathrm{Mn}$ and the binding energies of the electrons [35].

The measurement of fractional electron capture probabilities of $^{54}\mathrm{Mn}$ was part of the EMPIR MetroMMC project. Two different measurements using two different sources were performed. The first measurement using a Au nanofoam source foil was performed in 2020, before the beginning of this thesis. The analysis of this measurement was done during this thesis. The second measurement using an electroplated source on gold was performed in 2021 during the thesis.

- Au nanofoam source (2020 measurement)

The source was prepared on Au nanofoam (NPAu) using a micro-drop dispenser. The NPAu was prepared from 20 µm thick AuAg alloy using wet etching with 20% HNO_3 at 50 °C for 2 hours. Before wet etching, the AuAg alloy was diffusion welded to a 25 µm thick Au foil, which will act as one-half of the absorber. The other half of the absorber was made from 10 µm thick Au foil. The dimensions of the bottom absorber were $460 \times 460 \times 25\,\mu m^3$ and the top absorber was $440 \times 440 \times 10\,\mu m^3$. The energy spectrum obtained from the measurement in a double logarithmic scale is shown in Figure 4.8.

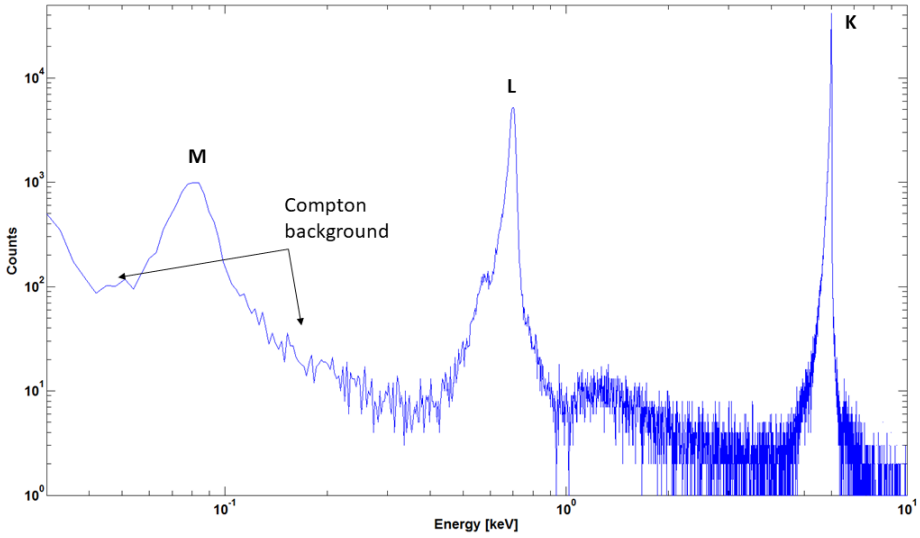

Figure 4.8: The total energy spectrum of $^{54}\mathrm{Mn}$ in a double-log scale.

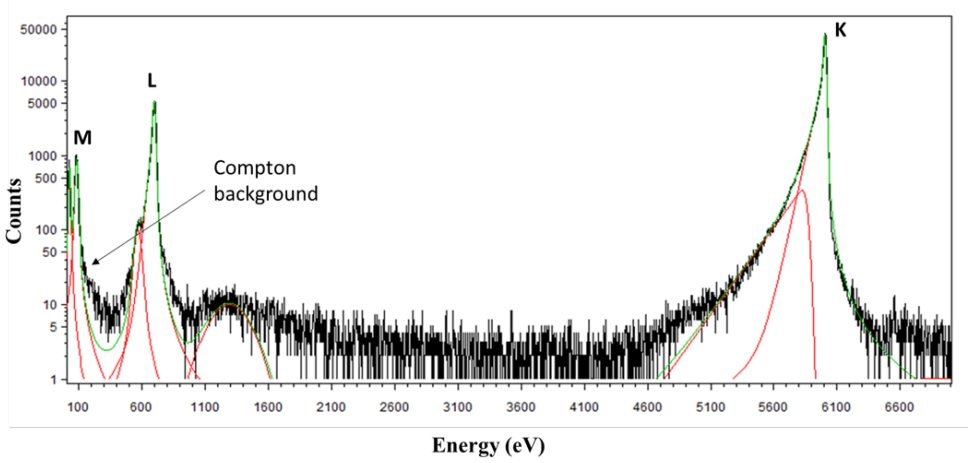

Figure 4.9: The spectrum analysis of $^{54}\mathrm{Mn}$ in a logarithmic Y- scale.

The K capture line can be seen just below 6 keV, the L captures at ~ 700 eV, and the M captures can be distinguished, below 0.1 keV, just above the noise visible at near zero energy, see Figure 4.8 for reference. On the left side of the principal L peak, a shoulder is observed. This may be due to captures on the L2 and L3 sub-shells. The background between the L and M populations and just on the left of the M line increasing towards low energies can be identified as Compton background from the 835 keV gamma photons. The Compton background was also expected from a Monte Carlo simulation, see Figure 4.10. The steeper increase below ~ 40 eV is due to noise triggers. Just above 1 keV, on the right-hand side of the L line, a less peaked population of unknown origin can be seen. We do not have a complete theoretical spectrum for $^{54}\mathrm{Mn}$ yet, but in the theoretical spectrum of $^{65}\mathrm{Zn}$ several satellite lines of low intensity and closely spaced in energy are predicted at higher energies than the main L1 peak. Satellite lines appear at higher energy values than the main peak due to the atomic effects like shake-off and shake-up. It is possible that the unidentified population in the $^{54}\mathrm{Mn}$ spectrum corresponds to these lines, which could be present also in the $^{54}\mathrm{Mn}$ emission spectrum, but are not resolved as individual lines in the measurement.

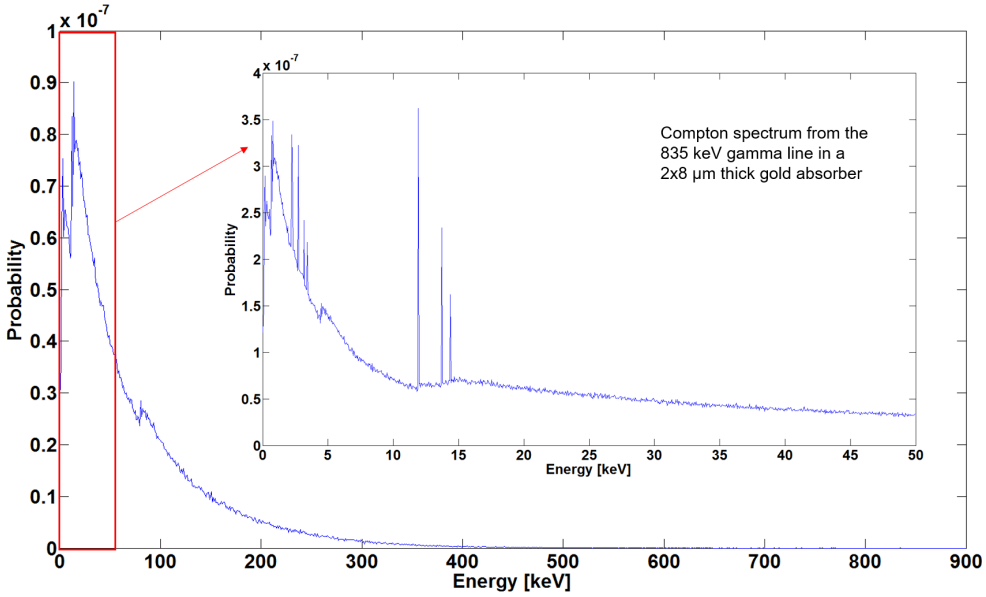

Figure 4.10: Monte-Carlo simulated Compton spectrum of the 835 keV gamma photons from the $^{54}\mathrm{Mn}$ decay in the source layer inside the Au absorber. The lines can possibly be attributed to resonances in the Compton scattering [150].

The K and L lines exhibit low energy tails. Although the nanofoam having pores in the 10-100 nm range limits the size of individual salt crystals forming during the drying of the solution, Auger electrons probably lose part of their energy in the salt, giving rise to the tails. Quantification of the peak areas in this spectrum is not straightforward. The line shapes do not correspond to any fit functions implemented in the common spectrum analysis programs. This is mainly due to the tailing due to incomplete thermalization of the part of energy deposited in the salt constituting the source. Using the program COLEGRAM developed at CEA, each population – K, L1, L2/3 and M – was fitted using several lines distributed within its energy range, see Figure 4.9. The peak area for each of the populations cor-

responds to the sum of the individual fit functions. Two different fits using both Gaussian and Voight with or without a tail and different template lengths were performed. The fitted spectrum shown in 4.9 is one of those spectra. The resulting peak areas from fits showing somewhat different, but reasonable agreement with the data were averaged to calculate the fractional capture probabilities. The calculated values are given in Table 4.4.

- Electroplated source on Au foil (2021 measurement)

The experimental spectrum of $^{54}\mathrm{Mn}$ measured during the thesis is shown in Figure 4.11. The source used was the electroplated source from PTB described in subsubsection 3.2.4.2 For the measurement of the very low energy radiations of this nuclide (< 6 keV photons and electrons; practically all of the 835 keV gamma photons escape from the absorber, leaving only a small Compton background), an XS-size MMC chip was chosen as the best match for the heat capacity of the absorber (~ 6.4 pJ/K at 20 mK) with the dimensions given in Table 3.4. Several attempts were made to measure the spectrum from this source but were unsuccessful. The experimental conditions during the measurement were far from optimal. One cause was the very low activity on the source received and the second was the instrumentation defaults. During the detector preparation phase, it was observed that the gold stems on the sensor of the XS-size MMC chip were not well attached. Trying several times to glue the absorber to different XS sensors, the stems completely came off the sensor. Another difficulty was that during the measurement the pulses observed were very small with a long rise time. Hence the energy resolution was bad, i.e. 350 eV for K capture (6 keV). The L capture peak could not be differentiated from the noise: triggering on the L capture events, noise was also triggered. Hence the quantification of the peak areas in this spectrum was not possible. In the figure 4.11 the K capture peak is visible along with the noise. Due to the bad performance of the detector, the detector threshold was too high (~0.6 keV) to observe the M capture line (~74 eV).

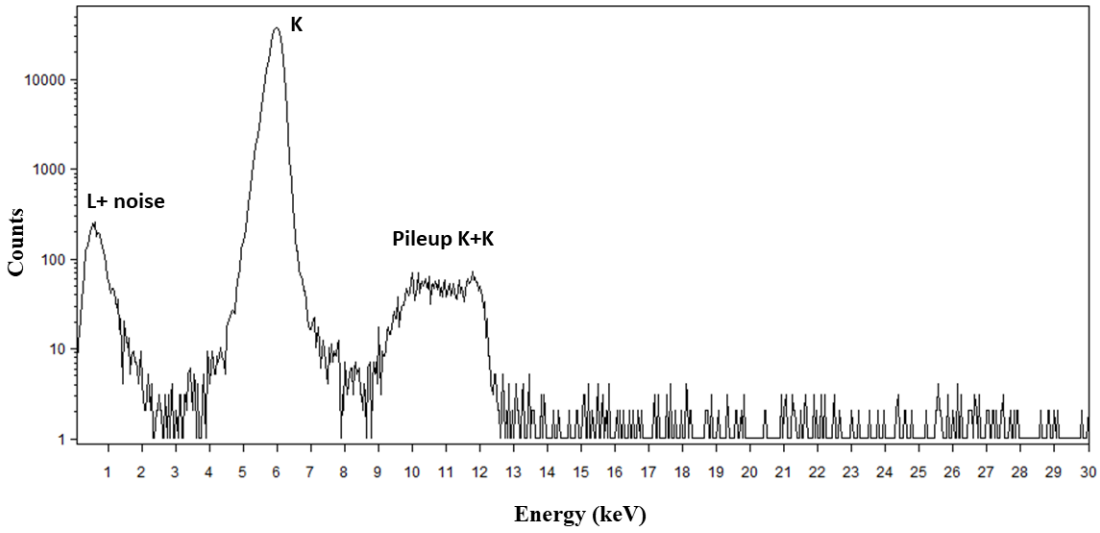

Figure 4.11: The energy spectrum of $^{54}\mathrm{Mn}$ obtained with the electrodeposited source in log Y scale.

- Discussion

The table 4.4 shows the comparison of the fractional EC probability ratios for measurement performed using a nanofoam source with the values from BetaShape and the previous experimental values in the literature.

Table 4.4: Fractional EC probability ratios of $^{54}\mathrm{Mn}$.

Fractional EC probabilities	Experimental	BetaShape [17]	Literature
$P_{\mathrm{L}}/P_{\mathrm{K}}$	0.11320 (21)	0.11219 (31)	0.098 (6) [145], 0.106 (3) [146], 0.096 (5) [147]
$P_{\mathrm{M}}/P_{\mathrm{K}}$	0.01686 (23)	0.01746 (11)	-

In the literature, three measurements for $P_{\mathrm{L}}/P_{\mathrm{K}}$ were found. In the reference [145], the authors measured the $P_{\mathrm{L}}/P_{\mathrm{K}}$ ratio for $^{54}\mathrm{Mn}$ using a multi-wire anti-coincidence proportional counter using the equation $\frac{P_L}{P_K} = \left[\frac{N_L}{N_K}\right][1 - P\omega_K] - P\omega_K k_\alpha$, here $\frac{N_L}{N_K}$ is the observed intensity ratio of the L and K peaks, ω_K is the K-fluorescence yield of the daughter element, k_α is the fraction of K_α X-rays in the K X-rays series, P is the sum of the fraction of X-rays from the center counter, which escapes through the ends of the counter and the fraction of X-rays from the center counter, which hit the wires of the center counter and are not detected, and the fraction of X-rays from the center counter, which escapes and also passes through the ring counters undetected.

In the reference [146], the authors performed the measurement of $^{54}\mathrm{Mn}$ gaseous sources with a high-pressure, multi-wire proportional counter. The experiment was conducted at argon pressures of 300 and 400 kPa, utilizing methane with a pressure of 21.3 kPa to serve as a quenching gas. The authors observed the peak half-widths to be marginally broader than typically anticipated at these energy levels, a phenomenon attributed to the CO radicals present in the manganese compound. The equation $\frac{L}{K} = \left[\frac{N_L}{N_K}\right][1 - (P_2 + P_4)\,\omega_4] - [P_1 + P_2 + P_3]\,\omega_K k_\alpha$ was used to calculate the capture probability. In this equation, $\frac{N_L}{N_K}$ is the observed intensity ratio of the L and K peaks, P_1 is the probability that a K_α X-ray will escape the central counter through the ends; P_2, that the X-ray will escape the central counter and hit a cathode wire; P_3, that the X-ray will escape the central counter and pass through the ring counter without being absorbed; P_4, that the X-ray will escape the central counter and hit the containing cylinder; k_α is the fraction of K_α X-rays in the K series; ω_K is the K-fluorescence yield of the daughter element.

In the reference [147], the authors measured the fractional probability of K captures of $^{54}\mathrm{Mn}$ by measuring coincidences between the gamma transition from the excited state to the ground state and X-radiation and/or Auger electrons following the K capture process. The measurement was performed using a double proportional counter. The proportional counter was filled with Argon-methane (9:1) to a pressure of 5 kPa. A conducting foil of area 3×10 cm^2 was placed on the wall between the two counters. On this conducting foil, carrier-free $^{54}\mathrm{Mn}$ was deposited.

In the table 4.4, the quoted uncertainties on the MMC fractional capture probability ratios ("Experimental") are composed of the statistical uncertainties associated with the peak areas, as well as an

uncertainty component resulting from the scatter of the peak areas obtained with the different fits. The detailed explanation of uncertainty calculation is given in the section on ^{125}I results. For this nuclide, a good agreement between the MMC measurement and the theoretical value from BetaShape is observed for the $P_{\mathrm{L}}/P_{\mathrm{K}}$ value and agreement to within 2σ for $P_{\mathrm{M}}/P_{\mathrm{K}}$, whereas the agreement with other experimental values from the literature [145–147] is less good. Using the calculated value for P_{N} = 0.0006, the absolute fractional capture probabilities can also be inferred: P_{K} = 0.873 (7), P_{L} = 0.107 (3) and P_{M} = 0.0185 (5).

4.3 . Nickel-59

Nickel-59, one of the radionuclides chosen for the MetroMMC project, decays mainly by EC to the ground state of ^{59}Co and has a half-life of 76000 years. The decay is a 2^{nd} forbidden non-unique transition. The decay scheme and the binding energies of the electrons are shown in Figure 4.12.

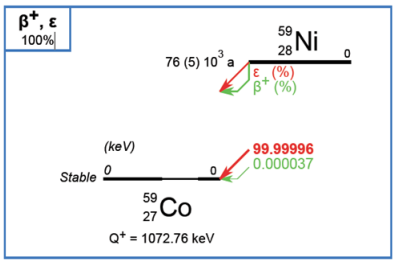

Electron shell	Energy (keV)
K	7.7089
L1	0.9256
L2	0.7936
L3	0.7786
M1	0.1007

Figure 4.12: ^{59}Ni decay scheme and the binding energies of the electrons [35].

^{59}Ni is used to date the terrestrial age of meteorites and determine the abundance of extraterrestrial dust in ice and sediment. The decay data of ^{59}Ni is required in nuclear power plant radioactive waste qualification as ^{59}Ni is produced in thermal-nuclear reactors as an activation product of Ni-cladded control rods and other steel structural components. It is present in nuclear waste, and its detection is complicated because of its long half-life and the absence of γ-rays emission. From the literature review, only a single direct measurement of $P_{\mathrm{K}}/P_{\mathrm{L}}$ was observed [148]. The previous measurement was performed using a wall-less multi-wire proportional counter. The non-availability of experimental data also makes this measurement important.

Two different source preparation techniques were employed to prepare thin homogeneous sources of high quality as described in subsubsection 3.2.3.3 and 3.2.4.3. Both the absorbers were placed on the two sensors of the same S-size MMC chip. The heat capacities of the Au absorbers were respectively 14.6 pJ/K at 20 mK with the electrodeposited source enclosed and 11.5 pJ/K at 20 mK with the drop deposited source enclosed. The choice was to either use an XS size chip (optimized for an absorber heat capacity of 8 pJ/K at 20mK) or an S size (absorber heat capacity of 28 pJ/K at 20mK), see Table 3.1. As in the measurement of ^{54}Mn some difficulties were observed in using the XS size chip, it was decided to use an S size chip for this measurement. The full energy spectra obtained from both the electroplated as well as drop deposited source in a 4π geometry are shown in linear Y scale in Figure 4.13 and log Y scale in 4.14, respectively. In the linear Y scale, three peaks corresponding to respective captures on the K, L, and M shells are observed. The K peak is observed at 7.7 keV and L at 0.9

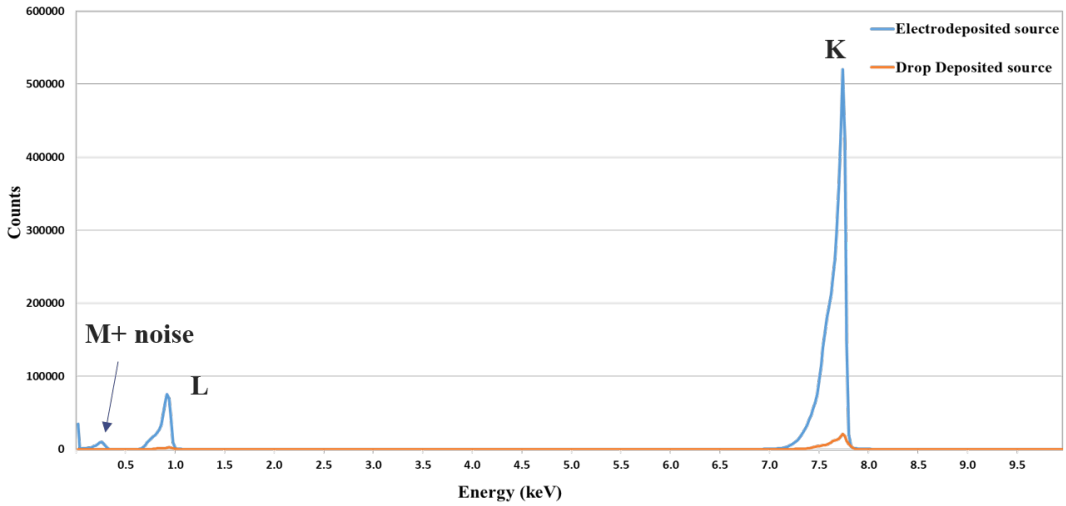

Figure 4.13: The comparison of energy spectrum of ^{59}Ni from both sources in a linear Y scale.

keV. However, the M peak is not differentiated from the noise and noise triggers that occurred while triggering the M capture events. In the log Y scale, more details about the spectrum are observed.

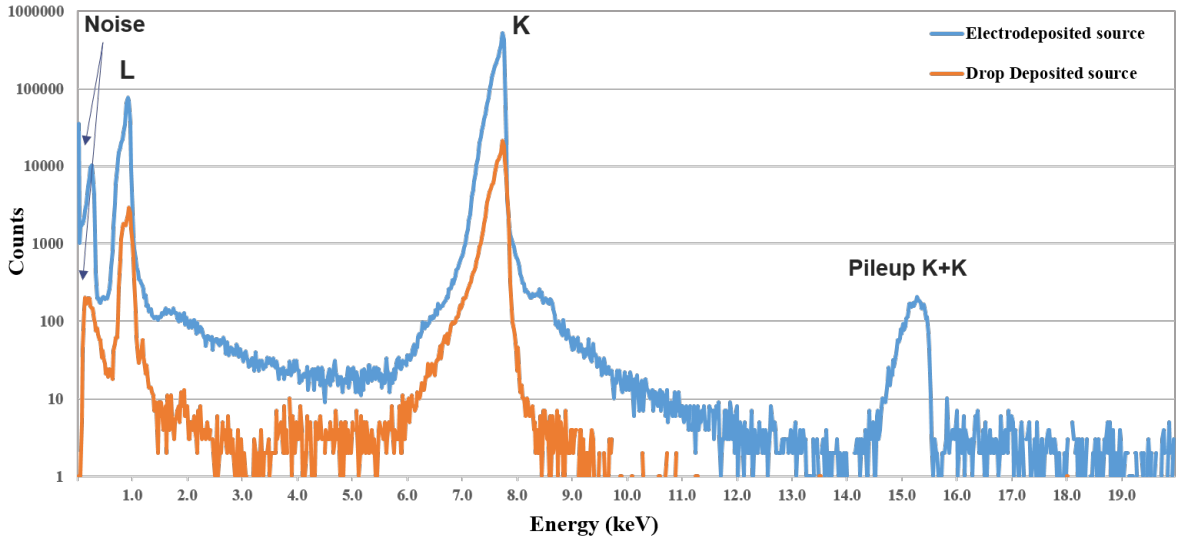

Figure 4.14: The comparison of energy spectrum of ^{59}Ni from both sources in a log Y scale.

- Electroplated source

The fitted spectrum of the electroplated source in the log Y scale is shown in Figure 4.15. The data analysis steps were the same as in the analysis of previous measurements. The spectrum contains about 6.5×10^6 EC events after filtering, cuts, and corrections. The pulses had a 10–90% rise time of 170 µs, and the pulse decay follows an exponential, giving a 1/e decay time of 4 ms. In conjunction

with 9 Bq source activity, this results in a small fraction of pile-up for both K and L capture on the right side of the principal peaks.

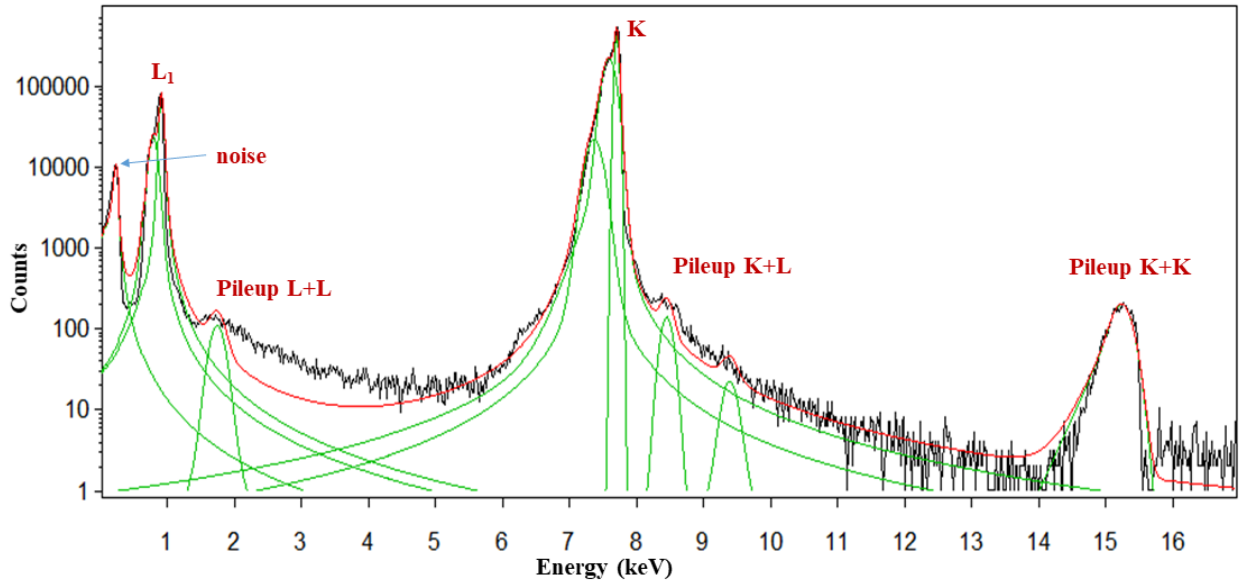

Figure 4.15: Fit of the electroplated source spectrum of $^{59}\mathrm{Ni}$ in log Y scale.

The number of events in the K+K pileup peak is accounted for as two K capture events each, in the K + L pileup as one K and one L capture each, and in the L + L pileup as two L captures each. On the left side of the principal L capture peak, a shoulder is also observed and is an artifact from auger electrons. The ratio of area of the shoulder to L1 peaks was measured (0.505) and this did not match the L2/L1 BetaShape code value (0.006). A similar shoulder is observed on the left side of the K capture peak, but this time it corresponds to the interaction of Auger electrons and X-rays emitted after K capture. In all peaks, a low-energy tail is observed due to the loss of a portion of the energy of Auger electrons in the source material (0.55% of the K-peak events in the tail). A small percentage of unresolved pile-up (0.27% for K+L) results in the tail on the right side of the K-peak. A fraction of 0.098% of K+K pileup is present at 15.2 keV and 1.25% of L+L pileup is present at 1.8 keV.

- Drop-deposited source on Au nanofoam

The fitted spectrum from the source prepared by drop deposition on Au nanofoam in log Y scale is shown in figure 4.16. The pulses had 10–90% rise times of 170 µs, and the pulse decay follows an exponential, giving a 1/e decay time of 4.4 ms. The activity on the source is 3 Bq. The final spectrum contains about 4.9×10^5 EC events after filtering, cuts, and corrections.

On the left side of the principal L capture peak, a shoulder is observed similar to the one observed in the electroplated source, and on the right side, there is a small unknown population. The ratio of area of shoulder on the left to L1 came out to be 0.631 and did not match with the L2/L1 BetaShape value of 0.006. Similar unknown populations on the right side of the L peak were also observed in the case of $^{54}\mathrm{Mn}$ and $^{65}\mathrm{Zn}$ (measurement at PTB within the MetroMMC project). As mentioned in

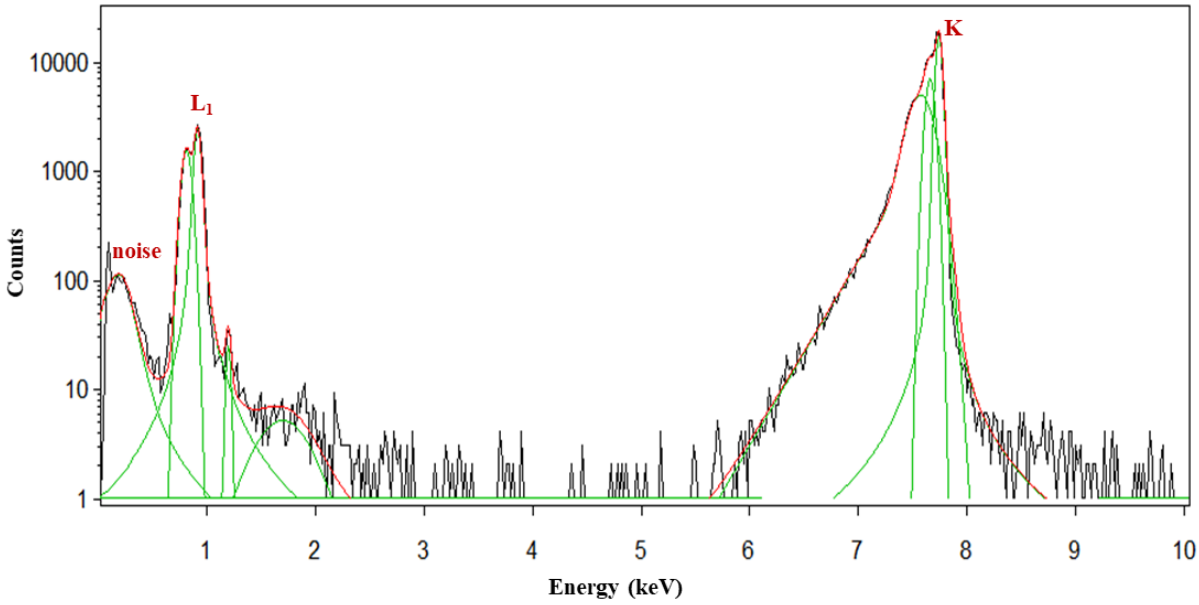

Figure 4.16: Fit of the drop deposited source spectrum of ^{59}Ni in log Y scale.

section 4.2 (^{54}Mn), it may be a satellite structure related to the L captures. (A pile-up from the K peak is not observed in this spectrum; that is due to the setting of the SRS amplifier combined with the limitation on the dynamic range of the data acquisition system. However, an L+L pileup population is present also in this spectrum. In all peaks, a low-energy tail is observed due to the loss of a portion of the energy of Auger electrons in the source material (2.58% for K peak). The M capture peak is not separated from noise.

- Discussion

As it was expected, in the source prepared from the drop deposition the low energy tailing on the left side of the principal peaks (2.6% for K-peak) is more prominent than in the electroplated source (0.55% for K-peak). This low energy tail is due to the loss of a portion of the energy of Auger electrons in the source material leading to incomplete thermalization. Also, the electroplated source had a better energy resolution of 57.4 eV (FWHM) for the K peak, while the energy resolution for the drop deposited source was 86.5 eV (FWHM) for the K peak. The quoted energy resolutions are the FWHM of the main Gaussian fit peak; it does not include the low energy tail. The better energy resolution obtained with the electroplated source than with the drop-deposited source also proves that the source preparation and the presence of salt crystals affect the spectrum to a great extent, even in this case where the crystal size of the drop-deposited source is minimized by the pore size of the gold nanofoam.

In both spectra, quantification of the peak areas was challenging. The shapes of these lines don't match the fit functions found in standard spectrum analysis software. As mentioned before, this discrepancy is largely due to the partial thermalization of the energy deposited at the source. The peak areas were determined using the program COLEGRAM as in the previous cases. The obtained values from the measurement are given in Table 4.5.

Table 4.5: Fractional EC probabilities ratios of $^{59}\mathrm{Ni}$

Fractional EC probability ratio	Electroplated source	Drop-deposited source	BetaShape [17]	Literature
$P_{\mathrm{L}}/P_{\mathrm{K}}$	0.1154 (11)	0.1122 (22)	0.11590 (26)	0.1210 (20) [148]

In the literature, there is only a single direct measurement of $P_{\mathrm{L}}/P_{\mathrm{K}}$ in the reference [148]. In this article, the authors measured the $P_{\mathrm{L}}/P_{\mathrm{K}}$ ratio using a wall-less multi-wire proportional counter surrounded by an anti-coincidence ring counter. The source was in the form of gaseous nickelocene, $C_{10}H_{10}Ni$, present in the couter gas with a pressure of 500 kPa. The authors used the equation $\frac{L}{K} = \left[\frac{N_L}{N_K}\right][1-(P_\alpha k_\alpha + P_\beta k_\beta)\,\omega_k] - \omega_K k_\alpha P_\alpha$ to calculate the ratio. In this equation, $\frac{N_L}{N_K}$ is the observed intensity ratio of the L and K peaks, ω_K is the K-fluorescence yield of the daughter element, k_α and k_β is the fraction of K_α and K_β X-rays in the K series respectively. P is the combination of the probabilities that a photon strikes a central counter cathode wire and that an X-ray passes from the center counter through the ring counter undetected; and that an X-ray escapes through the ends of the counter for K_α and K_β X-rays in the K series.

The quoted uncertainties on the MMC fractional capture probability ratios in 4.5 are composed of the statistical uncertainties associated with the peak areas, as well as an uncertainty component resulting from the scatter of the peak areas obtained with different fits. Again, for the electrodeposited source, the $P_{\mathrm{L}}/P_{\mathrm{K}}$ value measured by MMC is in agreement with the value from BetaShape to within the standard uncertainty, and for the drop deposited source to within 2σ. The only previously published experimental value [148] is a bit further off.

4.4 . Carbon-14

Carbon-14 decays by 100% of β^- to the ground state of $^{14}\mathrm{N}$. Although decaying via an allowed transition, it has an unusually long half-life, and the spectrum shape is influenced by a strong nuclear structure effect. It is the case of accidental cancellation of the nuclear matrix elements prominent in allowed transitions.So, this measurement is essential for studying its beta spectrum shape influenced by the nuclear structure. $^{14}\mathrm{C}$ is an interesting radionuclide as it is used in radiocarbon dating due to its existence in organic materials and is used to estimate the age of carbonaceous materials up to 60,000 years old. It is also used as a radioactive tracer in nuclear medicine.

The measurement of the beta spectrum of $^{14}\mathrm{C}$ was part of the MetroBeta EMPIR project and the first measurement was performed in 2019 [37,149]. However, the conditions during that measurement were not optimal. The detector's performance was degraded during the cooling down; the MMC chip came off the detector holder due to the breaking of the glue layer. The chip was held in place only by the gold and aluminum bonding wires used for electrical and thermal contacts. Due to this, the thermal time constant of the detector was longer than expected, with more than 50% accumulated pulses being piled up, needing to be removed. Following a ten-day data collection period with a count rate of approximately 7 counts per second, a concluding spectrum contained 2.7 million events. Also,

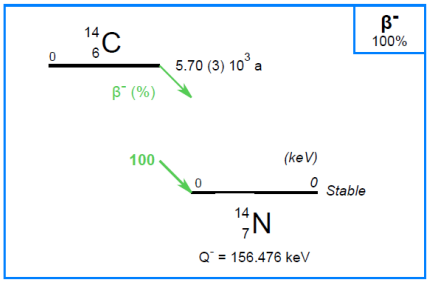

Figure 4.17: Decay scheme of ^{14}C [35].

as the MMC was held only by bonding wires, a degraded energy resolution of 200 eV (FWHM) was observed due to vibrations, about a factor 5 worse than expected. An external calibration source containing both $^{109}\mathrm{Cd}$ and $^{55}\mathrm{Fe}$ was used. The 22 keV, 26 keV, and 88 keV are K X-ray and gamma-ray lines from $^{109}\mathrm{Cd}$. The double line around 6 keV is the $\mathrm{K}_\alpha + \mathrm{K}_\beta$ line from the $^{55}\mathrm{Fe}$ source. Another observation was an unexpected increase in the spectrum below 6 keV.

Peaks observed in spectrum	Energy (keV)
^{55}Fe K_α	5.89
^{55}Fe K_β	6.51
^{109}Cd K_α	22.16
^{109}Cd K_β	25.00
^{109}Cd γ	88.03

Peaks observed in spectrum	Energy (keV)
X K_α (^{57}Co)	6.40
Au escape (γ_2) $K_{\alpha1}$	53.21
Au escape (γ_2) $K_{\alpha2}$	55.03
Au escape (γ_2) $K_{\alpha3}$	44.04
γ_1 (^{57}Co)	14.42
γ_2(^{57}Co)	122.06
γ_3 (^{57}Co)	136.47

Figure 4.18: The energy of the peaks observed from calibration sources $^{55}\mathrm{Fe}$ and $^{109}\mathrm{Cd}$ for 2019 measurement and $^{57}\mathrm{Co}$ for 2021 measurement.

To improve on the 2019 measurement, a remeasurement using the same $^{14}\mathrm{C}$ source was performed during the thesis. This time, $^{57}\mathrm{Co}$ was used as an external calibration source. In Figure 4.19, three beta spectra are shown from the 2019 measurement in blue, from the 2021 measurement in orange, and the grey one is from the BetaShape code [17].

The 2021 measurement slightly improved the energy resolution from 200 eV to 155 eV (FWHM) and the energy threshold from 1.5 keV to 1 keV, but can be improved further. Also, the spectral increase below 6 keV was not observed, confirming the assumption that the increase was due to the non-optimal conditions of the previous measurement.

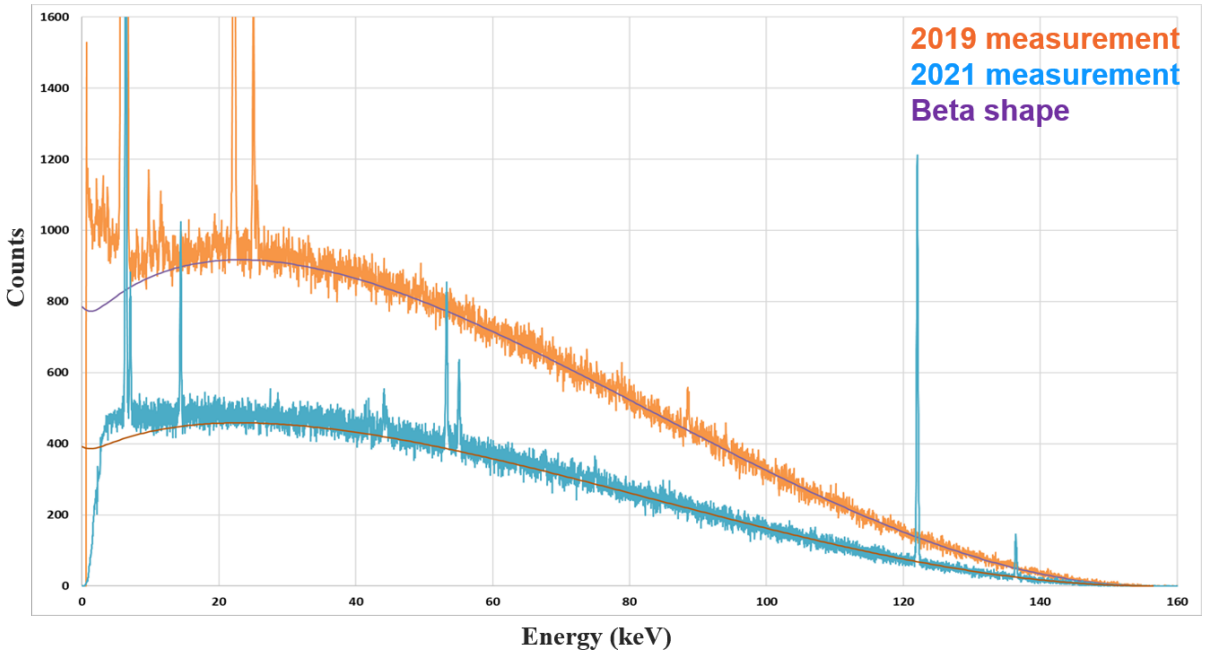

Figure 4.19: The comparison of the measured beta spectrum of ^{14}C from the 2019 and 2021 measurements along with the theoretical spectrum from the BetaShape code in linear Y scale. Below the ^{55}Mn X K lines ($\sim$ 6 keV) an abnormal increase of the spectrum is clearly visible; this increase is absent in the 2021 measurement. It can be concluded that the too high probability at low energies was due to the non-optimal experimental conditions (see text for details).

4.5 . Chromium-51

The Chromium-51 measurement for determining fractional electron capture probabilities is also planned in the near future. As explained in the subsubsection 3.2.4.1, the activity on the prepared electroplated source was quite high. So, the measurement could not be performed immediately, the source was kept for 3 half-lives without any manipulation to reduce the activity to a handleable amount of 127.5 Bq. The dimensions of the source prepared for the measurement are $190 \times 190 \times 5\,\mu m^3$ with 7.5 Bq activity and the two gold absorber halves of dimensions $450 \times 450 \times 10\,\mu m^3$. After the absorber-source ensemble was diffusion welded at 400 °C for 2 hours, it was glued to the sensor of the MMC size S chip using Stycast. The complete detector is shown in Figure 4.20.

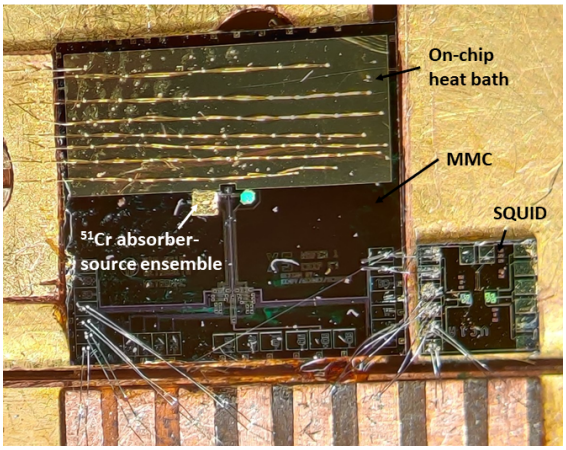

Figure 4.20: Complete detector for $^{51}\mathrm{Cr}$.

4.6 . Iodine-129 source preparation

The measurement of the beta spectrum of $^{129}\mathrm{I}$ is part of the EMPIR project PrimA-LTD. It disintegrates via 100% beta emission to the 39.58 keV excited state of $^{129}\mathrm{Xe}$. The decay scheme is shown in Figure 4.21.

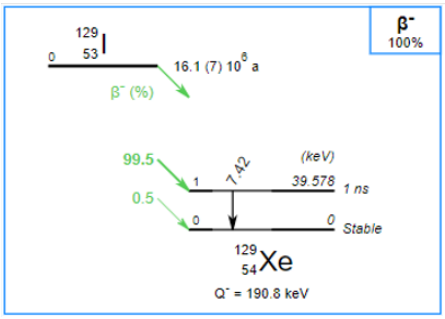

Figure 4.21: The decay scheme of $^{129}\mathrm{I}$ [35].

Due to the second forbidden non-unique nature of the transition, it is a good candidate to study the theoretical beta spectrum shape. Using DES technique, the beta spectrum will be shifted by 39.58 keV gamma transition. The energy of gamma-ray photons, respectively the conversion electrons from the prompt gamma transition, will be summed with the beta energy, such that the measured spectrum starts at the energy of the gamma transition. The shift will allow measuring the actual beta spectrum down to 0 keV. The measurement will also help validate the theoretical calculation of the atomic effects at the lowest energies where their influence becomes very strong at typically higher than 10%. The high-precision measurements down to 0 keV are important for:

1. The weak interaction for the decay
2. The strong interaction for the nuclear structure due to the dominance of the relativistic matrix elements

3. The electromagnetic interaction for the atomic structure

During this thesis and in the previous MetroBeta and MetroMMC EMPIR projects, it was observed that there is a systematic distortion of the spectrum shape due to the chemical composition of the source material and its preparation technique. The two most promising source preparation techniques for minimizing spectrum distortion are electrodeposition and ion implantation. Electrodeposition cannot be applied to $^{129}\mathrm{I}$ due to the electrochemical nature of iodine, and due to the long half-life of $^{129}\mathrm{I}$, ion implantation of sufficient activity in the small size of an MMC absorber is not possible either. As it was already mentioned, if the radioactive material is in the form of dissolved salts in liquid solutions, the salt crystals forming during the drying of the solution can often cause considerable spectrum distortion. Using a micro-drop dispenser can reduce the size of salt crystals forming after deposition, as the size of individual drops is reduced to a few picolitres, and when dispensing the solution into nanoporous metal then the pore sizes of the nanoporous metal additionally constrain the crystal size. But even in this case, non-negligible spectrum distortion may occur.

However, as discussed in section 3.2.3.1, the strong chemical affinity between iodine and silver opens a way to produce high-quality sources of iodine radionuclides: Iodine homogeneous monolayers can be formed on silver through spontaneous deposition. This method has successfully been applied for the EC measurement of $^{125}\mathrm{I}$ (see section 4.1). As the half-life of $^{129}\mathrm{I}$ is very much longer $(1.6\times10^{7}$ a) than that of $^{125}\mathrm{I}$ (59.4 d), a monolayer on the small absorber size $(\sim 500\times500\,\mu\mathrm{m}^2)$ will not result in a sufficient activity for the MMC measurement. Hence the idea is to enhance the available surface for AgI by creating a nanoporous silver on the absorber foil. This should allow the deposition of sufficient activity without increasing the lateral absorber size. While waiting for the availability of nanoporous silver (NPAg), a first test was the self-deposition of $^{129}\mathrm{I}$ on a plain Ag foil, and for the second test, the NPAg foil was prepared by C2N-CNRS Palaiseau.

4.6.1 . First test using Ag foil for self-deposition

A silver foil of 10 µm thickness was selected. The dimension of the foil were $22\times3\mathrm{mm}^2$. The initial mass activity of the source solution was 34 kBq/g (01/06/99). The chemical composition of the solution was 7.07 mg/g of NaI and 50 µg/g of $\mathrm{Na_2S_2O_3}$. In the solution, for every 1 radioactive iodine ion, there were 1.3 stable iodine ions. The original solution was diluted with water. From this diluted solution, 0.8 mL of solution containing about 0.8 kBq were taken for the self-deposition. The top 11 mm of the silver foil (33 mm^2) were dipped in the solution for 24 hours. The top part of the foil was clamped to suspend the foil inside the solution such that the active solution should not touch the clamp to avoid contamination. The precautions needed to prevent the evaporation of $^{129}\mathrm{I}$ were also taken, as Iodine is volatile in nature.

The activity deposited on the foil was checked using the liquid scintillation counting (LSC) method. Two samples for LSC were prepared with Hionic-Fluor (HF) cocktail. The first sample contained 10 mL of HF and 50 µL of radioactive (RA) solution before dipping the foil, and the second sample was taken after 24 hours and removing the foil from the RA solution. The LSC results show that $66\ \mathrm{mm}^2$ of Ag foil surface (taking into account both sides of the foil exposed to the solution) contain 11.5 Bq of activity. As expected, this activity level per unit surface is insufficient for a 4π MMC measurement. The distribution and homogeneity of the deposition were checked using the autoradiography of the foil, and it pointed towards a homogeneous deposit of $\sim 0.175\,\mathrm{Bq/mm}^2$. The Ag foil after 24 hours of

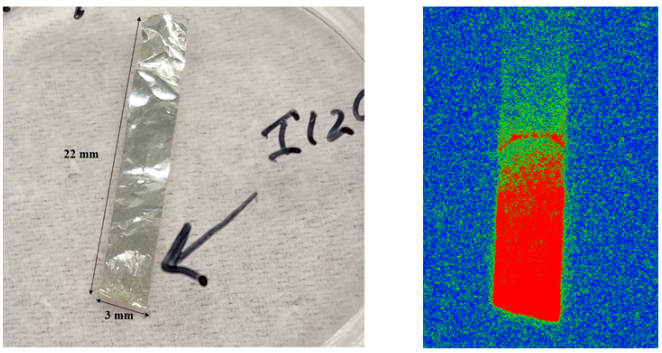

Figure 4.22: The Ag foil after 24 hours of self-deposition in the radioactive solution and the autoradiography of the Ag foil.

self-deposition in the radioactive solution and the autoradiography of the Ag foil is shown in Figure 4.22.

4.6.2 . Second test using Ag nanofoam

A Ag nanofoam (NPAg) sample on a silicon wafer was prepared by CNRS-C2N. To remove the oxidation of the Ag layer, the cut-out piece of Ag nanofoam $(7 \times 8\,\mathrm{mm}^2)$ was first dipped in $\mathrm{HNO_3}$ with pH 3 for about 1 min and then immediately rinsed with deionized (DI) water. The part of foil inside the solution was $6 \times 8\,\mathrm{mm}^2$. The silicon side of the wafer with the nanofoam was stuck to a piece of Kapton masking tape. A Teflon foil was also attached to the same Kapton tape to use the clamp for dipping the foil inside the solution. The extra Teflon foil was used to avoid contamination of the clamp. The foil was dipped inside the same solution of 0.8 kBq activity, which was used for Ag foil self-deposition, for about 24 hours. After that, the Ag nanofoam was rinsed with DI water before autoradiography. To know the deposited activity, LSC was performed. The LSC results showed 18.4 Bq of activity on 48 mm^2. The autoradiography of the foil, as shown in Figure 4.23, shows a rather homogeneous deposition of 0.38 $\mathrm{Bq/mm}^2$.

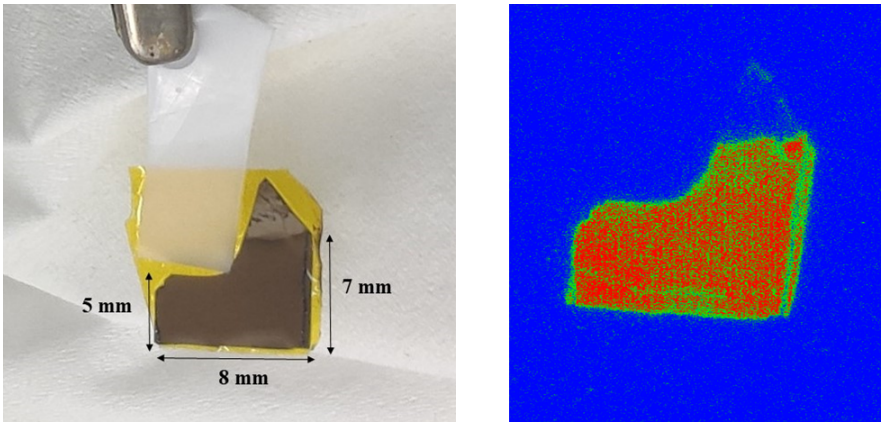

Figure 4.23: The NPAg on silicon used for self-deposition and the autoradiography of the source.

The two tests performed showed that Nanofoam Ag foil (NPAg) is a better choice to prepare the

source with the highest activity: in the case of NPAg, the activity deposited was 0.38 $\mathrm{Bq/mm^2}$ while in the case of plain Ag foil, it was $0.175\,\mathrm{Bq/mm^2}$. Further tests are planned to enhance the deposited activity by using a carrier-free source solution and thicker Ag nanofoam foil.

4.7 . New multichannel spectrometer setup

As the next step in the advancement of the measurements with the MMCs in radionuclide metrology, to reduce the statistical uncertainty, a new multi-pixel MMC array with at least 10 read-out channels will be employed as a part of the PrimA-LTD EMPIR project. In this project, two different sets of MMCs were designed. The first one is called reusable MMC, where the absorber containing the nuclide to be measured will not be directly glued to the sensor of the MMC. The thermal link between the absorber and sensor will be made by gold bonding wires or strips of gold foil bonded to the absorber and the sensor. The second MMC design is fully optimized for one nuclide, namely ^{55}Fe, to achieve the best detector performance for this nuclide. In this design, several MMCs (with two absorbers each) share a common chip, and the bottom half absorbers are electroplated freestanding on gold posts as one of the micro-fabrication steps. The radionuclide will be implanted directly on the bottom halves of the absorbers of the MMC array. Subsequently, the second absorber halves will be deposited equally on top of the source layer by electroplating. The micro-fabrication of two absorber layers in the final dimensions, but without embedded activity, has already been demonstrated successfully. This is the first time that an MMC for DES spectroscopy, including the 4π absorber, was fully micro-fabricated. The multi-pixel array will help to gain counting statistics to achieve statistical uncertainties of low per-mill to $\mathcal{O}$()100 ppm) level in a reasonable measurement time of a few days to a few weeks $(10^8$ events).

To measure the 10 detector channels simultaneously, the spectrometer setup used at CEA was upgraded. As part of this thesis, this upgrade will make it possible to improve the statistics of the measured spectra significantly. The new multichannel spectrometer setup is shown in Figure 4.24. The spectrometer setup comprises 10 individual plates for each MMC chip and 10 individual PCB boards for each SQUID chip, and when reusable MMCs are to be used, 10 individual source-absorber plates can be added. The electrical connections between the MMC and SQUID units to the cryostat are done using PCBs. The individual MMC chips are daisy-chained using PCBs, as shown in Figure 4.25. The MMCs and the SQUIDs are placed on separate support structures having a narrow (0.1 mm) space between them to have a minimum of thermal decoupling between MMCs and SQUIDs in order to minimize heating of the MMCs by the power dissipation in the SQUIDs.

In the case of beta spectrometry, there is an additional calibration source requirement, so a calibration source and collimator plate can also be attached to this design, as shown in Figure 4.24. Individual source carrier plates can be fixed above each collimator aperture. All the components, except the absorber-source plate, the collimator plate, and the PCBs, are made of gold-plated copper. The absorber-source plates are made of aluminum. The choice of aluminum was made to thermally decouple the absorbers from the holder and ensure that the heat deposited by a particle flows to the sensor. Aluminum is superconducting (T_c = 1.2 K) and at low mK temperatures has a much lower thermal conductivity than the gold bonding wires connecting the absorbers to the sensors. The shielding cylinder is made of a combination of lead as a superconducting magnetic shielding and copper as a

support for the (soft) lead cylinder.

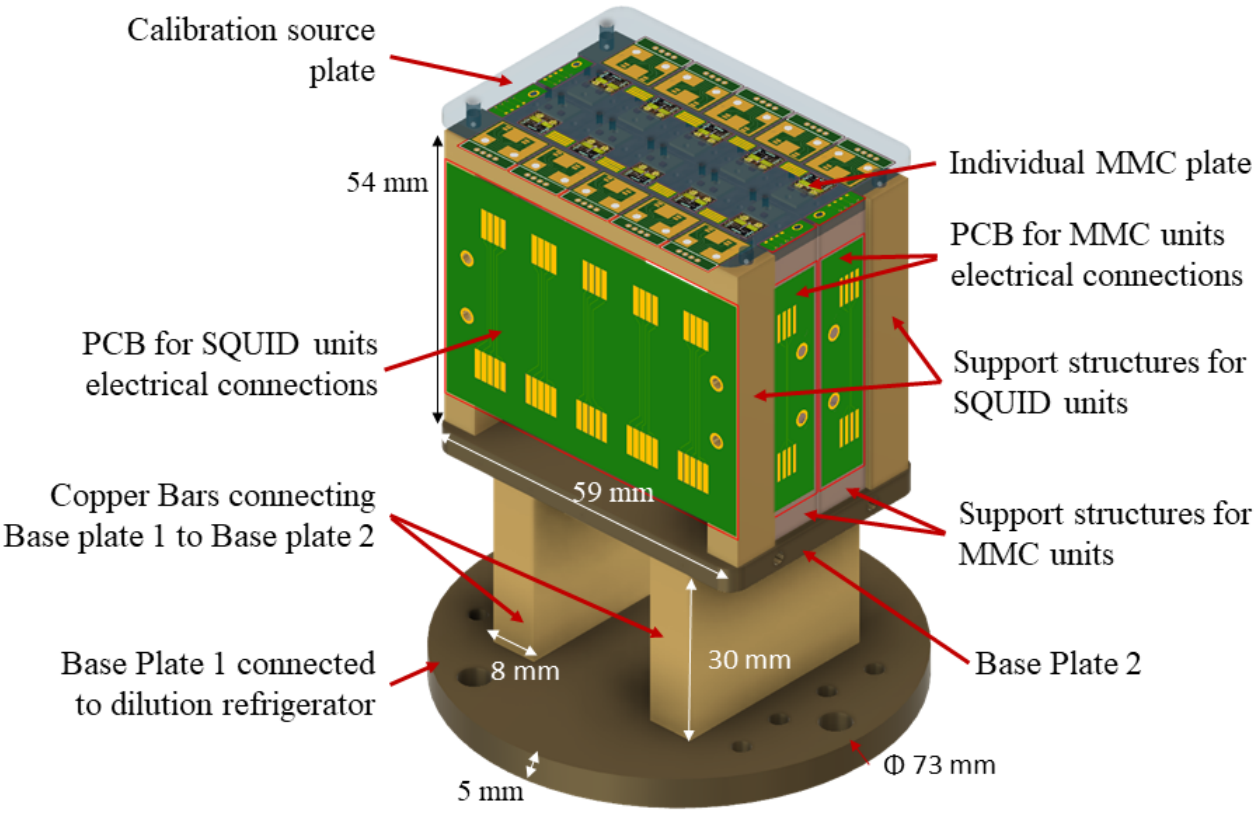

Figure 4.24: New multichannel spectrometer setup.

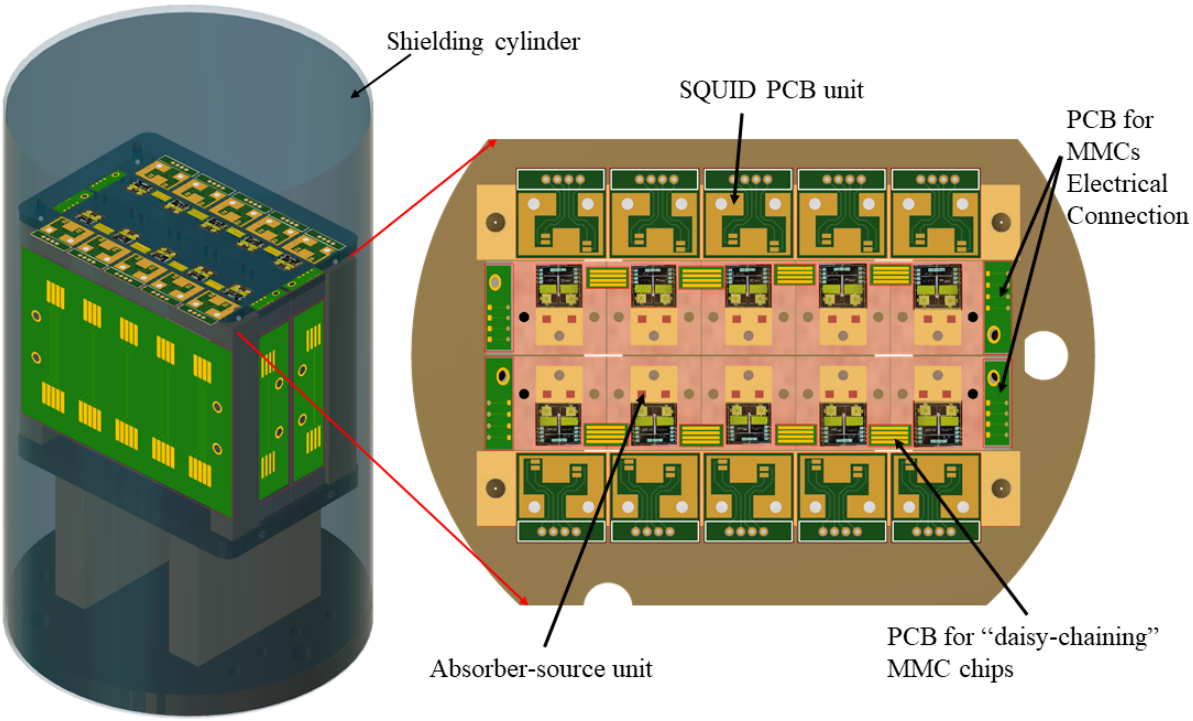

Figure 4.25: The shielding cylinder for the spectrometer and the MMC-SQUID unit design details.

4.8 . Measurement results conclusion

This chapter described the measurements of fractional capture probability ratios for three radionuclides, ^{125}I, ^{54}Mn and ^{59}Ni, and of the beta spectrum of ^{14}C. The EC ratios for ^{125}I need to be measured again with the correct absorber thickness, and the uncertainties in the measured value can be additionally improved by depositing the source in a nanofoam Ag foil instead of normal Ag metal foil. For the case of ^{54}Mn, a good agreement between the MMC measurement and the theoretical value from BetaShape is observed for the $P_{\mathrm{L}}/P_{\mathrm{K}}$ value and agreement to within 2σ for $P_{\mathrm{M}}/P_{\mathrm{K}}$. For ^{59}Ni using the electrodeposited source, the $P_{\mathrm{L}}/P_{\mathrm{K}}$ value measured by MMC is in agreement with the value from BetaShape to within the standard uncertainty, and for the drop deposited source to within 2σ. So we suggest that the measured fractional EC ratio values for ^{54}Mn and ^{59}Ni can be used to update the available values in the decay data tables. The measured ^{14}C beta spectrum revealed that the increase below 6 keV, noted in the 2019 measurement, resulted from non-optimal experimental conditions. There was also a slight improvement in energy resolution in the recent measurement.

With the upgraded spectrometer setup introduced in this chapter, the statistical uncertainties will be reduced in near future measurements.

5 - Summary and Perspectives

The aim of this doctoral thesis entitled 'Measurement of nuclear decay data for beta decay and electron capture using metallic magnetic calorimeters' prepared at LNHB-MA, CEA Paris-Saclay is to determine the decay data (spectrum shapes and fractional electron capture probabilities) associated with the radionuclides decaying via beta decay and electron capture. One of the tasks of LNHB-MA (French National Metrology Laboratory for Radionuclide Metrology) is to determine and evaluate nuclear and atomic decay data and to disseminate them in data tables. Accurate decay data is required in different fields of basic and applied sciences like nuclear medicine, particle physics, radiation metrology, and so on. Even to validate the theoretical models, accurate experimental data is needed. In the literature, the decay data associated with electron capture (EC) and beta decay often suffer from large or underestimated uncertainties. Moreover, in the case of EC, the measured radionuclides are very few, and the rest of the data is instead from theoretical calculations of - in many cases - questionable accuracy. Relying on fluorescence yields to determine fractional EC probabilities can be problematic since the fluorescence yields sometimes depend on the experimental values determined using theoretical or older measured electron capture probabilities.

In this thesis, to measure the fractional EC probabilities independently of fluorescence yields, the technique of Decay Energy Spectroscopy (DES) using Metallic Magnetic Calorimeters (MMCs) was used. MMCs have proven to have low energy thresholds down to a few tens eV, along with excellent energy resolution at low energies combined with exceptional detection efficiency and good linearity. Regardless of the particles released, MMCs can be used for all decays. MMCs measure the temperature change in the absorber caused by the energy deposited from a decay event. In the DES technique, the radionuclide is embedded between two absorber layers, forming a 4π geometry. Due to the long thermal time constants of the detector compared to the duration of the atomic rearrangement process, the energy of the individual Auger electrons and photons is summed up and read out as a single pulse. Thus, the total decay energy is measured except for the neutrino's energy and high-energy gamma rays that escape due to the low stopping power of the small absorber, in contrast to energy measurements of individual decay products. DES with cryogenic detectors offers an extremely high resolving power of up to several thousand, allowing high-precision spectrometry to measure and improve the decay data. In the case of beta decay, the shape of the beta spectrum is used in studying atomic effects like screening and exchange effects; EC measurements should also give access to atomic effects like shake-up and shake-off. Within the field of radionuclide metrology, these data are also required in primary activity standardization methods, in particular liquid scintillation counting, but also in secondary methods like ionization chambers. The beta spectrum measurement with MMCs in the DES technique has the potential to have a very low energy threshold and excellent energy linearity to study these nuclear and atomic effects.

Using the DES, the fractional capture probabilities for $^{125}\mathrm{I}$, $^{54}\mathrm{Mn}$ and $^{59}\mathrm{Ni}$ were measured, and the results obtained were compared with those in the literature and with the theoretical values from the BetaShape code developed at LNHB. Three different source preparation techniques, i.e., electroplating and drop deposition (manual and micro drop dispenser), were used to prepare the sources for the measurements. In the case of $^{59}\mathrm{Ni}$, a comparison could be made between the obtained spectra to

identify the best source preparation method for excellent energy resolution and minimum spectrum distortions. The results from the comparison showed the electroplated source to have better energy resolution and lower spectrum distortion as compared to the source prepared using a micro-drop dispenser.

The measured EC ratios for $^{125}\mathrm{I}$ were in agreement with the values in the literature but showed a large divergence from the recent values from the BetaShape calculation code. The main cause behind this large variance is the decrease in gold absorber thickness from 210 µm to 149 µm. Due to the decrease in the absorber thickness, the escape peaks for Te, Ag, and gamma were observed. The escape peaks were quantified, and while measuring the peak area to find fractional EC ratios, the peak areas for escape peaks were added to their main peaks. But, the $^{125}\mathrm{Te}$ escape peaks, (K_α and K_β from K+ γ) were not quantifiable, as they coincide with the M+γ and N+γ. Hence, this nuclide needs to be measured again with the correct absorber thickness, and the spectrum distortion can be improved by depositing the source in a nanofoam Ag foil instead of a plain Ag metal foil to limit the salt crystal formation.

For the case of $^{54}\mathrm{Mn}$ a good agreement between the MMC measurement and the theoretical value from BetaShape was observed for the ratio between the capture probabilities $P_\mathrm{L}/P_\mathrm{K}$ value and agreement to within 2σ for the ratio between the capture probabilities $P_\mathrm{M}/P_\mathrm{K}$. Similarly, for the case of $^{59}\mathrm{Ni}$, for the electrodeposited source, the $P_\mathrm{L}/P_\mathrm{K}$ value measured by MMC was in agreement with the value from BetaShape to within the standard uncertainty, and for the drop deposited source to within 2σ. The quantification of tailing on the left side of peaks for both electroplated and drop-deposited sources (the latter in Au nanofoam) is difficult with existing spectrum fitting tools, and once again demonstrated showed that the source material can lead to spectrum distortion due to incomplete thermalization. The reason in the case of drop-deposited sources is the formation of salt crystals during the drop drying, and that the electrons emitted in the decay process lose a part of their energy in the source material rather than the absorber material. This energy would not be entirely converted to detectable heat and leads to spectrum distortion and, consequently, degradation in the energy resolution.

The measured fractional EC ratio values for $^{54}\mathrm{Mn}$ and $^{59}\mathrm{Ni}$ can be used to update the available values in the decay data tables. The beta spectrum of $^{14}\mathrm{C}$ was also measured and revealed that the increase below 6 keV, noted in the previous 2019 measurement, resulted from non-optimal experimental conditions.

As we have seen, the source preparation is the most critical issue for nuclear decay data measurements using the DES technique. Another method by which spectrum distortion can be reduced, apart from electrodeposition or drop deposition into nanofoam instead of standard metal foil, is the use of ion-implantation for preparing the source. It was planned to use ion-implanted sources for high-precision measurements of the EC spectrum of ^{55}Fe during this thesis, in particular to study shake-up and shake-off effects, but also to determine fractional capture probabilities for the L sub-shells. Unfortunately, both due to delays in the fabrication of dedicated MMCs and unexpected difficulties in ^{55}Fe implantation, these measurements could not be performed before the end of the thesis.

As described in the thesis, MMCs have been successfully optimized and utilized for 4π decay spectrometry using a two-pixel MMC detector. Here, the 4π absorber-source ensemble was glued directly on the sensor of the MMC for the measurement. This makes the MMC non-reusable. Although in

some cases, after measurement, the 4π absorber-source ensemble was removed by dissolving the glue, there is always the probability of damaging the sensor. It was observed that while removing the absorber, in a few cases, the Ag:Er sensor layer came off. The solution to this problem is instead of directly gluing the absorber on the sensor, the thermal contact between the absorber and sensor using a gold bonding wire. This technique will be used for measurements with the new upgraded spectrometer setup (4.7). Until the completion of this thesis, an appropriate compromise between flexibility and detector performance has been achieved by designing different MMC sizes optimized for different energy ranges in the EMPIR MetroBeta and MetroMMC projects. In these projects and during this thesis, it was observed that because of the low counting statistics, the statistical uncertainty limits the comparison of the experimental spectra with theoretical calculations and the fundamental decay parameters. Till the completion of this thesis, the statistical uncertainty was limited ($< 10^6$ counts per day of data taking) by the count rate capability of a single MMC detector used for each measurement. To improve the statistical uncertainties, the spectrometer setup was upgraded to measure 10 detectors simultaneously with expected counting statistics of order 10^8 within few weeks of data taking. The upgraded spectrometer will also facilitate the use of the reusable MMC design, i.e. by placing the absorber-source ensemble on separate plates made of aluminum. The thermal link will be formed by using gold bonding wires between the absorber and the sensor of the MMC.

Bibliography

[1] G. F. Knoll, "Radiation Detection and Measurement, 3rd edition. New York: John Wiley and Sons, 2000. 21, 24, 27, 33, 34, 35

[2] https://www.academiesciences.fr/pdf/dossiers/Becquerel 22

[3] G. C. Schmidt, "Über die von den Thorverbindungen und einigen anderen Substanzen ausgehende Strahlung," Ann. Phys., vol. 301, no. 5, pp. 141–151, 1898, doi: 10.1002/andp.18983010512. 22

[4] M. Curie and G. Lippmann (M., Rayons émis par les composés de l'uranium et du thorium. Gauthier-Villars, 1898. 22

[5] E. Rutherford, "VIII. Uranium radiation and the electrical conduction produced by it," Lond. Edinb. Dublin Philos. Mag. J. Sci., vol. 47, no. 284, pp. 109–163, 1899. 22

[6] E. Rutherford, "XV. The magnetic and electric deviation of the easily absorbed rays from radium," Lond. Edinb. Dublin Philos. Mag. J. Sci., vol. 5, no. 26, pp. 177–187, Feb. 1903, doi: 10.1080/14786440309462912. 22

[7] B. D. Popp, "Discovery of the Electron: Radioactivity," in Henri Poincaré: Electrons to Special Relativity: Translation of Selected Papers and Discussion, B. D. Popp, Ed. Cham: Springer International Publishing, 2020, pp. 147–165. doi: 10.1007/978-3-030-48039-4_8. 22

[8] L. W. Alvarez, "Nuclear K Electron Capture," Phys. Rev., vol. 52, no. 2, pp. 134–135, Jul. 1937, doi: 10.1103/PhysRev.52.134. 22

[9] G. C. Wick, "Sulle Proprietà della Materia Nucleare," Il Nuovo Cimento 1924-1942, vol. 11, no. 4, pp. 227–234, Apr. 1934, doi: 10.1007/BF02959837. 22

[10] H. A. Bethe and R. F. Bacher, "Nuclear Physics A. Stationary States of Nuclei," Rev. Mod. Phys., vol. 8, no. 2, pp. 82–229, Apr. 1936, doi: 10.1103/RevModPhys.8.82. 22

[11] C. Møller, "On the Capture of Orbital Electrons by Nuclei," Phys. Rev., vol. 51, no. 2, pp. 84–85, Jan. 1937, doi: 10.1103/PhysRev.51.84. 22

[12] IAEA Nuclear Data Section, "Live Chart of Nuclides nuclear structure and decay data." 15, 22, 23

[13] K. S. Krane, "Introductory nuclear physics," CERN Document Server, 1988. 23, 26

[14] F. Wilson, "Fermi's Theory of Beta Decay," Am. J. Phys., vol. 36, p. 1150, Dec. 1968, doi: 10.1119/1.1974382. 23

[15] X. Mougeot, M.-M. Bé, V. Chisté, C. Dulieu, V. Gorozhankin, and M. Loidl, "Calculation of beta spectra for allowed and unique forbidden transitions," Radiocarbon, pp. 249–257, Jan. 2011. 25, 26

[16] X. Mougeot, M.-M. Bé, and C. Bisch, "Calculation of beta spectral shapes," Radioprotection, vol. 49, no. 4, pp. 269–273, Oct. 2014, doi: 10.1051/radiopro/2014017. 25, 26

[17] X. Mougeot, "Applied Radiation and Isotopes 154 (2019) 108884, doi: 10.1016/j.apradiso.2017.07.027 26, 109, 115, 120, 121

[18] E. Schönfeld, "Calculation of fractional electron capture probabilities," Appl. Radiat. Isot., vol. 49, no. 9, pp. 1353–1357, Aug. 1998, doi: 10.1016/S0969-8043(97)10073-2. 28

[19] W. Bambynek et al., "Orbital electron capture by the nucleus," Rev. Mod. Phys., vol. 49, no. 1, pp. 77–221, Jan. 1977, doi: 10.1103/RevModPhys.49.77. 28

[20] M. Aker et al., "Direct neutrino-mass measurement with sub-electronvolt sensitivity," Nat. Phys., vol. 18, no. 2, Art. no. 2, Feb. 2022, doi: 10.1038/s41567-021-01463-1. 28

[21] A. De Rújula and M. Lusignoli, "The calorimetric spectrum of the electron-capture decay of ^{163}Ho. The spectral endpoint region," J. High Energy Phys., vol. 2016, no. 5, p. 15, May 2016, doi: 10.1007/JHEP05(2016)015. 28

[22] S. Yasumi et al., "The mass of the electron neutrino from electron capture in ^{163}Ho," Phys. Lett. B, vol. 334, no. 1, pp. 229–233, Aug. 1994, doi: 10.1016/0370-2693(94)90616-5. 28

[23] L. Gastaldo et al., "The electron capture in ^{163}Ho experiment – ECHo," Eur. Phys. J. Spec. Top., vol. 226, no. 8, pp. 1623–1694, Jun. 2017, doi: 10.1140/epjst/e2017-70071-y. 28

[24] B. Alpert et al., "HOLMES," Eur. Phys. J. C, vol. 75, no. 3, p. 112, Mar. 2015, doi: 10.1140/epjc/s10052-015-3329-5. 28

[25] R. G. H. Robertson, "Direct Measurement of Neutrino Mass," J. Phys. Conf. Ser., vol. 173, p. 012016, Jun. 2009, doi: 10.1088/1742-6596/173/1/012016. 28

[26] V. M. Lobashev, "The search for the neutrino mass by direct method in the tritium beta-decay and perspectives of study it in the project KATRIN," Nucl. Phys. A, vol. 719, pp. C153–C160, May 2003, doi: 10.1016/S0375-9474(03)00985-0. 28

[27] S. Mertens et al., "Sensitivity of Next-Generation Tritium Beta-Decay Experiments for keV-Scale Sterile Neutrinos," J. Cosmol. Astropart. Phys., vol. 2015, no. 02, pp. 020–020, Feb. 2015, doi: 10.1088/1475-7516/2015/02/020. 28

[28] F. M. Fraenkle and for the KATRIN collaboration, "The neutrino mass experiment KATRIN," J. Phys. Conf. Ser., vol. 1342, no. 1, p. 012024, Jan. 2020, doi: 10.1088/1742-6596/1342/1/012024. 28

[29] A. L. Nichols, "Decay data:: review of measurements, evaluations and compilations," Appl. Radiat. Isot., vol. 55, no. 1, pp. 23–70, Jul. 2001, doi: 10.1016/S0969-8043(00)00382-1. 31, 32

[30] A. L. Nichols, "Recommended decay data and evaluated databases – international perspectives," J. Nucl. Sci. Technol., vol. 52, no. 1, pp. 17–40, Jan. 2015, doi: 10.1080/00223131.2014.929985. 31, 32

[31] A. L. Nichols, "Nuclear decay data: Observations and reflections," Appl. Radiat. Isot., vol. 64, no. 10, pp. 1384–1391, Oct. 2006, doi: 10.1016/j.apradiso.2006.02.071. 31, 32

[32] D. P. Humbert, A. L. Nichols, and O. Schwerer, "IAEA Nuclear Data Section: provision of atomic and nuclear databases for user applications," Appl. Radiat. Isot. Data Instrum. Methods Use Agric. Ind. Med., vol. 60, no. 2–4, pp. 311–316, 2004, doi: 10.1016/j.apradiso.2003.11.034. 31, 32

[33] M. A. Kellett and O. Bersillon, "The Decay Data Evaluation Project (DDEP) and the JEFF-3.3 radioactive decay data library: Combining international collaborative efforts on evaluated decay data," EPJ Web Conf., vol. 146, p. 02009, 2017, doi: 10.1051/epjconf/201714602009. 31

[34] C. Dulieu, M. M. Bé, and V. Chisté, "Tools and publications for reference decay data," in ND2007, Nice, France, 2007, p. 027. doi: 10.1051/ndata:07503. 31

[35] http://www.lnhb.fr/Laraweb/. 16, 17, 18, 31, 77, 80, 83, 84, 87, 88, 105, 111, 116, 121, 123

[36] M. Loidl et al., "Nuclear and atomic data determination with metallic magnetic calorimeters," Nucl. Instrum. Meth. A, vol. 559, no. 2, pp. 769–771, Apr. 2006, doi: 10.1016/j.nima.2005.12.138. 32

[37] M. Loidl et al., "MetroBeta: Beta Spectrometry with Metallic Magnetic Calorimeters in the Framework of the European Program of Ionizing Radiation Metrology," J. Low Temp. Phys., vol. 193, no. 5, pp. 1251–1256, Dec. 2018, doi: 10.1007/s10909-018-1933-0. 19, 32, 49, 52, 72, 73, 83, 120

[38] R. M. Dolby, "Absolute intensity measurements of the carbon and aluminium X-ray K-lines with a proportional counter," Br. J. Appl. Phys., vol. 11, no. 2, p. 64, Feb. 1960, doi: 10.1088/0508-3443/11/2/304. 33

[39] R. Batchelor, R. Aves, and T. H. R. Skyrme, "Helium-3 Filled Proportional Counter for Neutron Spectroscopy," Rev. Sci. Instrum., vol. 26, no. 11, pp. 1037–1047, Dec. 2004, doi: 10.1063/1.1715182. 33

[40] H. Sipilä, "Energy resolution of the proportional counter," Nucl. Instrum. Methods, vol. 133, no. 2, pp. 251–252, Mar. 1976, doi: 10.1016/0029-554X(76)90616-9. 33, 38

[41] N. P. Zaitseva et al., "Recent developments in plastic scintillators with pulse shape discrimination," Nucl. Instrum. Meth. A, vol. 889, pp. 97–104, May 2018, doi: 10.1016/j.nima.2018.01.093. 35, 38

[42] J. B. Birks, "CHAPTER 8 - ORGANIC LIQUID SCINTILLATORS," in The Theory and Practice of Scintillation Counting, J. B. Birks, Ed., in International Series of Monographs in Electronics and Instrumentation. Pergamon, 1964, pp. 269–320. doi:10.1016/B978-0-08-010472-0.50013-6. 35, 38

[43] M. Rizzi, D. Matteo, and B. Castagnolo, "Semiconductor Detectors and Principles of Radiation-matter Interaction," J. Appl. Sci., vol. 10, pp. 3141–3155, Dec. 2010, doi: 10.3923/jas.2010.3141.3155. 35, 38

[44] M.-C. Lépy, L. Brondeau, Y. Ménesguen, S. Pierre, and J. Riffaud, "Consistency of photon emission intensities for efficiency calibration of gamma-ray spectrometers in the energy range from 20keV to 80keV," Appl. Radiat. Isot., vol. 134, pp. 131–136, Apr. 2018, doi: 10.1016/j.apradiso.2017.07.006. 36, 38

[45] M. Moll, "Radiation tolerant semiconductor sensors for tracking detectors," Nucl. Instrum. Meth. A, vol. 565, no. 1, pp. 202–211, Sep. 2006, doi: 10.1016/j.nima.2006.05.001. 36

[46] G. L. Miller, W. M. Gidson, and P. F. Donovan, "Semiconductor Particle Detectors," Annu. Rev. Nucl. Sci., vol. 12, no. 1, pp. 189–220, 1962, doi: 10.1146/annurev.ns.12.120162.001201. 36

[47] D. Twerenbold, "Cryogenic particle detectors," Rep. Prog. Phys., vol. 59, no. 3, p. 349, Mar. 1996, doi: 10.1088/0034-4885/59/3/002. 38, 39

[48] E. Previtali, "20 years of cryogenic particle detectors: past, present and future," Nucl. Phys. B Proc. Suppl., vol. 150, pp. 3–8, Jan. 2006, doi: 10.1016/j.nuclphysbps.2005.04.060. 38, 39

[49] F. Simon, "Application of Low Temperature Calorimetry to Radioactive Measurements," Nature, vol. 135, no. 3418, Art. no. 3418, May 1935, doi: 10.1038/135763a0. 38

[50] S. H. Moseley, J. C. Mather, and D. McCammon, "Thermal detectors as x-ray spectrometers," J. Appl. Phys., vol. 56, no. 5, pp. 1257–1262, Sep. 1984, doi: 10.1063/1.334129. 39

[51] J. E. Evetts et al., "Superconducting indium detectors for solar neutrinos," Nucl. Instrum. Meth. A, vol. 264, no. 1, pp. 41–47, Feb. 1988, doi: 10.1016/0168-9002(88)91100-X. 39

[52] CDMS Collaboration et al., "New results from the Cryogenic Dark Matter Search experiment," Phys. Rev. D, vol. 68, no. 8, p. 082002, Oct. 2003, doi: 10.1103/PhysRevD.68.082002. 39, 44

[53] SuperCDMS Collaboration et al., "Results from the Super Cryogenic Dark Matter Search Experiment at Soudan," Phys. Rev. Lett., vol. 120, no. 6, p. 061802, Feb. 2018, doi: 10.1103/Ph52,53ysRevLett.120.061802. 39, 44

[54] M. Bravin et al., "The CRESST dark matter search," Astropart. Phys., vol. 12, no. 1, pp. 107–114, Oct. 1999, doi: 10.1016/S0927-6505(99)00073-0. 39, 44

[55] M. Loidl et al., "High-energy resolution X-ray, gamma and electron spectroscopy with cryogenic detectors," Appl. Radiat. Isot., vol. 60, no. 2, pp. 363–368, Feb. 2004, doi: 10.1016/j.apradiso.2003.11.043. 39

[56] E. Leblanc et al., "A new absolute method for the standardization of radionuclides emitting low-energy radiation," Appl. Radiat. Isot., vol. 56, no. 1, pp. 245–251, Jan. 2002, doi: 10.1016/S0969-8043(01)00195-6. 39

[57] D. Horansky et al., "Analysis of Nuclear Material by Alpha Spectroscopy with a Transition-Edge Microcalorimeter," J. Low Temp. Phys., vol. 151, no. 3, pp. 1067–1073, May 2008, doi: 10.1007/s10909-008-9789-3. 40

[58] T. Jach, J. N. Ullom, and W. T. Elam, “The microcalorimeter X-ray detector: A true paradigm shift in X-ray spectroscopy,” Eur. Phys. J. Spec. Top., vol. 169, no. 1, pp. 237–242, Mar. 2009, doi: 10.1140/epjst/e2009-00998-3. 40

[59] S.-J. Lee et al., “Cryogenic measurement of alpha decay in a 4π absorber,” J. Phys. G Nucl. Part. Phys., vol. 37, no. 5, p. 055103, Mar. 2010, doi: 10.1088/0954-3899/37/5/055103. 40

[60] S. J. Lee et al., “The development of a cryogenic detector with $CaMoO_4$ crystals for neutrinoless double beta decay search,” Astropart. Phys., vol. 34, no. 9, pp. 732–737, Apr. 2011, doi:10.1016/j.astropartphys.2011.01.004. 40

[61] C. Enss and D. McCammon, “Physical Principles of Low Temperature Detectors: Ultimate Performance Limits and Current Detector Capabilities,” J. Low Temp. Phys., vol. 151, no. 1, pp. 5–24, Apr. 2008, doi: 10.1007/s10909-007-9611-7. 16, 40, 46, 65, 67

[62] D. Mccammon, “Semiconductor Thermistors,” in C. Enss (ed.), "Cryogenic Particle Detection", Topics Appl. Phys. 99, Springer-Verlag, Berlin Heidelberg, 2005, pp. 3–23. https://doi.org/10.1007/109335962. 42

[63] A. Nucciotti et al., “Comparison between implanted Si and NTD-Ge thermistors performance in $AgReO_4$ microcalorimeters for a new neutrino mass experiment,” Nucl. Instrum. Meth. A, vol. 559, no. 2, pp. 367–369, Apr. 2006, doi: 10.1016/j.nima.2005.12.011. 42

[64] E. E. Haller, K. M. Itoh, and J. W. Beeman, “Neutron Transmutation Depot (NTD) Germanium Thermistors for Submillimetre Bolometer Applications,” vol. 388, p. 115, Dec. 1996. 42

[65] K. D. Irwin and G. C. Hilton, “Transition-Edge Sensors,” in C. Enss (ed.), "Cryogenic Particle Detection", Topics Appl. Phys. 99, Springer-Verlag, Berlin Heidelberg, 2005, pp. 63–150. doi: 10.1007/109335963. 42, 43

[66] D. H. Andrews, W. F. Brucksch, W. T. Ziegler, and E. R. Blanchard, “Superconducting Films as Radiometric Receivers,” Phys. Rev., vol. 59, no. 12, pp. 1045–1046, Jun. 1941, doi: 10.1103/PhysRev.59.1045.2. 42

[67] D. H. Andrews, R. D. Fowler, and M. C. Williams, “The Effect of Alpha-particles on a Superconductor,” Phys. Rev., vol. 76, no. 1, pp. 154–155, Jul. 1949, doi: 10.1103/PhysRev.76.154.2. 43

[68] W. Seidel et al., “Phase transition thermometers with high temperature resolution for calorimetric particle detectors employing dielectric absorbers,” Phys. Lett. B, vol. 236, no. 4, pp. 483–487, Mar. 1990, doi: 10.1016/0370-2693(90)90388-M. 15, 43, 44

[69] J. N. Ullom and D. A. Bennett, “Review of superconducting transition-edge sensors for x-ray and gamma-ray spectroscopy,” Supercond. Sci. Technol., vol. 28, no. 8, p. 084003, Jul. 2015, doi: 10.1088/0953-2048/28/8/084003. 44

[70] M. P. Croce et al., “Superconducting Transition-Edge Sensor Microcalorimeters for Ultra-High Resolution Alpha-Particle Spectrometry,” IEEE Trans. Appl. Supercond., vol. 21, no. 3, pp. 207–210, Jun. 2011, doi: 10.1109/TASC.2010.2096790 44

[71] P. D. Mauskopf, “Transition Edge Sensors and Kinetic Inductance Detectors in Astronomical Instruments,” Publ. Astron. Soc. Pac., vol. 130, no. 990, p. 082001, Jun. 2018, doi: 10.1088/1538-3873/aabafo. 44

[72] C. L. Chang et al., “Detectors for the South Pole Telescope,” Phys. Procedia, vol. 37, pp. 1381–1388, Jan. 2012, doi: 10.1016/j.phpro.2012.02.476. 44

[73] C. Enss et al., “Metallic Magnetic Calorimeters for Particle Detection,” J. Low Temp. Phys., vol. 121, pp. 137–176, Nov. 2000, doi:10.1023/A:1004863823166. 15, 45, 46, 50, 52, 55, 58, 65, 66

[74] A. Fleischmann et al., “Metallic magnetic calorimeters,” AIP Conf. Proc., vol. 1185, no. 1, pp. 571–578, Dec. 2009, doi: 10.1063/1.3292407. 15, 46, 50, 52, 55

[75] R. L. Kelley et al., “Development of microcalorimeters for high resolution X-ray spectroscopy,” J. Low Temp. Phys., vol. 93, no. 3, pp. 225–230, Nov. 1993, doi: 10.1007/BF00693424. 39

[76] J. Baselmans, “Kinetic Inductance Detectors,” J. Low Temp. Phys., vol. 167, no. 3, pp. 292–304, May 2012, doi: 10.1007/s10909-011-0448-8. 46

[77] T. Cecil et al., “Kinetic Inductance Detectors for X-Ray Spectroscopy,” Phys. Procedia, vol. 37, pp. 697–702, Jan. 2012, doi: 10.1016/j.phpro.2012.03.719. 47

[78] G. Ulbricht, M. De Lucia, and E. Baldwin, “Applications for Microwave Kinetic Induction Detectors in Advanced Instrumentation,” Appl. Sci., vol. 11, no. 6, Art. no. 6, Jan. 2021, doi: 10.3390/app11062671. 47

[79] P. Lerch and A. Zehnder, “Quantum Giaever Detectors: STJ’s,” in C. Enss (ed.), "Cryogenic Particle Detection", Topics Appl. Phys. 99, Springer-Verlag, Berlin Heidelberg, 2005, pp. 217–266. doi: 10.1007/109335965. 15, 47

[80] D. D. E. Martin and P. Verhoeve, “Superconducting tunnel junctions,” in Observing Photons in Space: A Guide to Experimental Space Astronomy, M. C. E. Huber, A. Pauluhn, J. L. Culhane, J. G. Timothy, K. Wilhelm, and A. Zehnder, Eds., in ISSI Scientific Report Series. New York, NY: Springer, 2013, pp. 479–496. doi: 10.1007/978-1-4614-7804-127. 47, 48

[81] G. Angloher, “Low-temperature detectors,” Nucl. Instrum. Meth. A, vol. 512, no. 1, pp. 401–407, Oct. 2003, doi: 10.1016/S0168-9002(03)01918-1. 15, 47, 48

[82] P. C.-O. Ranitzsch et al., “MetroMMC: Electron-Capture Spectrometry with Cryogenic Calorimeters for Science and Technology,” J. Low Temp. Phys., vol. 199, no. 1, pp. 441–450, Apr. 2020, doi: 10.1007/s10909-019-02278-4. 49, 52

[83] M. Loidl, M. Rodrigues, and R. Mariam, “Measurement of the electron capture probabilities of ^{55}Fe with a metallic magnetic calorimeter,” Appl. Radiat. Isot., vol. 134, pp. 395–398, Apr. 2018, doi: 10.1016/j.apradiso.2017.10.042. 49

[84] M. Loidl et al., “Feasibility study of absolute activity measurement with metallic magnetic microcalorimeters,” Nucl. Instrum. Meth. A, vol. 520, no. 1, pp. 73–75, Mar. 2004, doi: 10.1016/j.nima.2003.11.224. 49, 52

[85] K. Kossert, M. Loidl, X. Mougeot, M. Paulsen, P. Ranitzsch, and M. Rodrigues, “High precision measurement of the ^{151}Sm beta decay by means of a metallic magnetic calorimeter,” Appl. Radiat. Isot., vol. 185, p. 110237, Jul. 2022, doi: 10.1016/j.apradiso.2022.110237. 49

[86] R. Mariam, M. Rodrigues, M. Loidl, S. Pierre, and V. Lourenço, “Determination of L-X ray absolute emission intensities of ^{238}Pu, ^{244}Cm, ^{237}Np and ^{233}Pa radionuclides using a metallic magnetic calorimeter,” Spectrochim. Acta Part B At. Spectrosc., vol. 187, p. 106331, Jan. 2022, doi: 10.1016/j.sab.2021.106331. 49

[87] M. Rodrigues, R. Mariam, and M. Loidl, “A metallic magnetic calorimeter dedicated to the spectrometry of L X-rays emitted by actinides,” EPJ Web Conf., vol. 146, p. 10012, 2017, doi: 10.1051/epjconf/201714610012. 49

[88] W. Seidel: Diploma thesis, Technical University of Munich (1986), unpublished. 51

[89] T. Fausch, M. Bühler, and E. Umlauf, “Signal rise time of the magnetic bolometer,” J. Low Temp. Phys., vol. 93, no. 3, pp. 703–708, Nov. 1993, doi: 10.1007/BF00693499. 51

[90] A. Fleischmann, C. Enss, and G. M. Seidel, “Metallic Magnetic Calorimeters,” in C. Enss (ed.), "Cryogenic Particle Detection", Topics Appl. Phys. 99, Springer-Verlag, Berlin Heidelberg, 2005, pp. 151–216. doi: 10.1007/10933596_4. 51, 58, 61, 65, 68, 69, 70

[91] S. R. Bandler et al., “Metallic magnetic bolometers for particle detection,” J. Low Temp. Phys., vol. 93, no. 3–4, pp. 709–714, Nov. 1993, doi: 10.1007/BF00693500. 51

[92] L. J. Tao, D. Davidov, R. Orbach, and E. P. Chock, “Hyperfine Splitting of Er and Yb Resonances in Au: A Separation between the Atomic and Covalent Contributions to the Exchange Integral,” Phys. Rev. B, vol. 4, no. 1, pp. 5–9, Jul. 1971, doi: 10.1103/PhysRevB.4.5. 55

[93] S. Kempf, A. Fleischmann, L. Gastaldo, and C. Enss, “Physics and Applications of Metallic Magnetic Calorimeters,” J. Low Temp. Phys., vol. 193, no. 3, pp. 365–379, Nov. 2018, doi: 10.1007/s10909-018-1891-6. 15, 16, 52, 56, 62, 70, 71

[94] L. Fleischmann et al., “Physics and applications of metallic magnetic calorimeters for particle detection,” J. Phys. Conf. Ser., vol. 150, no. 1, p. 012013, Feb. 2009, doi: 10.1088/1742-6596/150/1/012013. 50

[95] K. E. Koehler, “Low Temperature Microcalorimeters for Decay Energy Spectroscopy,” Appl. Sci., vol. 11, no. 9, Art. no. 9, Jan. 2021, doi: 10.3390/app11094044. 52

[96] M. Loidl, M. Rodrigues, C. Le-Bret, and X. Mougeot, “Beta spectrometry with metallic magnetic calorimeters,” Appl. Radiat. Isot., vol. 87, pp. 302–305, May 2014, doi: 10.1016/j.apradiso.2013.11.024. 52

[97] L. Bockhorn et al., “Improved Source/Absorber Preparation for Radionuclide Spectrometry Based on Low-Temperature Calorimetric Detectors,” J. Low Temp. Phys., vol. 199, no. 1, pp. 298–305, Apr. 2020, doi: 10.1007/s10909-019-02274-8. 52, 53, 79, 90

[98] R. L. Mößbauer, “Progress in cryogenic detectors for neutrinos, dark matter and rare processes,” Nucl. Phys. B - Proc. Suppl., vol. 31, pp. 385–396, Apr. 1993, doi: 10.1016/0920-5632(93)90161-X. 53

[99] J.-P. Porst et al., “Properties of Superconducting Rhenium as an Absorber for Magnetic Calorimeters,” J. Low Temp. Phys., vol. 151, no. 1, pp. 436–442, Apr. 2008, doi: 10.1007/s10909-007-9665-6. 53

[100] Y. H. Kim et al., “Measurements and modeling of the thermal properties of a calorimeter having a sapphire absorber,” Nucl. Instrum. Meth. A, vol. 520, no. 1, pp. 208–211, Mar. 2004, doi: 10.1016/j.nima.2003.11.230. 54

[101] A. Fleischmann et al., “Low Temperature Properties of Erbium In Gold,” J. Low Temp. Phys., vol. 118, no. 1, pp. 7–21, Jan. 2000, doi: 10.1023/A:1004654401827. 54, 65

[102] T. Herrmannsdörfer, R. König, and C. Enss, “Properties of Er-doped Au at ultralow temperatures,” Phys. B Condens. Matter, vol. 284–288, pp. 1698–1699, Jul. 2000, doi: 10.1016/S0921-4526(99)02942-7. 54

[103] M. Herbst et al., “Numerical Calculation of the Thermodynamic Properties of Silver Erbium Alloys for Use in Metallic Magnetic Calorimeters,” J. Low Temp. Phys., vol. 209, no. 5, pp. 1119–1127, Dec. 2022, doi: 10.1007/s10909-022-02739-3. 54

[104] Talgat Daniyarov, Metallische magnetische Kalorimeter zum hochauflösenden Nachweis von Röntgenquanten und hochenergetischen Molekülen, Dissertation, Kirchhoff-Institute for Physics, University of Heidelberg, 2005. 16, 68, 69

[105] Andreas Burck, Entwicklung großflächiger mikrostrukturierter magnetischer Kalorimeter mit Au:Er- und Ag:Er-Sensoren fur den energieaufgelösten Nachweis von Röntgenquanten und hochenergetischen Teilchen, Dissertation, Kirchhoff-Institute for Physics, University of Heidelberg, 2008 68

[106] D. McCammon, “Thermal Equilibrium Calorimeters – An Introduction,” in C. Enss (ed.), "Cryogenic Particle Detection", Topics Appl. Phys. 99, Springer-Verlag, Berlin Heidelberg, 2005, pp. 1–34. doi: 10.1007/10933596_1. 67, 69

[107] M. Paulsen et al., “Development of a beta spectrometry setup using metallic magnetic calorimeters,” J. Instrum., vol. 14, p. P08012, Aug. 2019, doi: 10.1088/1748-0221/14/08/P0801 16, 64, 72

[108] S. Kempf, A. Ferring, A. Fleischmann, and C. Enss, “Direct-current superconducting quantum interference devices for the readout of metallic magnetic calorimeters,” Supercond. Sci. Technol., vol. 28, no. 4, p. 045008, Feb. 2015, doi: 10.1088/0953-2048/28/4/045008. 16, 64

[109] P. C.-O. Ranitzsch, "Low Temperature Calorimeters with Superconducting Particle Absorbers". 16, 65

[110] S. M. Anton et al., "Magnetic Flux Noise in dc SQUIDs: Temperature and Geometry Dependence," Phys. Rev. Lett., vol. 110, no. 14, p. 147002, Apr. 2013, doi: 10.1103/PhysRevLett.110.147002. 69

[111] J. Clarke und A.I. Braginski (Ed.), The SQUID Handbook: Vol. I Fundamentals and Technology of SQUIDs and SQUID Systems, Wiley-VCH, Weinheim, 2004, ISBN 3-527-40229-2 69

[112] F. Salvat, J. M. Fernandez-Varea, E. Acosta, and J. Sempau, Penelope - A code system for Monte Carlo simulation of electron and photon transport. Nuclear Energy Agency of the OECD (NEA): Organisation for Economic Co-Operation and Development - Nuclear Energy Agency, 2001. https://doi.org/10.1787/32da5043-en. 72, 76

[113] M. Rodrigues, M. Laarraj, M. Loidl, X.-F. Navick, and L. Ferlazzo, "Preparation of Drop-Deposited Sources in 4π Absorbers for Total Decay Energy Spectrometry," J. Low Temp. Phys., vol. 199, no. 1, pp. 461–466, Apr. 2020, doi: 10.1007/s10909-020-02410-9. 79, 84

[114] Y. Sun, K. P. Kucera, S. A. Burger, and T. John Balk, "Microstructure, stability and thermomechanical behavior of crack-free thin films of nanoporous gold," Scr. Mater., vol. 58, no. 11, pp. 1018–1021, Jun. 2008, doi: 10.1016/j.scriptamat.2008.01.036. 84

[115] G. Sibbens and T. Altzitzoglou, "Preparation of radioactive sources for radionuclide metrology," Metrologia, vol. 44, no. 4, p. S71, Aug. 2007, doi: 10.1088/0026-1394/44/4/S09. 75, 79

[116] C. Le-Bret, M. Loidl, M. Rodrigues, X. Mougeot and J. Bouchard: Study of the influence of the source quality on the determination of the shape factor of beta spectra, J. Low Temp. Phys. 167 (2012) 985 79, 82

[117] A. Kaur, M. Loidl, and M. Rodrigues, "Determination of Fractional Electron Capture Probabilities of ^{125}I Using Metallic Magnetic Calorimeters," J. Low Temp. Phys., vol. 209, no. 5, pp. 864–871, Dec. 2022, doi: 10.1007/s10909-022-02851-4. 86

[118] Y. B. Song and D.-T. Chin, "Current efficiency and polarization behavior of trivalent chromium electrodeposition process," Electrochimica Acta, vol. 48, no. 4, pp. 349–356, Dec. 2002, doi: 10.1016/S0013-4686(02)00678-3. 86

[119] G. Saravanan and S. Mohan, "Structure, current efficiency, and corrosion properties of brush electrodeposited (BED) Cr from Cr(III)dimethyl formamide (DMF)-bath," J. Appl. Electrochem., vol. 40, no. 1, pp. 1–6, Jan. 2010, doi: 10.1007/s10800-009-9962-7. 88

[120] P. Sahoo, S. V. Narasimhan, and S. E. Kannan, "Preparation of an Electrodeposited Source of ^{54}Mn," Radiochim. Acta, vol. 76, p. 185, Mar. 1997, doi: 10.1524/ract.1997.76.4.185.

[121] A. K. Gupta, H. K. Srivastava, J. Singh, P. Srivastava, and R. Kashyap, "Electrodeposition of nickel from dimethyl sulphoxide bath: Effect of nucleoside," IJCT Vol151 January 2008, Available: http://nopr.niscpr.res.in/handle/123456789/875 89

[122] H. K. Srivastava and P. K. Tikoo, "Electrodeposition of Nickel from N,N-dimethylformamide," Surf. Coat. Technol., vol. 31, no. 4, pp. 343–350, Oct. 1987, doi: 10.1016/0257-8972(87)90161-7. 89

[123] S. Biallozor, A. Lisowska-Oleksiak, and M. Lieder, "Investigations on electrodeposition of nickel from dimethylsulfoxide," Electrochimica Acta, vol. 29, no. 2, pp. 233–238, Feb. 1984, doi: 10.1016/0013-4686(84)87052-8. 89

[124] T. Kieck, H. Dorrer, C. E. Düllmann, V. Gadelshin, F. Schneider, and K. Wendt, "Highly efficient isotope separation and ion implantation of ^{163}Ho for the ECHo project," Nucl. Instrum. Meth. A, vol. 945, p. 162602, Nov. 2019, doi: 10.1016/j.nima.2019.162602. 90

[125] G. Gallucci et al., "163Ho Distillation and Implantation for HOLMES Experiment," J. Low Temp. Phys., vol. 194, no. 5, pp. 453–459, Mar. 2019, doi: 10.1007/s10909-018-2086-x. 90

[126] R. Haudebourg and P. Fichet, "A non-destructive and on-site digital autoradiography-based tool to identify contaminating radionuclide in nuclear wastes and facilities to be dismantled," J. Radioanal. Nucl. Chem., vol. 309, pp. 1–11, Nov. 2015, doi: 10.1007/s10967-015-4610-7. 78

[127] M. Zhang et al., "Image deconvolution in digital autoradiography: a preliminary study," Med. Phys., vol. 35, no. 2, pp. 522–530, Feb. 2008, doi: 10.1118/1.2828198. 78

[128] F. Pobell, Matter and Methods at Low Temperatures. Springer Science & Business Media, 2007. 93

[129] H. E. Hall, P. J. Ford, and K. Thompson, "A helium-3 dilution refrigerator," Cryogenics, vol. 6, no. 2, pp. 80–88, Apr. 1966, doi: 10.1016/0011-2275(66)90034-8. 93

[130] J. C. Wheatley, O. E. Vilches, and W. R. Abel, "Principles and methods of dilution refrigeration," Phys. Phys. Fiz., vol. 4, no. 1, pp. 1–64, Aug. 1968, doi: 10.1103/PhysicsPhysiqueFizika.4.1 93

[131] M. Rodrigues, "Développement d'un bolomètre magnétique haute résolution en énergie pour la spectrométrie gamma appliquée à la détermination des intensités d'émission photonique," These de doctorat (PhD thesis), Paris 11, 2007. Available: https://www.theses.fr/2007PA112277 95

[132] Lee, J.H., Jang, Y.S., Yoon, W.S. et al. Monte Carlo Simulation and Experimental Study of Alpha Decays in 4π Absorbers. J Low Temp Phys 176, 1053-1061 (2014). https://doi.org/10.1007/s10909-014-1107-7 79

[133] F.Buchegger, et al. Eur J Nucl Med Mol Imaging 33, 1352–1363 (2006). DOI:10.1007/s00259-006-0187-2 104

[134] K. A. Robertson, Comput. Math. Methods Med. 651475, 14 (2012).DOI: 10.1155/2012/651475 104

[135] M. Alotiby, et al., Phys. Med. Biol. 63(6),06NT04 (2018), DOI:10.1088/1361-6560/aab24b 104

[136] M. Alotiby, et al., J. Electron Spectrosc. Relat. Phenom. 232, 73-82 (2019), DOI:10.1016/j.elspec.2019.02.009 104

[137] A. Ku, et al. Auger electrons for cancer therapy – a review. EJNMMI radiopharm. chem. 4, 27 (2019). DOI:10.1186/s41181-019-0075-2 104

[138] H. Leutz, K. Ziegler, Nucl. Phys. 50, 648–656 (1964) 109

[139] K.M. Smith, G.M. Lewis, Nucl. Phys. 89, 561–564 (1966) 109

[140] V.D.M.L. Kalyani et al., Il Nuovo Cimento A 109(8), 1129–1133 (1996). https:// doi. org/ 10. 1007/ BF027 98818 109

[141] Karttunen et al., Nucl. Phys. A 131(1969), 343–352 (1969). https:// doi. org/ 10. 1016/ 0375- 9474(69) 90539-9 109

[142] J. Plch, J. Zderadička, Intensities of γ- and X-rays in the ^{125}I decay. Czech J. Phys. 24, 1311–1313 (1974). https:// doi. org/ 10. 1007/ BF015 89807 109

[143] F. Tolea, K.R. Baker, W.D. Schmidt-Ott et al., The electron capture decay of ^{125}I and ^{145}Pm. Z. Physik 268, 289–292 (1974). https:// doi. org/ 10. 1007/ BF016 69463 109

[144] E. Der Mateosian, Phys. Rev. 92, 4 (1953) 109

[145] R. B. Moler and R. W. Fink, "$\frac{L}{K}$-Capture Ratio in Mn^{54}, Fe^{55}, Co^{57}, and Co^{58} Decays," Phys. Rev., vol. 131, no. 2, pp. 821–829, Jul. 1963, doi: 10.1103/PhysRev.131.821. 115, 116

[146] G. Manduchi and G. Zannoni, "Experimental results on orbital-electron capture," Il Nuovo Cimento, vol. 27, no. 1, pp. 251–256, 1963, doi: 10.1007/BF02812618. 115, 116

[147] P. Kramer, M. E. C. Bos, A. De Beer, and J. Blok, "Measurements on electron capture branching ratios in the decay of the nuclides ^{54}Mn, ^{65}Zn and ^{57}Co," Physica, vol. 28, pp. 569–581, Jun. 1962, doi: 10.1016/0031-8914(62)90111-8 115, 116

[148] W. M. Chew, A. C. Xenoulis, R. W. Fink, and J. J. Pinajian, "Nuclear matrix elements from L/K electron capture ratios in ^{59}Ni decay," Nucl. Phys. A, vol. 218, no. 2, pp. 372–380, Jan. 1974, doi: 10.1016/0375-9474(74)90010-4. 116, 120

[149] M. Loidl et al.: Precision Measurements of Beta Spectra using Metallic Magnetic Calorimeters within the European Metrology Research Project MetroBeta, J. Low Temp. Phys. 199 (2020) 451-460, doi: 10.1007/s10909-020-02398-2 53, 120

[150] M. Haverkort, private communication (2020) 17, 113